Master Thesis in Medical Physics
Department of Physics and Technology
University of Bergen

Modelling Demyelination and Neuronal Loss from Diffusion Weighted Magnetic Resonance Images in an Experimental Model of Multiple Sclerosis

Vanja Flatberg

Supervisor: Assoc. Prof. Eli Renate Grüner
Co-supervisor: Dr. Tina Pavlin

Bergen, June 2015

Abstract

This master project is an application of an advanced biophysical model of water diffusion in tissue to asses neuronal microstructure of mouse and rat brain and, in particular, to find potential imaging markers of demyelination and neuronal integrity. The model is applied to animals at different stages of cuprizone exposure, which models the demyelination of neurons caused by multiple sclerosis (MS). This is the first time the model has been applied to study MS.

While the changes in white matter microstructure in MS have been extensively studied, lesions causing demyelination of gray matter are also present in the disease. In mouse brains, cuprizone exposure has been shown to induce demyelination and oligodendrocyte degeneration similar to that occurring in these lesions. Through conventional diffusion weighted imaging (DWI) sequences one is able to probe the microstructure of the brain tissues and detect changes such as MS lesions, but they are not pathologically specific. The complex biophysical model applied in the thesis is based on a DWI sequence to very high b -values, which allows probing on a micrometer scale. The diffusion weighted signal is modelled as a sum of the contribution from dendrites and axons (collectively named neurites) with cylindrical symmetry, and the extracellular space with spherical diffusion symmetry.

In mouse and rat brains, the neurite density, and the longitudinal and extracellular diffusion coefficients estimated from the model were used to quantify the extent of demyelination in corpus callosum, deep gray matter and the cortex. In all regions of the mouse brains, the neurite density was found to decrease significantly with cuprizone expsure. The longitudinal diffusion coefficient, and thus the diffusivity in neurites, showed a corresponding increase. In addition there was a significant increase in the extracellular diffusion coefficient in the corpus callosum of cuprizone exposed brains. In all regions a significant increase in neurite density 4 weeks after ended exposure to cuprizone was shown. In all regions the neurite densities were shown to correlate well with the myelin levels estimated from histology. However, they were not found to correlate with the axon development of gray matter.

In all regions, the neurite density and the longitudinal diffusion coefficient correlated with the estimated ADC from conventional diffusion modelling of the same brains. In both the cortex and deep gray matter, the complex model was able to detect significant changes in the neurite density, which was supported by the estimated myelin content from histology. While the same trend was seen in the ADC, the changes were not at a significant level.

In the rat brains, no significant changes in any of the imaging parameters were detected in any of the defined regions of interest. Both histology and gene expression analysis of animals from the same project showed a clear demyelination, and reduction of myelin-related proteins in the upper layers of the cortex.

The results from this project show that the model is suited for quantifying demyelination in the gray matter of mouse brains when cuprizone is used to model multiple sclerosis. In gray matter, it was found to be more specific and sensitive than conventional diffusion modelling. However, the results from rats show that the model is not as sensitive to smaller changes as histological examinations are.

Acknowledgements

I would like to thank everyone who have supported, helped and encouraged me in my work on this thesis. I could never have done this alone, and you are all most appreciated. I would especially like to thank:

My main supervisor Assoc. Prof. Renate Grüner for your positive encouragements, insightful feedback and invaluable competence in the field. Thank you for introducing me to the field of medical physics and MRI, and guiding me in both choosing and finishing this project.

My co-supervisor Dr. Tina Pavlin. Through your enthusiasm for the project you have been a great support. Thank you for always being available, for guiding me in the scanning of the animals, supporting me in the data analysis, and answering all my questions. There would be no thesis without you.

Dr. Stig Wergeland for helping me to understand MS, the nervous system and animal models. Thank you for presenting everything in a way even a physicist can understand, and not least for providing the mouse brains and histology for the project. My thanks also go to the 24 mice who were sacrificed for this project, without you this could not have been done.

Dr. Sune Jespersen for providing the model for the project, and guiding us in understanding it.

My thanks also go to everyone at MIC for welcoming me to the building, and to the security staff at HUH for allowing me access the lab after closing hours. As well as everyone in my office at the Physics Department who have provided great conversations over the last years.

My parents, for believing that my work is important and interesting, even when they do not understand a single word.

My dear friends who have shown a great enthusiasm for my project, helped me in matters great and small, and provided cake and encouragements when needed.

Finally, my boyfriend Jostein who has been nothing but supportive, patient, encouraging, and always with a strong belief that I could do it.

Contents

List of Abbreviations

ADC Apparent Diffusion Coefficient
CC Corpus Callosum
cDTI colour coded Diffusion Tensor Imaging
CNR Contrast-to-Noise Ratio
CPZ Cuprizone
DC Diffusion Coefficient
DGM Deep Gray Matter
DTI Diffusion Tensor Imaging
DWI Diffusion Weighted Imaging
EPI Echo Planar Imaging
ETL Echo Train Length
FA Fractional Anisotropy
FID Free Induction Decay
FOV Field-of-View
FSE Fast Spin Echo
FWHM Full Width at Half Maximum
GM Gray Matter
GRE Gradient Recalled Echo
MD Mean Diffusivity
MRI Magnetic Resonance Imaging
MS Multiple Sclerosis
MTI Magnetization Transfer Imaging
MTR Magnetization Transfer Ratio
PBS Phosphate Buffered Saline
PD Proton Density
PPMS Primary Progressive Multiple Sclerosis
RARE Rapid Acquisition with Refocused Echoes
RF Radio Frequency
RMS Root-Mean-Square
RRMS Relapsive Remitting Multiple Sclerosis
SE Spin Echo
SI Signal Intensity

SNR Signal-to-Noise Ratio
sPFG single Pulsed Field Gradient
SS-EPI Single Shot Echo Planar Imaging
TE Echo Time
TR Repetition Time
TrD Trace of D
VR Volume Ratio
WM White Matter

List of Figures

List of Tables

Chapter 1

Introduction

This chapter introduces the basic principles used in the thesis. The first section covers the pathological and anatomical knowledge that is necessary to understand the MS disease progression. The anatomy section includes nerve cells, the central nervous system, and white and gray matter. In the pathology section, the fundamentals of multiple sclerosis are covered, the disease progression, its microscopic characteristics, the disease detection and treatment, and animal models of the disease. Section two is on the fundamentals of magnetic resonance imaging (MRI), including generation of the signal, formation of images, and different imaging sequences. The third section of the chapter concerns diffusion, and how it is used in MRI. The section ends with a description of the biophysical model that is applied in this project, and a short comparison to conventional models. The chapter is concluded by the motivation.

1.1 Multiple Sclerosis

1.1.1 The Nervous System

Neurons

The nervous system consists of the central and the peripheral nervous systems, made up of neurons and neuroglia cells. The neurons transmit signals between different parts of the body, and are responsible for voluntary and involuntary actions. One of the tasks of the neuroglia is to support and protects the neurons [1]. The central nervous system consists of the brain and spinal cord, while the peripheral covers the rest of the body.

The neuron consists of a cell body called the soma with a cell nucleus, dendrites which spread out from the soma, and one axon that branches out at its end. A neuron usually has multiple dendrites that branch out to cover large areas, but only one axon,

as shown in figure 1.1. The axon leads electrical signals, usually from the soma, to one of its branches that ends in a bouton. A bouton is a small swelling that is placed close to the other neuron's membrane. The contact area is called the synapse, and is where the information is transmitted. This transmission is done by freeing signal molecules in the bouton that affect the receiver neuron. The synapse can be placed on both soma and dendrites, but a synapse on the soma will have a bigger influence on the neuron. The sum of the effects of all the synapses on a neuron determines its activity level.

Neurons vary both in the shape of the soma, and the length, branching and amount of dendrites. The area the dendrites cover indicates how many other neurons that neuron can be contacted by. In the neurons there is also a network of proteins that make up the cytoskeleton, a structure that maintains the shape of the cells [2].

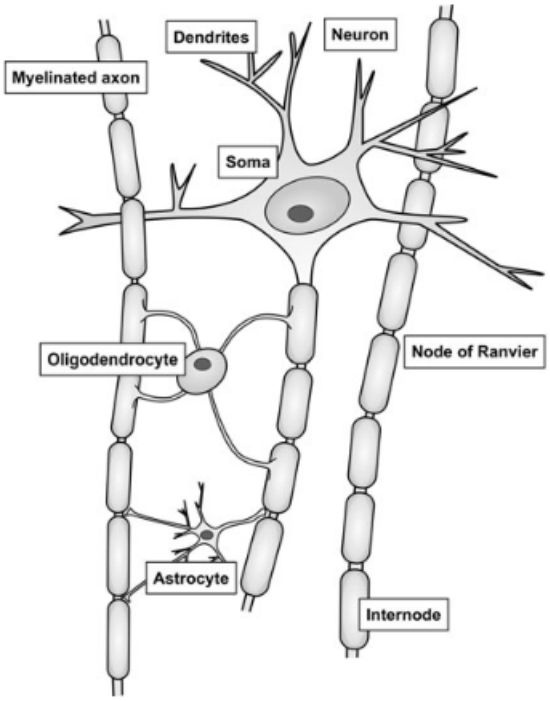

Figure 1.1: Schematic drawing of the components in neuronal tissue [3]

Myelination and demyelination

An essential property of the nervous system is its ability to transfer information quickly over relatively long distances. The speed of an electrical impulse within a nerve depends partially on the thickness of the axon, but mainly on its degree of myelination. Myelin consists mostly of lipids, and forms cylindrical bilayer sheaths around the axon. Between each myelin sheath there is a small gap where the axon is myelin free, called the node of Ranvier. The myelin reduces the loss of current to the environment, allowing the signal

to "jump" quickly between the nodes. The conduction velocity in myelinated axons approaches 120 m/s, while in umyelinated axons the velocity is less than 1 m/s [4].

Each myelin sheath consists of many thin layers of cell membrane, created from a type of glia cells that convolute the cell membrane around the axon. In the central nervous system, the myelinating glia cell is the oligodendrocyte. In demyelinating diseases, the most common one being multiple sclerosis (MS), myelin sheaths are degenerated along with a loss of oligodendrocytes. This will hinder the signal transmission in the axon, and in the worst case cause neuronal death.

Gray and white matter

The nerve cells are not randomly distributed in the brain tissue. The somas form functional groups called nuclei. Gray matter consists mainly of nuclei, as well as dendrites, glia cells and capillaries (small blood vessels). The deep gray matter is characterized by nuclei groups responsible for different tasks. In the cortex there is a layered structure in the gray matter, with an axon and dendrite density that decreases with distance from the corpus callosum . White matter is mostly made up of myelinated nerve fibres, which is the reason it appears white. However, it is important to remember that there are no clear boundaries between the regions, and there will be some axons in grey matter, and somas in white. The mouse (gray matter) cortex is estimated to contain near equal parts axons and dendrites [5]. Some gray and white matter regions of the mouse brain can be seen in figure 1.2.

1.1.2 Multiple Sclerosis

Multiple sclerosis (MS) is a chronic, inflammatory and demyelinating disease that affects the central nervous system of humans. The disease often starts in adults in their 20s and 30s, with big geographical variations. Northern Europe is one of the areas where MS is most prevalent. In Norway the disease affects 200/100 000 individuals, and there are around 10 000 MS patients total [7].

Together with medical history, neurological examination, and analysis of spinal fluid, MRI plays an important part in diagnosing MS. It is also used in monitoring the progress of the disease, and in medical research related to MS.

Disease progression

There are two main forms of MS, relapsing-remitting (RR) MS and primary progressive (PP) MS. A majority (80-90 %) of patients get RRMS [7], and may also progress to secondary progressive MS. RRMS progresses through unpredictable relapses with symptoms from different parts of the nervous system. The relapses are followed by complete or partial remission, and then new relapses at various time intervals. This usually leads to an increasing amount of disability over time. PPMS is characterized by a steady progression of disability from the début of the illness, with some stable periods, but no regression. Plots of the typical disease progressions are seen in figure 1.3.

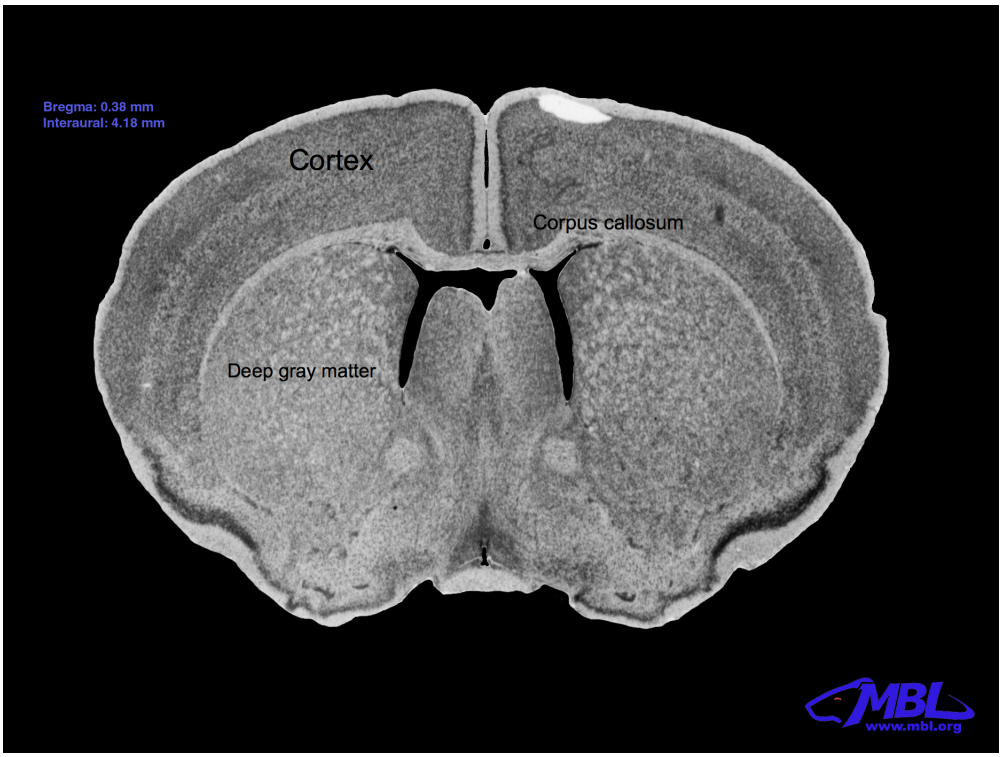

Figure 1.2: Axial slice of healthy mouse brain from a mouse brain library
The gray matter areas are the cortex and deep gray matter, while corpus callosum is white matter [6]

Usual symptoms of MS include visual impairment, disturbance in the motor skill and sensibility, bowel- and bladder dysfunction, fatigue, and cognitive failures or dysfunction giving reduced short time memory and a lessened ability to reason, learn and solve problems. The disease affects family life, the ability to work, social activities, and the general quality of life. Anxiety and depression is relatively common in MS patients, and, as a consequence, they have an increased suicide rate [7].

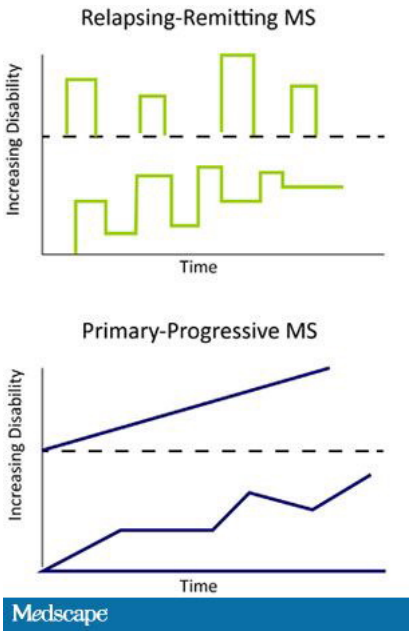

Figure 1.3: RRMS and PPMS.
In patients with RRMS the amount of disability will vary over time with clear relapses and remissions. In PPMS there are no relapses and a steady increase of disability, with no remission.[8]

Pathology and physiology

MS can be seen macroscopically in multiple lesions in the white and gray matter. A lesion is created in hours and causes early damage to the blood-brain barrier. The damage leads to a leak and a local oedema. The macroscopic lesions can be seen both in MRI, and in histology (the study of the microscopic anatomy of cells). Microscopically, the lesions are characterised by the demyelination that occurs in both white and gray matter due to inflammation and oligodendrocyte loss.

Demyelination and inflammation can also lead to axonal damage and loss, both in chronic and active lesions. In the chronic lesions there are also much fewer oligodendrocytes, and a scar tissue called gliosis is created. Permanent damage to the nerve cells leads to a decreased ability to transfer signals, which causes to varying degrees of permanent disability.

Remyelination occurs in both active and chronic lesions, partially due to the inflammatory process which stimulates remyelination and limitation of the myelin damage in the lesions. The main part of the remyelination is done by oligodendrocytes, but stem cells in the central nervous system are also involved in the process.

MRI and MS

Through MRI examinations, MS activity can be documented, and the location of lesions determined. Lesions appear differently in MRI depending on the MRI contrast used, and different techniques can be used to explore different aspects of the disease. Through serial examinations it has been shown that activity in the form of new lesions can be seen 5-10 times more often in MRI than what is recognised as a relapse in an untreated patient. The lesions are seen both in the brain and the spinal cord, but most commonly in the brain. Significantly more activity is seen in patients with RRMS, compared to those with PPMS. [7]

Although traditional MRI methods have a high sensitivity in revealing MS lesions, they are unable to distinguish between inflammation, demyelination and reactive glial changes in both lesions and normal-appearing white matter [9, 10]. While conventional T_1-methods have shown some potential for pathological specificness [11], quantitative methods such as DTI and MTI are by far the most commonly used.

Treatment

There is no known cure for MS, and so the treatment focuses on slowing down the progression of the disease and limiting the damage done by a relapse. The treatment of MS consists of relapse treatment, preventive disease modulation, and treatment of the symptoms [7]. Relapse treatment can shorten the relapse, thus reducing the damage done by it. The disease modulation treatments have been shown to decrease the relapse rate by up to 50 percent for RRMS patients [7], but has given no documented effect on PPMS patients. In the early stages of the disease there is a high capability of repair and remyelination, but as the disease progresses there is more axonal loss, and the treatment is at later points no longer effective.

The cuprizone model

MS is an exclusively human disease, but several experimental models in lab animals exists. The models are complementary to each other, to cover all aspects of MS pathophysiology. The cuprizone model is a model of toxic demyelination. Exposing mice to cuprizone through the mouse chow will lead to selective oligodendrocyte death and subsequent demyelination. The degree of demyelination increases with the concentration of cuprizone, and the duration of the exposure. It is also dependent on age, gender and species of the mice [12]. Cuprizone gives specific myelin loss without oedema and inflammation. This makes it a very suitable model for investigating myelin loss and neuronal

integrity. The differences in the histopathology of animal lesions in gray and white matter have been suggested to occur similarly in the mouse cuprizone model and in humans. During and after the exposure, there will also be some degree of remyelination [12, 13].

While the cuprizone model is widely used in mice, it is less commonly used in rats. Rats generally have a greater resistance to cuprizone, and so the effect is often smaller, and a larger exposure is necessary. There is also less knowledge about the effect of cuprizone on rat gray matter, but studies have suggested that cortical damage is one of the earliest consequences of cuprizone exposure, and can be observed before white matter demyelination [14].

1.2 Magnetic Resonance Imaging

1.2.1 Basic Principles

Magnetization

Magnetic Resonance Imaging is an imaging technique based on the response of protons in biological tissue to external magnetic fields. All elementary particles have an intrinsic angular momentum called spin, this value is quantized, hence the spin can only have certain values. For any particle there are 2s+1 possible orientations, where s is the spin quantum number [15]. Nucleons have spin s=1/2. A nucleus will only have a net spin if it has an uneven number of nucleons. In "uneven" nuclei there will be an associated magnetic moment μ. The magnetic moment and the spin are related by the gyromagnetic ratio γ, as shown in (1.1)

$$\mid \mu \mid = \gamma\sqrt{s(s+1)} \tag{1.1}$$

where s is the nuclear spin quantum number, and s=1/2 for protons. Hydrogen, ^1H, has the largest gyromagnetic ratio of all nuclei, and thus the strongest magnetic moment. It is also the most abundant element in humans and animals. Both of these properties are exploited in MRI.

When a strong magnetic field B_0 (in MRI scanners typically between 1.5 and 7 T) is applied the spins will align parallel or anti-parallel to the field's direction. This is known as Zeeman splitting. The spins aligned with the field will have lower energy given by

$$E_\uparrow = -\frac{1}{2}\gamma\hbar B_0 \tag{1.2}$$

and the spins aligned opposite the field will have higher energy given by

$$E_\downarrow = +\frac{1}{2}\gamma\hbar B_0 \tag{1.3}$$

where $\hbar$ is Planck's constant. The energy difference between the two states is given by

$$\Delta E = E_\downarrow - E_\uparrow = \gamma\hbar B_0 \tag{1.4}$$

In MRI, the net magnetization $\mathbf{M}$ is observed, and it is given by the sum of all magnetic moments within a voxel or sample.

$$\mathbf{M} = \sum_{n=1}^{N_s} \mu_n \tag{1.5}$$

There will always be a small excess of spins in the lower energy state, and so $\mathbf{M}$ will be aligned with the magnetic field. The difference between the number of spins in each state is

$$\frac{N_\uparrow}{N_\downarrow} = e^{\frac{\Delta E}{KT_s}} \tag{1.6}$$

where K is the Boltzmann constant, and T_s is the absolute temperature [K]. The expression for the net magnetization is then found to be

$$\mathbf{M} = \frac{1}{2}(N_\uparrow - N_\downarrow)\gamma\hbar\overrightarrow{k} \tag{1.7}$$

when the magnetic field is parallel to the z-axis. $\overrightarrow{k}$ is the unit vector along the z-axis. From (1.4) and (1.6) an expression for $N_\uparrow - N_\downarrow$ is found

$$N_\uparrow - N_\downarrow = N_S\frac{\gamma\hbar B_0}{2KT_S} \tag{1.8}$$

where N_S is the total number of spins. By combining (1.7) and (1.8) the magnitude of the magnetization vector is found to be [16]

$$\mid \mathbf{M} \mid = \frac{\gamma^2\hbar^2 B_0 N_s}{4KT_s} \tag{1.9}$$

The flip angle

For an MRI signal to be generated $\mathbf{M}$ has to be perturbed away from its equilibrium position along B_0. This is done by adding energy in the form of a radio frequence (RF) pulse, exciting the system. The pulse is produced by a coil perpendicular to the B_0 field, and is described by

$$B_1(t) = B_1^e(t)e^{-i(\omega t+\varphi)} \tag{1.10}$$

where ω is the Larmor frequency, φ is the phase, and $B_1^e(t)$ is an envelope describing the shape of the field.

Excitation will cause the net magnetization to start precessing in the plane perpendicular to the field B_0 with a characteristic (resonance) frequency given by the Larmor equation

$$\omega = \gamma B_0[rad/s] \tag{1.11}$$

The precession of the magnetization leads to emission of observable RF radiation. A voltage is induced in the receiver coil by the oscillating magnetization, according to Faraday's law of induction

$$\epsilon = -N\frac{d\Phi_B}{dt} \tag{1.12}$$

where ϵ is the induced electromotive force, N is the number of turns of the wire in the coil, and Φ_B is the magnetic flux given by

$$\Phi_B = \int_A BdA \tag{1.13}$$

where A is an area limited by the circuit [17]. The signal detected by the coil is called a Free Induction Decay (FID) signal, see figure 1.4.

The strength and duration of B_1 determines the flip angle of $\mathbf{M}$. B_1 can also be written as the sum of two rotating vectors, B_1^+ and B_1^- which rotate with the same angular frequency Ω in opposite directions. Mathematically this is expressed as [16]

$$B_1 = B_1^+ + B_1^- = B_1 \begin{bmatrix} cos(-\Omega t) \\ sin(-\Omega t) \\ 0 \end{bmatrix} + B_1 \begin{bmatrix} cos(\Omega t) \\ sin(\Omega t) \\ 0 \end{bmatrix} = 2B_1 \begin{bmatrix} cos(\Omega t) \\ 0 \\ 0 \end{bmatrix} \tag{1.14}$$

A new Cartesian coordinate system (x', y', z') called the rotating frame can be defined that rotates around the z-axis of the fixed coordinate system (x,y,z) (the laboratory frame) along with the B_1^+-vector. From the rotating frame, an effective field B_{eff} can be defined

$$B_{eff} = B_0 + B_1 - \frac{\Omega}{\gamma} \tag{1.15}$$

When $\Omega = \gamma B_0$ the effective field only consists of the B_1^+ and B_1^- vectors. The magnetization is related to the effective field as given in the modified Bloch equation [16]:

$$\frac{\partial M}{\partial t} = \gamma M \times B_{eff} \tag{1.16}$$

In the rotating frame B_1^- will appear to rotate with an angular velocity 2Ω. Over time the rotating B_1^- will then have a negligible effect on the magnetisation, so the net effect of applying the RF-field B_1 for a time t_p is a precession of M around B_1^+ with an angular velocity

$$\omega_1 = -\gamma B_1 \tag{1.17}$$

resulting in M rotating by an angle

$$\alpha = \omega_1 t_p = -\gamma B_1 t_p \tag{1.18}$$

towards the xy-plane. This angle is the flip angle.

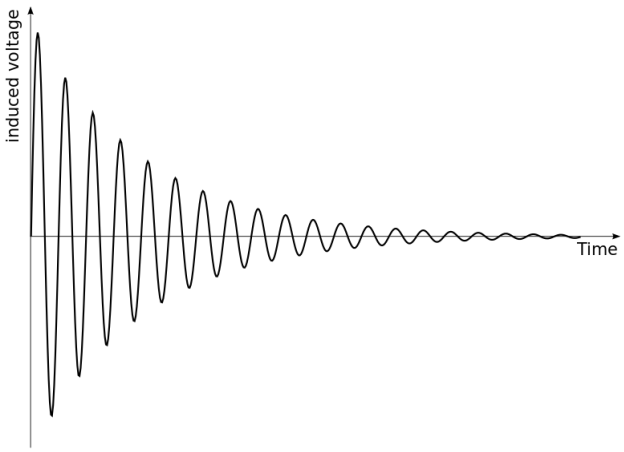

Figure 1.4: Free Induction Decay signal
[18]

Excitation and relaxation

Usually B_0 is defined as parallel to the z-axis, so that the xy-plane is perpendicular to the field and **M** before the RF excitation. After the excitation **M** will consist of two components, the longitudinal component parallel to B_0

$$M_z = M_0(1 - e^{t/T_1}) \tag{1.19}$$

and the transverse component perpendicular to B_0

$$M_{xy} = M_0 e^{t/T_2} \tag{1.20}$$

The precession of the M_{xy} (transverse) component of the magnetization around the z-axis gives the Free Induction Decay (FID) signal, as shown in figure 1.4.

When the RF pulse is turned off **M** will return to its equilibrium state along the B_0 direction, i.e the z-axis. These processes are called relaxation and happen simultaneously and independently for M_z and M_{xy}, as described by equations (1.19) and (1.20), and shown in figure 1.5. There are two different relaxation times, T_1 and T_2. T_1 describes the recovery of M_z, and T_2 describes the decay or loss of M_{xy}. T_2 relaxation is due to the loss of phase coherence caused by spin-spin-interactions.

T_1 and T_2 are tissue dependent and independent of each other. Water has long T_1 and T_2, while fat has short T_1 and T_2 [19]. In biological tissues, T_1 is usually between 300 and 1500 ms, while T_2 lies between 30 and 150 ms, at a 1.5 T main field [20].

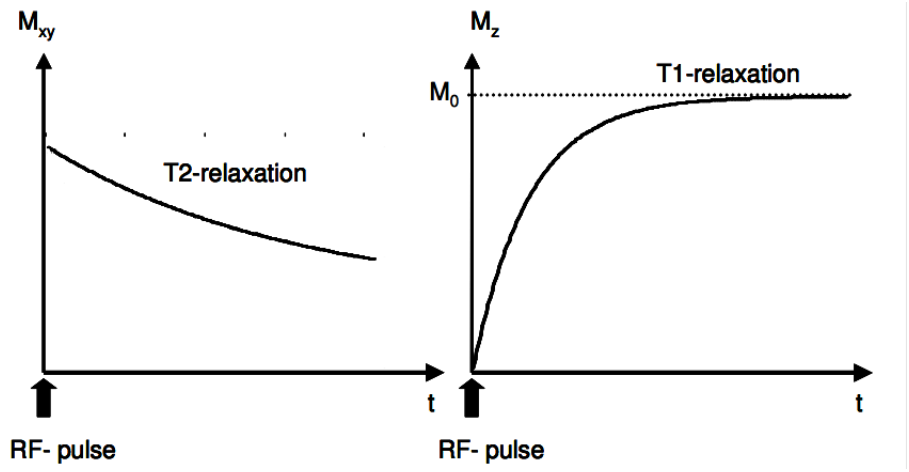

Figure 1.5: T_1 and T_2
Plots of the two different relaxation processes that occur after an RF excitation [16]

In traditional imaging, the FID signal is generated too soon after the excitation to allow spatial encoding of the signal [16]. So instead, the information is read from an echo of the FID signal. There are two main ways to generate the echo. Through multiple RF pulses (spin echo) and through magnetic gradient reversal (gradient echo). The imaging sequences that are most commonly used to create such echo signals are presented in section 1.2.3.

Image Contrast

While T_1 and T_2 are determined by the tissue type, the echo time (TE) and the repetition time (TR) are experiment specific parameters chosen to achieve different image contrasts. TE is the time delay from the excitation RF pulse to the signal readout (echo), while TR is the time between two successive excitation RF pulses, as shown in figure 1.6.

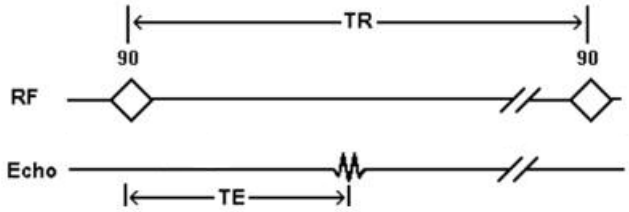

Figure 1.6: TE and TR.
TE is the time between the exciting RF pulse and the generated echo, TR is the time between two subsequent excitation RF pulses.[21]

T_1 weighting means that the contrast in images is primarily due to the differences in T_1 times of tissues. It is usually achieved by using a short TR to maximize the difference in T_1 times, and a short TE to minimize the T_2 effects. For a T_1 weighted image, acquired with a SE sequence the signal intensity S is

$$S \quad \propto \quad \rho_0(1 - e^{\frac{-TR}{T_1}}) \tag{1.21}$$

where ρ_0 is the proton density. A T_1 weighted sequence is commonly used for imaging anatomy and fat [19].

In T_2 weighting the contrast is mainly due to the different T_2 times of the tissues. Primarily, a long TR and intermediate TE are chosen to maximize the differences in T_2 times. The T_2 weighted sequence is best suited for imaging pathology [19, 22]. The signal intensity S is

$$S \quad \propto \quad \rho_0 e^{\frac{-TE}{T2}} \tag{1.22}$$

An image can also be Proton Density (ρ_0) weighted. The proton density depends on the density of hydrogen atoms in the tissues. To achieve proton density weighting, both the T_1 and the T_2 weighting are minimized by choosing a long TR and a short TE. The signal intensity is then mainly proportional to the proton density. An example of a human brain imaged with the different imaging contrasts is shown in figure 1.7.

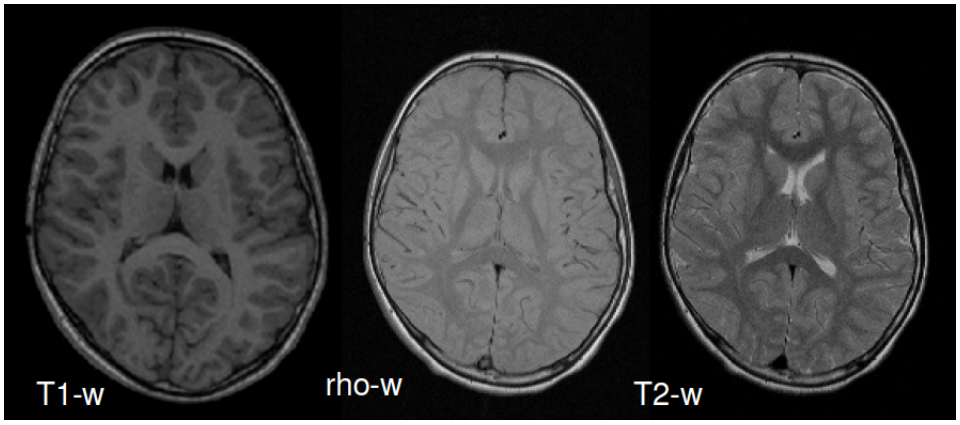

Figure 1.7: Sample SE images in the brain.
From right to left the sequence parameters were TR/TE = 500 ms/20 ms (T_1-w), 2200 ms/20 ms (rho-w) and 2200 ms/80 ms (T_2-w) [16]

1.2.2 Image formation

Gradients

Gradients are lower-strength, spatially-varying magnetic fields where the duration, strength and direction are all controllable. When a gradient field is applied, it creates a spatial variation in the homogeneous, constant main magnetic field. This leads to a variation of spin frequency that is dependent on position, and a dephasing of the spins over time. In the MRI system, there are gradient coils positioned in all three spatial dimensions, and these are used to generate imaging gradient fields.

Encoding and slice selection

The Larmor equation (1.11) states that the resonance frequency is proportional to the strength of the magnetic field. This property can be used to locate the spins along a gradient field, since the spins at different positions will have different resonance frequencies when the field is no longer uniform. A slice is chosen by applying a linearly increasing gradient along say the z-axis, at the same time as an RF excitation pulse is applied. The spins that have the same position along the axis (a slice) will all respond to the same resonance frequency. The slice thickness is dependent on the bandwidth of the RF-pulse, and inversely on the gradient amplitude, according to

$$\Delta z = \frac{\Delta\omega}{\gamma G_z} \tag{1.23}$$

where $\Delta\omega$ is the bandwidth, and G_z is the gradient amplitude.

When the slice is selected, further encoding is needed to localize the origin of a signal within the slice. Two waves can be differentiated by a difference in amplitude, phase or

frequency. The maximum amplitude is dependent on the proton density, so the gradients along the x- and y-axis are used to phase encode and frequency encode the signals.

Frequency encoding is done by applying a constant gradient during the readout of the signal. The frequency is dependent on the strength of the gradient. By measuring the amplitude of the generated signal, a one dimensional projection (along the gradient direction) of the sample is found as a function of frequency or position. When the strength of the applied gradient is known, the origin of the signal can be found. Phase encoding is done by applying a gradient before the readout to induce a phase difference. The phase difference makes waves distinguishable, and this is used to locate the source of each signal along the phase-encoding direction.

k-space

The k-space is a data matrix filled with the acquired echo signals (i.e. signal intensity) in the spatial frequency domain [16]. Collected data is stored temporarily in the k-space, before it is Fourier transformed to the spatial domain in order to create the final images. The data in the middle of the k-space contains the most information on SNR and contrast, while the data at the edges contain the most information on image resolution. Proper sampling of the k-space is fundamental to obtain good quality images, as illustrated in figure 1.8. Different sequences sample the k-space in different ways, depending on how the phase (typically y-axis) and the frequency (typically x-axis) encoding gradients are applied to k-space.

Nyquists sampling theorem states that the sampling frequencies must be at least two times greater than the maximum frequency of the continuous signal being sampled [23]. The sampling rate limits the available image resolution, and the size of the objects that can be scanned. When the sampling theorem is not fulfilled it is called under-sampling. Under-sampling leads to aliasing [23], meaning that two or more continuous time signals can be drawn through the discrete samples, and the input signal is not uniquely identified as shown in figure 1.9.

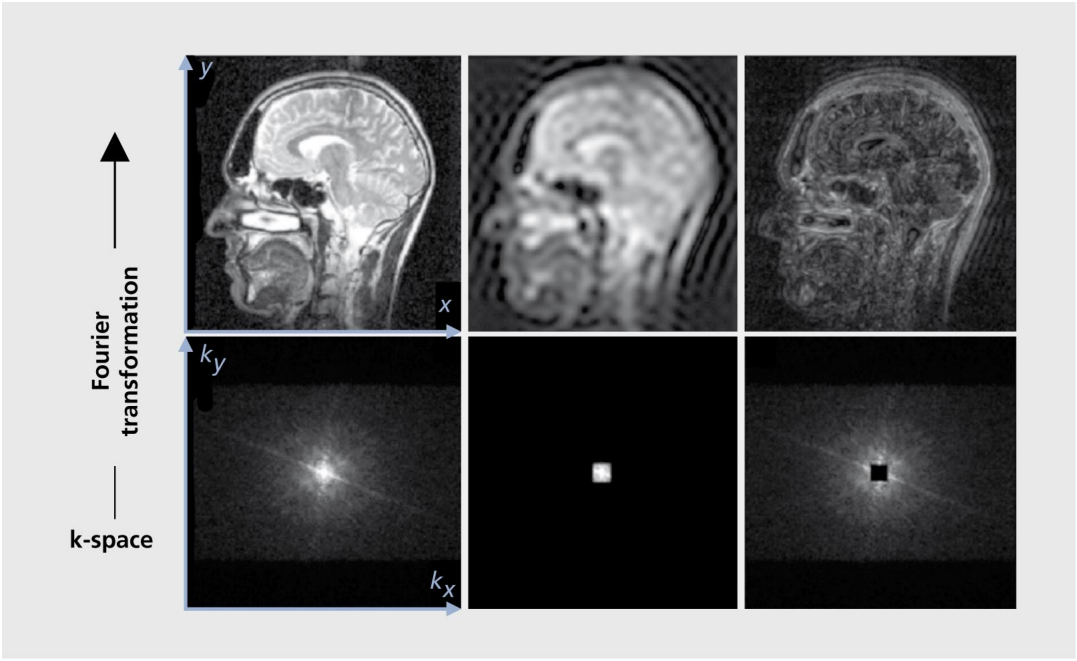

Figure 1.8: Fourier transforming the k-space
On the left a Fourier transform of the whole k-space is shown. In the middle, only the center of the k-space was transformed. On the right everything but the center of the k-space has been tranformed. [24]

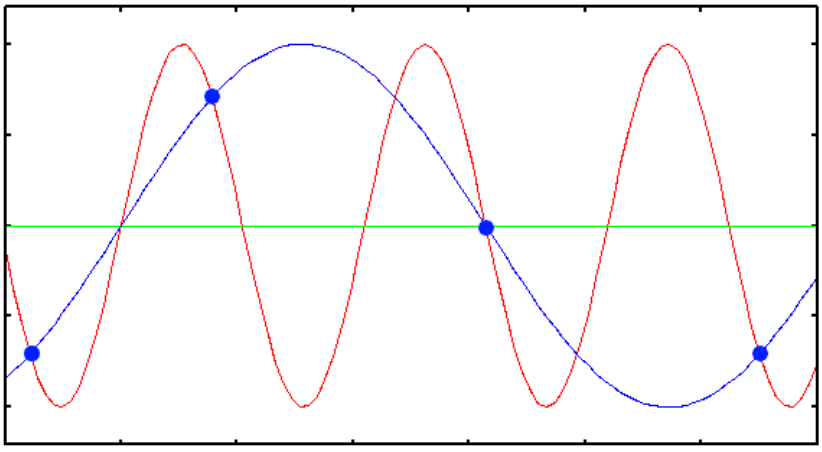

Figure 1.9: Aliasing.
The discrete samples from an under-sampled signal does not allow a unique reconstruction of the signal [25]

An artefact related to the k-space is Gibbs ringing, which can occur as lines parallel to abrupt changes in the object being imaged, as seen in figure 1.10. At such boundaries there is a jump between values, causing the Fourier sums to overshoot and oscillate after the jump [26]. These oscillations are the source of the lines that appear in the MR image. The artefact can be reduced by increasing the number of encoding steps in that direction, which can be hard to do in the phase-encoding direction, because it increases scan times [27]. A typical boundary where this artefact can be seen is between the edge of the sample and its surroundings.

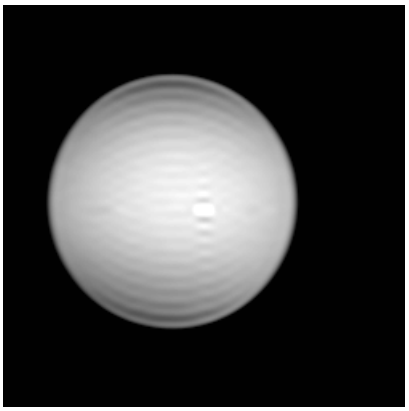

Figure 1.10: Example of Gibbs ringing in a phantom
[28]

Shimming

Many sequences, like diffusion weighted imaging and T_2* mapping, require the main magnetic field to be shimmed before they can be run. Shimming means adjusting the field gradients to make the magnetic field in the sample as homogeneous as possible. No magnets are perfect and inhomogeneities will appear over time. In addition, the samples are susceptible to magnetization which will alter the field [29]. There are various strategies for shimming, resulting in different qualities of the shims. Typically, whenever a new study or patient is created, a first order shim is included in the initial adjustments [30]. Second order shimming is then done prior to advanced scan protocols. The order of the shim comes from the mathematical model of the magnetic field, which is a Taylor series expansion [31]. For a first order shim, only linear terms are included, while for a first and second order shim, both linear and second order terms are included.

Shimming is also divided into passive and active shimming. Active shimming is done by special shim coils which have an adjustable current running through them. By adjusting the current correctly, the homogeneity of the field is improved. Passive shimming is done during the installation of the magnet. Metal plates are strategically placed on the surface or of the scanner to improve the homogeneity of the field [31]. To access the quality of the shim, an FID is collected and the FWHM (full width at half

maximum) of its spectrum is measured. The smaller the FWHM, the better the shim quality is.

Resolution

The resolution is the size of the pixels/voxels in an image. It should be chosen so that they are large enough to get a high signal intensity to noise ratio, but small enough so that important details can be seen in the image. The Field-of-View (FOV) of an image is the linear extent of the coverage of the sample being imaged [16]. The size of a pixel is decided by the Field-of-View and the number of frequency and phase encoding steps (forming a matrix) N_x x N_y. The resolution $\Delta \times \Delta y$ is found from the two equations below, (1.24) and (1.25), as is also seen in figure 1.11. In MRI it is common to use a matrix size of 256×256 or 128×128. Increasing the matrix size will decrease the signal intensity. Averaging may then be required (often making the scan times too long for practical purposes).

$$FOV_x = \Delta x N_x \tag{1.24}$$

$$FOV_y = \Delta y N_y \tag{1.25}$$

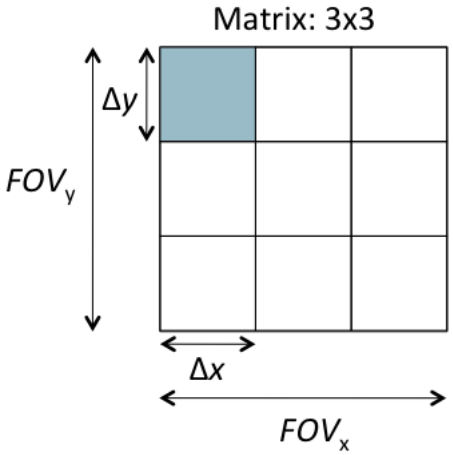

Figure 1.11: Resolution
The resolution is the size of each pixel, defined by the Field of View and the matrix size in each direction [19]

The size of the Field-of-View is also important. If an image FOV is defined that is smaller than the extent of the object being imaged, aliasing can lead to parts of the object outside the image FOV being back-folded into the image [16]. This may be a problem in the phase-encoding direction where the sampling rate can only be increased by increasing either N_y or FOV_y. In the readout direction the sampling rate is generally

high enough that back-folding is not a problem. Choosing the correct readout direction for the object imaging is therefore very important.

Signal-to-Noise ratio

The signal-to-noise ratio (SNR) is an important measure of image quality, for magnitude data it is given by

$$SNR = \frac{0.655S}{\sigma_{air}} \tag{1.26}$$

where S is the signal amplitude and σ_{air} the standard deviation of the noise outside of the object [19]. Many factors affect SNR including (but not limited to) the strength of B_0, the design of the RF-coil, proton density, voxel size, the number of averages and the readout time. Most of these affect both the signal strength and the amount of noise.

The reason MRI is performed at high magnetic field strengths can be seen from the relationship between SNR and B_0

$$SNR \quad \propto \quad \frac{B_0^2}{\sqrt{B_0^2}} = B_0 \tag{1.27}$$

There are several different designs of RF-coils, including volume coils for imaging organs deep in the body, and surface coils for imaging organs closer to the surface of the body. It is important to choose the right coil for a specific application, and to place it correctly to maximize SNR. The SNR is also proportional to the proton density of the tissue, since more spins (higher density) will give a stronger signal. This is also true for the voxel size; a big volume will contain more spins, so SNR is proportional to the volume of a voxel. The SNR can also be improved by averaging several measurements, but this will increase the total scan time.

$$SNR \quad \propto \quad \sqrt{N_{avg}} \tag{1.28}$$

By doubling the readout time the noise variance will be halved, improving SNR according to

$$SNR \quad \propto \quad \sqrt{T_{read}} \tag{1.29}$$

Combining (1.28) and (1.29) it is clear that the SNR is proportional to the square root of the measurement time. There will always be a compromise between a good SNR, scan times and resolution.

1.2.3 Imaging sequences

Different imaging sequences are used to sample the k-space. Two of the most fundamental ones are the spin echo sequence and the gradient echo sequence. Both can be accelarated to allow even more time efficient sampling of the k-space. The imaging sequences used in the current thesis are described next. Sequences that introduce diffusion weighting will be covered separately in section 1.3.3.

Spin Echo

The spin echo (SE) sequence uses two RF pulses to generate a signal echo. The first pulse is a 90° pulse that flips the magnetization completely into the xy plane. A frequency encoding gradient is then applied, causing the spins to dephase. The gradient is then turned off, and a second, 180 ° RF pulse is applied which flips all the spins (still in the xy plane). Finally a new frequency encoding gradient is turned on, causing the spins to rephase and generate an echo at t=TE. This is seen in figure 1.12. One line of the *k*-space is sampled between the pulses.

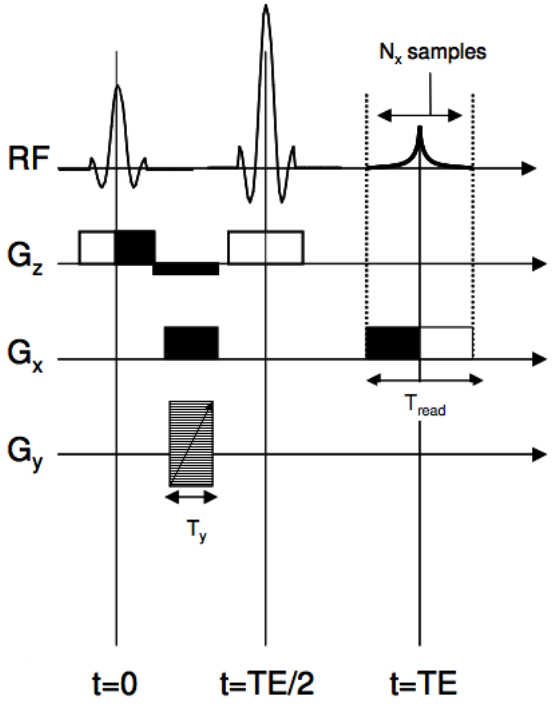

Figure 1.12: Spin Echo Sequence
Two frequency encoding gradients are used together with a 90 ° and a 180 ° pulse to dephase and rephase the spins in the xy-plane and generate an echo. [16]

Gradient echo

In a gradient echo (GRE) sequence a magnetic gradient is used to dephase and rephase spins, creating an echo. The gradient echo sequence also samples one line of the k-space after each RF pulse. The RF pulse can have a flip angle anywhere between 0 and 90°. The angle where maximum signal strength is achieved is called the Ernst angle, and is defined as

$$\alpha_{Ernst} = cos^{-1}(e^{\frac{-TR}{T_1}}) \tag{1.30}$$

If $\alpha > \alpha_{Ernst}$ the images will be T_1 weighted, and if $\alpha < \alpha_{Ernst}$ they will be proton density weighted.

To generate the images (read the k-space) and the echo, a constant (negative) frequency encoding gradient (G_x) is applied at the same time as the phase encoding gradient (G_y). This moves k(t) to the left of the k-space (minimum value of k_x), and the position on the k_y-axis determined by the phase encoding gradient. In the middle of the echo (at t=TE) k_x is zero. When G_y is turned off the polarity of G_x is changed. and one line of the k-space (from min. to max k_x) is sampled. The sequence is illustrated in figure 1.13, and it is repeated until all of k-space is sampled.

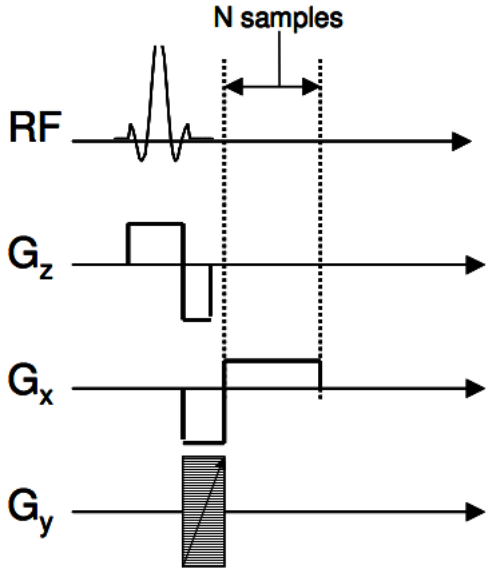

Figure 1.13: Gradient Echo Sequence
Magnetic gradients are used to generate the echo and read one line of k-space following an excitation RF pulse. [16]

Echo Planar Imaging

Echo Planar Imaging (EPI) is an extremely time efficient sequence where gradients are used for refocusing. It is also the most common sequence for diffusion weighted imaging [16]. Gradient echoes are used to sample the k-space, either under a spin echo for SE imaging, as shown in figure 1.14, or a FID for GRE imaging. When single-shot EPI is used the whole k-space is sampled with just one RF pulse, and a complete image can be generated in less than 100 ms [16]. However, the technique is very sensitive to inhomogeneities in the magnetic field, and other artefacts. One major advantage with SS-EPI is that it is very insensitive to motion of the subject. Multi-shot EPI where fewer lines are collected after each pulse has fewer artefacts, but it takes longer to construct the image.

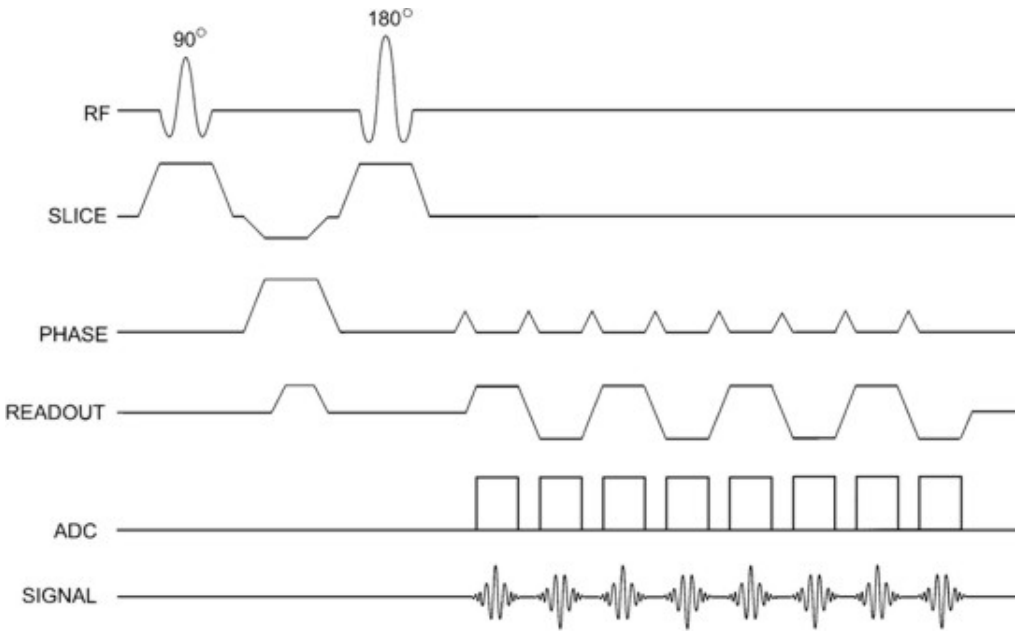

Figure 1.14: Echo Planar Imaging sequence
A spin echo based sequence where gradient echoes are used to efficiently sample the k-space after the excitation pulses. [32]

Fast Spin Echo

RARE, Rapid Acquisition with Refocused Echoes, is generally referred to as Fast Spin Echo (FSE). The sequence is shown in figure 1.15. The technique is based on a conventional spin echo sequence, but several k_y lines are sampled during each TR. All the lines are individually phase encoded after a 180° pulse. In theory, all the lines of the k-space could be read in a single TR (single-shot FSE) but this sets very high demands for stability and homogeneity in the system. Usually a segmented FSE technique is used where 8 or 16 echoes are acquired in each TR-interval [16]. The number of echoes acquired per TR is called the echo train length (ETL) or the turbo/RARE factor, and is an indicator of the speed increase of the technique compared to a conventional SE sequence. Segmented FSE is subject to artefacts related to variations or discontinuities in the signal level between subsequent segments. But other artefacts, such as blurring of the image due to T_2-relaxation, are reduced significantly compared to single-shot FSE [16].

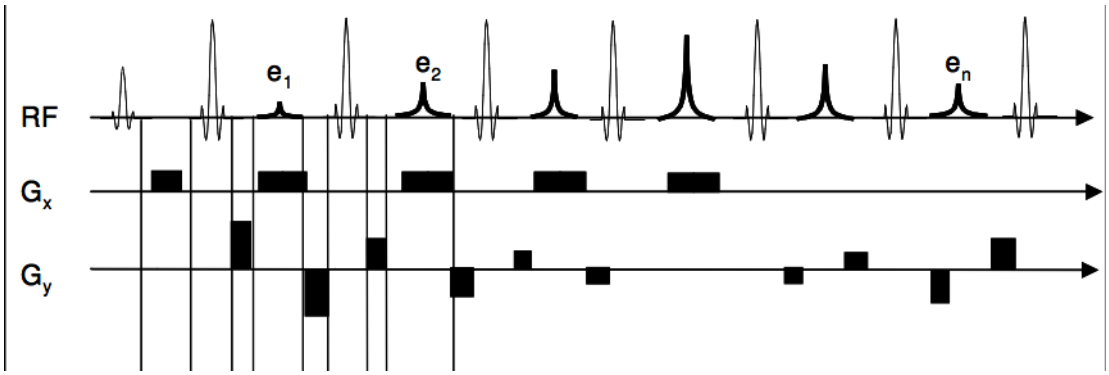

Figure 1.15: Fast Spin Echo sequence
Gradients are used to indiciduallt phase-encode each line of the k-space after each 180° pulse. [16]

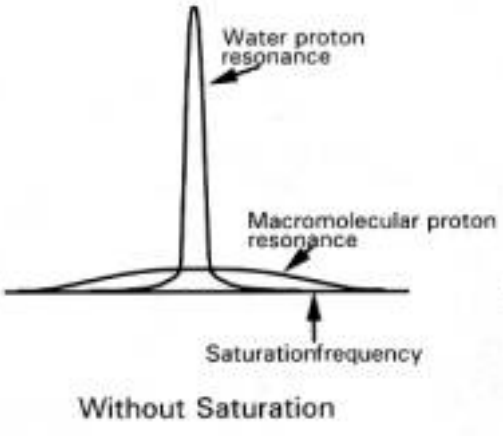

Figure 1.16: Lineshapes of bound and free protons
[33]

Magnetization Transfer Imaging

Magnetization Transfer Imaging (MTI) is a fairly new technique (first introduced in 1989 by Wolff and Balaban) [22] that has been shown to be very useful in quantification and characterization of tissues, particularly in the brain. MTI gives information about protons that are bound to macromolecules, which from a biological point of view are much more interesting than free protons in water. In white matter, the bound protons are primarily found in myelin. Free protons have a much narrower lineshape, while bound protons have a broader lineshape, as shown in figure 1.16.

To use MTI semi-quantitatively, a magnetization transfer ratio (MTR) has been introduced, defined as

$$MTR = 100\frac{(M_0 - M_S)}{M_0} \tag{1.31}$$

This ratio indicates the amount of bound protons in the sample by comparing a signal measured without saturation (M_0) to one measured with saturation (M_S). Saturation is loss of magnetization, induced by irradiating bound protons with an off-resonance RF-pulse. Due to the difference in lineshapes it is easy to irradiate only the bound protons by applying the pulses 1-2 kHz off-center, as is also seen in figure 1.16. When the bound protons are saturated there will be a transfer of magnetization between the free and bound protons, resulting in a reduction of magnetization and signal intensity for the free protons. The constant for the magnetization transfer rate when the bound pool is completely saturated is

$$k_{for} = \frac{MTR}{T_{1sat}} \tag{1.32}$$

Where T_{1sat} is the T_1-time after a saturating pulse. Water has a MTR of approximately

0 while tissues such has white matter have a high MTR of 30-60 pu and gray matter has intermediate values. Demyelination will lead to lower MTR, which is especially visible in white matter [22]. MS lesions typically have lower MTR than normal-appearing white matter due to demyelination, axonal loss and/or oedema [11]. A significant decrease of MTR has been shown experimentally in both corpus callosum (white matter) and deep gray matter when mouse brains were exposed to cuprizone [34]. In the same experiment, MTR values were shown to correlate well with myelin loss, as measured by histology.

1.3 Diffusion Weighted Imaging

Diffusion describes the Brownian motion of a particle. Each molecule moves randomly and collides with the other molecules. It is not possible to detect the path of a single molecule, but the collective motions can be studied, summing over all the diffusion paths within a certain time interval (i.e. the diffusion time). In MRI, the measurements are related to the dephasing of water molecules, and therefore signal attenuation with time, the degree of which is determined by the local tissue microstructure. Changes in tissues, such as the damage to the central nervous system that occurs in MS, affect the diffusion and can be detected with diffusion weighted MRI. If the diffusion in a medium is uniform in all directions it is called isotropic diffusion. When the diffusion is not uniform the medium is anisotropic. Biological tissues are anisotropic on a micrometer scale, and the diffusion is restricted by cell membranes and other biological barriers. This makes for a complex system where it is not the true diffusion constant D that is measured, but the apparent diffusion coefficient (ADC)[35].

1.3.1 Diffusion detection in MRI

The basic sequence for detecting diffusion is the Stejskal-Tanner sequence, a spin echo sequence with motion-sensitizing gradients [35]. After the 90° pulse in the SE sequence, a motion-sensitizing gradient is applied, giving the spins a phase that is dependent on the position along one axis. The gradient is then turned off, and the 180° pulse is applied, flipping the spins. An identical gradient is then turned on, causing the spins to rephase and generate an echo at t=TE. In the presence of diffusion, molecules will change position along the gradient, causing incomplete rephasing of the spins. This attenuates the strength of the echo, according to

$$\frac{S}{S_0} = e^{-bD} \tag{1.33}$$

where S is the attenuated signal echo amplitude, S_0 is the echo signal amplitude with the motion-sensitizing gradients turned off, D is the diffusion coefficient, and b is the so-called b -value (see below). D can be estimated by performing at least two measurements of S for different values of b , as shown in

$$\frac{S(TE, b_2)}{S(TE, b_1)} = e^{(b_1 - b_2)D} \tag{1.34}$$

If more measurements are performed, the curve is fitted using a least squares linear fit.

The SE sequence with motion-sensitizing gradients between the pulses is also called the (single) Pulsed Field Gradient (sPFG) sequence, and it is widely used to introduce diffusion weighting along one axis. The sequence is illustrated in figure 1.17. One disadvantage of the technique is that the sequence is very sensitive to motion artefacts, because of the large diffusion gradients that are used [36]. If a voxel contains locally anisotropic areas that are randomly oriented, the sPFG technique will not detect the local microstructural anisotropy, and the sample will exhibit overall isotropy. This can

be a problem in imaging of gray matter, where axons and dendrites are not as ordered as in the white matter [36]. This is another big disadvantage of sPFG.

The b-value

The b-value for the sPFG sequence is given by the equation below, and gives information about how sensitive the sequence is to motion.

$$b = \gamma^2 G^2 \delta^2 (\Delta - \frac{\delta}{3})[s/mm^2] \tag{1.35}$$

where γ is the gyromagnetic ratio, G is the gradient strength , δ is the duration of the gradient, and Δ is the time interval between the two gradient pulses.

There are two main ways to increase the b-factor:

1. Increasing the strength or duration of the gradient, thereby increasing the area under the pulse which is proportional to gδ. This increases the amount of relative dephasing along the gradient. When the phase difference between neighbouring spins is increased, the effect of diffusion, and thus the attenuation of the signal, will increase.

2. Increasing the diffusion time $t_{diff} = \Delta - \frac{\delta}{3}$, allowing for more diffusion to take place between the gradient pulses.

If only two measurements are made, and one is with b=0, it is very important to choose the right non-zero b value. If it is too small, the difference in attenuation will also be small. This makes it hard to accurately determine the slope, primarily due to noise in the data. However, if b is too large, the signal attenuation may be so significant that S lies in the noise region. There is no consensus on a perfect b-value, but it should lie between the two extremes, roughly at [35]

$$b = 1.1/D \tag{1.36}$$

The q-value

Another important factor in diffusion imaging is the q-value, which allows the creation of a displacement profile where molecular displacements can be read out directly. The q-value is proportional to the area under the gradient, which is its strength g multiplied by its duration δ. For narrow gradient pulses, the signal intensity S can be described in terms of q, and there will be a Fourier relationship between S and the displacement $\mathbf{R}$ [22]. The ideal gradient G(t) can then be described by a delta-function with area Gδ, so that q is defined by

$$q = \frac{\gamma}{2\pi} \int_0^t G(t)dt = \frac{\gamma}{2\pi} G\delta \tag{1.37}$$

The relationship between q and b is

$$b = q^2(\Delta - \delta/3) \tag{1.38}$$

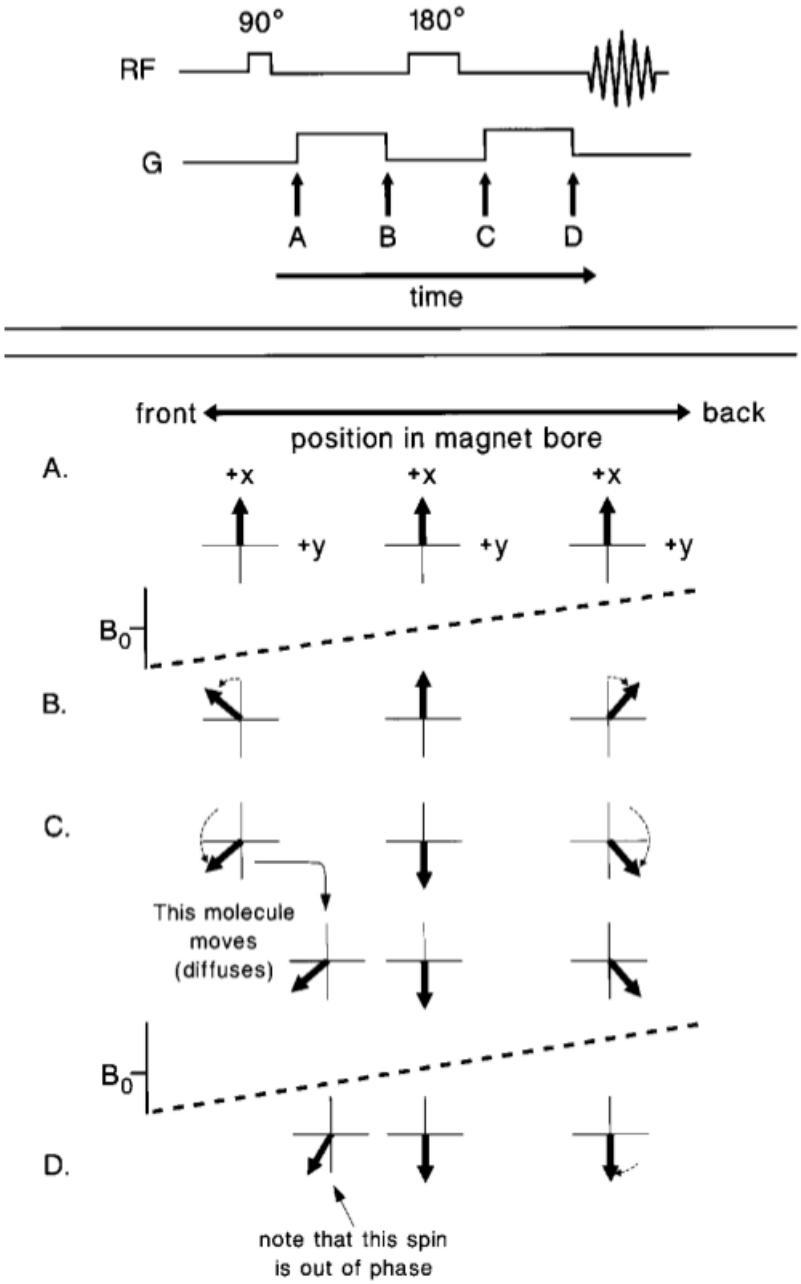

Figure 1.17: The single Pulsed Field Gradient sequence
The spin echo based sequence uses motion-sensitizing gradients that cause a diffusion dependent incomplete rephasing of the spins, and thus an attenuated echo and MRI signal. [35]

Data is typically acquired for a range of q-values, at constant values of Δ, mapping the signal S(q). A displacement profile P($\mathbf{R}, t_d$) is found from the Fourier transform of S(q). P gives the probability of a molecule having a displacement $\mathbf{R}$ at the time t_d. The q-space can be compared to the k-space where a range of points is sampled and Fourier transformed to create the MR image; q is used for diffusion gradients, in the same way that k is used for imaging gradients.

To get a good displacement profile resolution, a large range of q-values is needed. Strong gradients are required to reach high values of q. This poses difficulties, particularly in human whole body clinical imaging scanners.

1.3.2 Diffusion in biological tissues

Biological tissues are complex, and the diffusion is anisotropic and restricted by cell membranes. The RMS displacement for restricted diffusion (for one-directional movement) is given by (1.39)

$$< x^2 >^{1/2} = \sqrt{2(ADC)t_{diff}} \tag{1.39}$$

It is important to note that in restricted diffusion, the ADC will vary with the diffusion time. For a very short t_{diff}, few of the water molecules will reach a barrier, and the measured ADC will be very close to the true diffusion coefficient, D, which is found in free diffusion. As t_{diff} is increased, more molecules will be hindered by barriers, slowing the diffusion and reducing the diffusion coefficient. For long diffusion times, ADC is much smaller than the free diffusion coefficient. Over long time periods the ADC never becomes 0 in biological tissues, since the barriers are only partial, so the diffusion is slowed down but not stopped completely [35]. Water will find its way around and through cell membranes. However, in a diffusion experiment, membranes can be considered impermeable for the time scale of the measurement. In such a case the diffusion coefficient over the membrane is set to 0.

Anisotropy

Anisotropy means that the diffusion is dependent on direction. Water travels much faster parallel to an axon than perpendicular to it, since the myelin hinders diffusion [35]. Faster water motion means a higher ADC. A diffusion measurement is sensitive to motion in one direction (the direction of the motion-sensitizing gradient is applied along one axis). The ADC is therefore highly dependent on the diffusion weighting and the direction. If the ADC is measured in white matter, the orientation of the fibres with respect to the direction of the diffusion gradient will vary largely, and the measured ADC will not be a consistent measure of the diffusion properties of white matter.

To measure the anisotropy in the sample, and measure a spatially invariant quantitative diffusion coefficient, measurements along four (if there's axial diffusion symmetry) or sic axes are needed. In practice, more than six directions are needed, due to noise effects [16]. If this condition is fulfilled, it is possible to locate the major axis of diffusion,

and to measure the degree of anisotropy. The anisotropy will be the highest in matter where the orientation of the barriers (axons and dendrites) is the most structured and orderly. In the same way as the ADC, the measured anisotropy is dependent on t_{diff}. If the diffusion time is too short, one is unable to detect the anisotropy correctly.

There are a number of pathological processes that can change the molecular environment or modify tissue in ways detectable by diffusion imaging. Such processes include inflammation, cell swelling, demyelination, and axonal loss and reorganization. They all have in common that they change the diffusion properties in the regions they affect.

1.3.3 Diffusion analysis

Diffusion Weighted Imaging

Diffusion Weighted Imaging (DWI) is a simple and time efficient method that generates one diffusion weighted image. It is a qualitative method, not quantitative. The voxel intensities in the image are all measured for one b-value, and so the numerical ADC value corresponding to each voxel can not be found. However, by diffusion weighting the image, the signal intensity will depend mainly on the ADC of the water in each voxel, in the direction of the diffusion gradient [35]. Low ADC values, meaning low diffusivity, give high signal intensity, and vice versa. Anisotropy can be detected by comparing DWIs where the gradient has been applied in different directions. If an area is isotropic, it will have the same characteristics in all the images.

The b-value is chosen so that the difference in signal intensity between healthy and non-healthy tissues is as large as possible. The method is very sensitive to the positioning of the sample, and to the choice of acquisition parameters. It is also important to remember that the T_2-value is not eliminated. In DW images, signal increase due to T_2 can mask an increase in diffusivity, or be misread as a decrease in diffusivity. This is called T_2 shine-through effect [16].

ADC Maps

If numerical values of ADC are obtained in each voxel, an ADC map can be generated. In the map, each voxel will have an intensity that represents the ADC at that location. This makes ADC a quantitative measure. A series of images at different b-values are used to generate the map. The ADC of each voxel is calculated from an attenuation curve based on the signal intensities in the same voxel as a function of b. The intensity scale of the ADC map is opposite of the one in DWI. Areas with high water mobility are bright in ADC maps, but dark in DWI, and vice versa. ADC maps are somewhat time consuming to acquire and reconstruct, and often they are created offline after all the images have been collected [35]. ADC maps from DWI are heavily dependent on the choice of diffusion parameters, primarily the direction of the measurement. To generate maps that are rotationally invariant, at least 4 (6) diffusion directions have to be used, as explained in the Anisotropy section.

DTI - Diffusion Tensor Imaging

In an anisotropic medium, where it is assumed that the molecular displacements follow a multivariate Gaussian distribution, the diffusion can be described by a diffusion tensor (DT) [22], **D**:

$$\mathbf{D} = \begin{pmatrix} D_{xx} & D_{xy} & D_{xz} \\ D_{yx} & D_{yy} & D_{yz} \\ D_{zx} & D_{zy} & D_{zz} \end{pmatrix} \tag{1.40}$$

For uncharged molecules like water, there is no interaction between the spins and the DT is symmetric. Symmetry in DT means that the diffusion along an axis is invariant under reflection of the axis, e.g. $D_{xz} = D_{zx}$. DT can then be defined by the six elements $D_{xx}, D_{yy}, D_{zz}, D_{xy}, D_{xz}, D_{yz}$. The first three are the diffusion constants along the main axes of the frame of reference, the last three give the effect on the diffusion along j from the gradient along i; i,j=x,y,z. In an anisotropic media, DTI is preferable over simple DWI since it provides information on the diffusion's dependence on direction [22]. DTI is both quantitative and independent on the orientation of the sample within the scanner (rotationally invariant). At least six diffusion weighted measurements along different axes (e.g. x,y,z,xy,yz,xz) are needed to calculate **D**. The Stejskal-Tanner formula becomes

$$ln[\frac{S(TE,b)}{S(TE,0)}] = -\mathbf{b{:}D} \tag{1.41}$$

$$b_{ij} = \gamma^2\delta^2(\Delta - \frac{\delta}{3})G_iG_j; i,j = x,y,z \tag{1.42}$$

where : is the generalized dot product between the two matrices.

The diffusion tensor can then be transformed into a new matrix:

$$\mathbf{D'} = \begin{pmatrix} \lambda_1 & 0 & 0 \\ 0 & \lambda_2 & 0 \\ 0 & 0 & \lambda_3 \end{pmatrix} \begin{pmatrix} \varepsilon_1 \\ \varepsilon_2 \\ \varepsilon_3 \end{pmatrix} \tag{1.43}$$

where $\varepsilon_1, \varepsilon_2$ and ε_3 are the eigenvectors of **D** and represent three different directions, along which the displacements are independent of each other. λ_1, λ_2 and λ_3 are the eigenvalues of **D** and the ADC values corresponding to the eigenvectors. The eigenvectors and -values are unique for every DT. Conventionally the DT is made so that ε_1 represents the main direction of the diffusion, and is aligned with the fibres in the sample [22]. λ_1 then gives the maximum diffusion in each voxel. One of the main advantages of the rotational invariability that is made possible by a diagonalized DT, is the reproducibility of the measurements.

Scalar Invariants of D

The information that is contained in the three eigenvalues can be combined in different ways.

The mean diffusivity (MD) is given by the average of the eigenvalues, and is a convenient way of summarizing the diffusion properties in one voxel.

$$MD = \frac{\lambda_1 + \lambda_2 + \lambda_3}{3} = \frac{Tr\mathbf{D}}{3} \tag{1.44}$$

Tr$\mathbf{D}$ is called the trace, and is simply the sum of all three eigenvalues. The mean ADC is the average of the ADC values along all three spatial directions. If the imaging gradients have little influence $< ADC > \approx MD$, the mean ADC is given by

$$< ADC >= \frac{ADC_x + ADC_y + ADC_z}{3} \tag{1.45}$$

Another useful measure is the fractional anisotropy (FA), which is an estimate of what fraction of $\mathbf{D}$ is due to anisotropic motion. When FA is 0, there is complete isotropy, and when it is 1, the medium is cylindrically symmetric and $\lambda_1 >> \lambda_2 = \lambda_3$. FA is visually easy to interpret, white matter is white and gray matter is gray in the visualization, but it gives no information about the direction of the anisotropy. The fractional anisotropy is also rotationally invariant. [16].

$$FA = \frac{\sqrt{(\lambda_1 - < \mathbf{D} >)^2 + (\lambda_2 - < \mathbf{D} >)^2 + (\lambda_3 - < \mathbf{D} >)^2}}{\sqrt{\lambda_1^2 + \lambda_2^2 + \lambda_3^2}} \tag{1.46}$$

A DTI color map (cDTI) will give information on both the fractional anisotropy and the principal diffusion directions. In the map three colors are used to indicate the principal diffusion direction:

Red = Left - Right, Blue = Head - Feet, Green = Anterior - Posterior. The intensity of the colour reflects the fractional anisotropy.

1.4 Diffusion weighted imaging based models

1.4.1 Conventional models and their limitations

Conventionally, in clinical and animal scanners, the simple DWI models described earlier are used. ADC maps generated from DWI or DTI, as well as maps of anisotropy are commonly used. These simpler models have the advantage of short scan times and established protocols. While the diffusion weighted signal is sensitive to changes at a microstructural level, the models lack specificity. An increased ADC indicates less restricted diffusion in the area, but does not differentiate between processes like inflammation and demyelination, both of which occur in MS. Another issue with conventional techniques is their low sensitivity to gray matter changes. If one wishes to detect demyelination in gray matter, it can prove difficult due to the tissue complexity and the low volume fraction of myelin. By employing more complex diffusion models, one hopes to gain specificity and sensitivity to essential features of the tissue microstructure.

1.4.2 Jespersen et. al.'s model of dendrite density

While diffusion weighted imaging is sensitive to changes in tissue microstructure, there is a lack of specificity. A biophysical model can be used to connect the diffusion weighted signal to the microstructue, and to reveal specific properties by fitting the model to the acquired data. With such a model, the integrity of the nervous system can be assessed non-invasively with diffusion weighted MRI.

In 2007, Jespersen et. al. [37] proposed a model of diffusion outside and inside neurons (dendrites and axons), with an intent to describe the essential features of tissue microstructure that affect the water diffusion measured with MRI. While the model can be applied to both gray and white matter, it was developed to model the microstructure of gray matter. The model is based on three experimental observations.

1. The diffusion signal from white and gray matter is not mono-exponential. There is a clear deviation between the experimental signal and a mono-exponential model, especially for higher b-values. This suggests that there is a compartmentalization of water, since isotropic single department diffusion is mono-exponential.

2. The ADC in the brain is time independent for diffusion times over approximately 20 ms (corresponding to a diffusion length of 5-20 μm). The independence suggests that the compartments are either much smaller or much larger than this length.

3. There is a variation of water permeability of cell membranes that differs by orders of magnitude, giving compartmentalization. The model assumes that on the time-scale of the diffusion measurements, the permeability of the cell membranes in brain tissue is small enough that the membranes can be modelled as impermeable.

From these observations, a model was proposed where water in gray matter is primarily restricted (and compartmentalized) by dendrites. Dendrites are hundreds of micrometers long, and have a diameter of 0.1-2 μm. They can be modelled as long, thin and impermeable cylinders, as seen in figure 1.18. The diffusion not associated with cylinders is modelled as isotropic and Gaussian [37]. When the cylinders are modelled as impermeable for the relevant diffusion times, the signal can be written as a sum of the contributions from dendrites/axons and the isotropic diffusion. This sum gives a more biologically correct expression of the diffusion signal than for instance the "quasi-free" diffusion model that validates the diffusion tensor model.

For the model to be applicable, it is essential that the relation $q << 1/r$ is fulfilled, where r is the cylinder radius. For our experimental parameters this corresponded to $r << 1.3\mu m$ for the largest q-value. The diameter of a dendrite is typically $0.1 - 0.2\mu m$ [37].

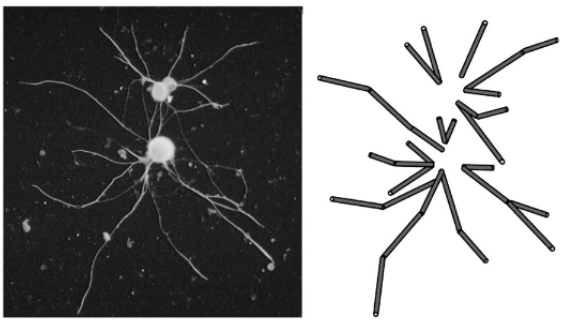

[37]

Figure 1.18: Model of neurons where dendrites and axons have been modelled as cylinders

Each cylinder has two separate diffusion constants, D_L parallel to the cylinder, and D_T perpendicular to it, $D_L >> D_T$. The orientations in one voxel are described by the fraction of dendrites in the solid angle $d\Omega$, which is defined by two spherical polar angles θ and φ. When it is assumed that the diffusion times are long enough to allow a Gaussian approximation of the diffusion within the cylinders, the contribution from each cylinder will be

$$S_{cyl}(\mathbf{q}, \Delta) \propto e^{-b(D_L cos^2\theta' + D_T sin^2\theta')} \tag{1.47}$$

where θ' is the angle between the diffusion gradient and the central axis of the cylinder. This contribution is summed over all cylinders. Any real function $f(\theta, \varphi)$ can be expanded in terms of complex spherical harmonics, and this is done to describe the heterogeneous cylinder orientation distribution.

$$f(\theta, \varphi) = \sum_{lm} f_{lm} Y_{lm}(\theta, \varphi) \tag{1.48}$$

where Y_{lm} is the Laplace series, a generalized Fourier series [38]. By using known properties of the expansion the expression for S_c, the contribution from all cylinders, can be written as

$$S_c(\mathbf{q}, \Delta) = \pi e^{-bD_T} \sum_{lm} f_{lm} C_l(b(D_L - D_T)) Y_{lm}(\theta, \varphi) \tag{1.49}$$

The diffusion not associated with the cylinders is modelled as mono-exponential and isotropic. An effective diffusion constant D_{eff} is experienced by the water molecules, and the approximation becomes

$$S_i(\mathbf{q}, \Delta) \approx e^{-bD_{eff}} \tag{1.50}$$

Introducing the water volume fraction associated with dendrites as ν, the sum of of the two contributions can then be written

$$S(\mathbf{q}, \Delta)/S_0 = (1-\nu)S_i(\mathbf{q}, \Delta) + \nu S_c(\mathbf{q}, \Delta) \tag{1.51}$$

$$S(b, \theta, \varphi) = S_0[(1-\nu)e^{-bD_{eff}} + \nu\pi e^{-bD_T} \sum_{lm} f_{lm} C_l(b(D_L - D_T))Y_{lm}(\theta, \varphi)] \tag{1.52}$$

Data from model application suggests that terminating the Laplace series at L=4 provides an adequate fit.

1.5 Motivation

The main objective of this thesis is to quantify the neuronal integrity of ex-vivo mice in a degenerative experimental model of MS. Cuprizone exposure is used to model the demyelination aspect of the MS disease progression. By applying a more complex biophysical model of water diffusion in tissue in the image acquisition and analysis, we aim to identify pathological changes with hgher specificity than what is achieved in conventional models. The main area of focus is the gray matter, a tissue with a complicated microstructure which requires more complex modelling than white matter. In MS and in the cuprizone model, demyelination occurs in both white and gray matter. Multiple steps were required for the evaluation of neuronal integrity:

- Understanding and adapting the complex biophysical model proposed by Jespersen to the diffusion properties of the underlying tissue microstructure as studied with advanced diffusion weighted magnetic resonance imaging.
- Performing and understanding ex-vivo preparation and imaging of mouse brains in a pre-clinical MRI system.
- Operating a pre-clinical 7T MRI scanner, optimizing the imaging protocol and minimizing artefacts.
- Scoring the quality of acquired images, and determining what data should be excluded from analysis.
- Analysing acquired data, and comparing the complex model with conventional diffusion imaging which provides ADC. Doing statistical analysis and interpreting the results. This also includes gaining knowledge of animal anatomy to properly define regions of interest.
- Repeating the above steps for a small group of rats in order to compare the applicability of the cuprizone model in rats and mice.

Chapter 2

Experimental Set-up and Method

2.1 Mice and rats

A total of 24 female mice (c57Bl/6, Taconic, Tornbjerg, Denmark) were aquired at 7 weeks of age. After acclimatization, 18 mice were randomized to five weeks of cuprizone exposure, by adding 0.2% cuprizone (bis-cyclohexanone-oxaldihydrazone, Sigma-Aldrich, St. Louis, MO, USA) to milled mouse chow (Rat and mouse no. 1 maintenance diet, from Scanbur, Special Diet Services, Karlslunde, Denmark). The experiment was conducted in accordance with the Federation of European Laboratory Animal Science Associations (FELASA) recommendations, and the protocol was approved by the Norwegian Animal Research Authority.

A total of 6 rats were also acquired and randomly divided into two groups (n=3). The rats in the cuprizone exposed group were fed milled standard laboratory chow containing 0.6 % cuprizone (Sigma-Aldrich, USA). This experiment was also conducted in accordance with FELASA recommendations, and the protocol approved by the Norwegian Animal Research Authority.

2.2 Preparation of brains

The total of 24 mice were split into 4 groups defined by the duration of the cuprizone exposure, as shown in table 2.1.

Control	3 weeks	5 weeks	Remyelinated
A1, A2, A3, (A4), A5, A6	C1, C2, D1, D2, E1, (E2)	C3, (C4), D3, D4, E3, E4	(C5), C6, D5, D6, E5, E6

Table 2.1: Groups of mice
Mouse brains and their respective groups, brains where the data was excluded from analysis are marked with brackets.

Mice were sacrificed after three (n=6) and five (n=6) weeks of cuprizone exposure, and four weeks after ending cuprizone exposure (n=6). The control mice (n=6) were sacrificed at the end of the experimental period, at 16 weeks of age, by a qualified scientist. Mice were euthanized by CO_2 asphyxiation, followed by intracardial perfusion with 4% formalin in phosphate-buffered saline (PBS). Mouse brains were extracted, immersed in 4% formalin, and stored at 4 °C until MRI scanning.

Rats were sacrificed after two weeks (n=3) of cuprizone exposure, and the control rats (n=3) were sacrificed at the same time. Rats were anesthetised by isoflurane gas, followed by intraperitoneal injection of pentobarbital and transcardiac perfusion with 9mg/ml NaCl (20ml/min for 5 min) and 4% (w/v) paraformaldehyde in PBS (PFA) (20 ml/min for 20 min). Fixated brains were removed from the skull, and stored in 4% PFA at 4 °C until MRI scanning.

Formalin is a solution of paraformaldehyde and water, and it is commonly used as a disinfectant, and for conservation of biological samples [39]. Fixation with formalin has been shown to reduce T_1, T_2 and MTR compared to values in-vivo [40, 41] and ex-vivo pre-fixation [42] in both white and gray matter. A shorter T_2 time means faster relaxation, and a lower signal intensity (SI) at a given time after excitation. Lower SI gives worse SNR and therefore image quality, so it was essential to properly rinse out the formalin before scanning.

Two days ahead of planned scanning, the brains were transferred to phosphate buffered saline (PBS), and brought to the lab where they were stored at room temperature until the time of scanning. PBS diffuses formalin out of the brain with an estimated maximum diffusion time of 1 mm of brain tissue per. hour [43].

Prior to scanning, the brain was transferred from PBS to Fomblin perfluoropolyether Y04 grade fluid to rinse off any excess PBS from its surface. It was then placed into an acrylic holder, as seen in figure 2.1. The holders were moulded in the same kind of tube that was used for scanning, in order to secure the sample, and prevent formation of air bubbles around the surface of the brain. The holder and brain were then placed in a Fomblin-filled tube, so that the brain was completely submerged in the oil. The function of the Fomblin oil was to keep the brains hydrated, and also eliminate external proton signal and susceptibility artefacts [10]. Neither Fomblin nor the acrylic holders produce any background MR signals, and they do not interfere with the signal from the brain.

After scanning, the brain was carefully dried off on a paper towel, before again being immersed in PBS for at least five minutes to rinse off the excess oil. It was then transferred to formalin and stored at 4°C, preserved for later histological assessment.

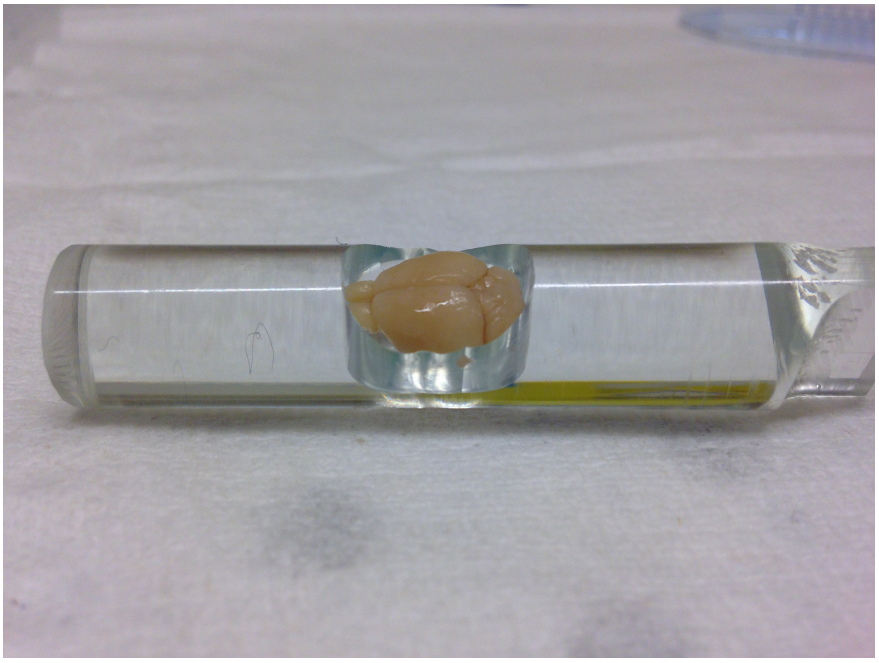

Figure 2.1: Mouse brain in acrylic holder

This procedure was done in the same way for both rat and mouse brains.

2.3 Scan protocols and equipment

2.3.1 Equipment

Figure 2.2: Bruker 7 T horizontal bore magnet
Photo by Anne Herdlevær

All scanning was performed using a 7 T horizontal-bore magnet (Pharmascan 70/16, Bruker BioSpin, Bruker Corporation, Germany), shown in figure 2.2. For the MRI of the mouse brains, a mouse head (23 mm ID) quadrature volume resonator (Bruker Corporation) was used, shown in figure 2.3. For the imaging of the rat brains, a phased array surface coil, shown in figure 2.4, was used in conjunction with a quadrature transmitter resonator (72 mm ID). The scanner software used was ParaVision 5.1 (Bruker Corporation).

Figure 2.3: RF mouse head quadrature volume resonator
Photo by Anne Herdlevær

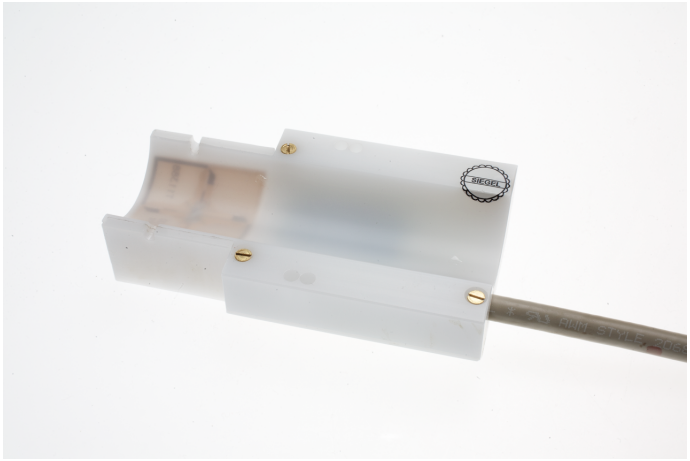

Figure 2.4: Rat head phased array surface coil
Photo by Anne Herdlevær

2.3.2 Protocol for mouse brains

Four brains, one from each group, were scanned on each scan day. There were a total of six scan days over a 10 day period. In addition, several brains were rescanned after being stored in formalin for approximately two months. The protocol included 12 pulse sequences, which can be divided into four groups: Positioning and slice selection, Shimming, Magnetization transfer imaging, and Diffusion weighted imaging. The total scan

time for each brain was approximately 4 hours.

Positioning and slice selection

	Name	Averages	TE/TR [ms]	Total duration	Matrix size
1	Tripilot	1	3.000/100.000	0min 12sec	256 × 256
2	TurboRARET2Coronal	2	12.000/3500.000	3min 44sec	256 × 256
3	TurboRARET2Sagittal	2	12.000/3500.000	3min 44sec	256 × 256
4	TurboRARET2Axial	2	12.000/3500.000	3min 44sec	256 × 256

Table 2.2: Protocol parameters - Positioning and slice selection (1) - Mouse brains

Name	FOV [cm^2]	# of slices	Slice thickness/ Interslice distance [mm]	Resolution [mm^2/pixel]
Tripilot	3.00×3.00	1	2.00	0.117×0.117
TurboRARET2Coronal	1.50×1.50	16	0.50/0.50	0.059×0.059
TurboRARET2Sagittal	1.80×1.80	24	0.50/0.50	0.070×0.070
TurboRARET2Axial	1.25×1.25	12	0.75/0.75	0.049×0.049

Table 2.3: Protocol parameters - Positioning and slice selection (2) - Mouse brains

The TriPilot, also called a localizer, is a very quick scan used to determine the placement of the sample with respect to the center of the magnetic field. Based on the information from this scan, the brain and coil were moved further in or out of the scanner, if necessary. It was also used to determine whether the tube had to be rotated to minimize the angle of the brain in the axial plane. Before the TriPilot was executed, the scanner automatically adjusted the resonant frequency, optimized the field homogeneity using first-order shimming coils, and adjusted the transmitter and receiver gains.

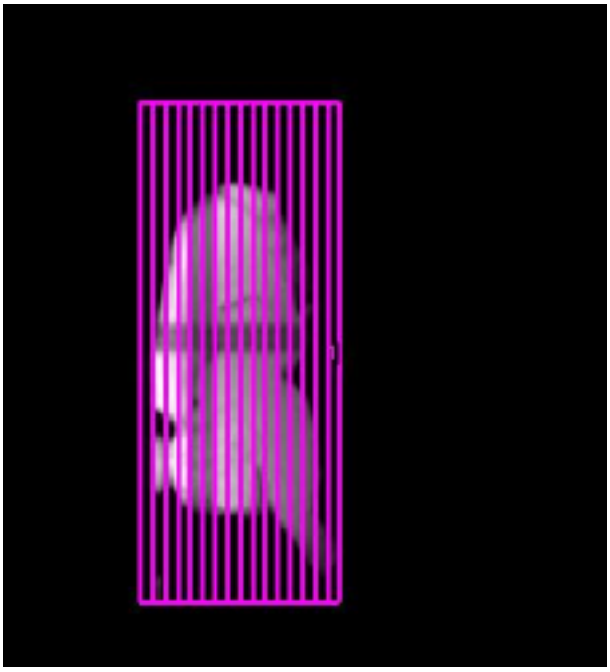

Figure 2.5: Example of slice positioning
Positioning of slices in the sagittal plane based on the Tripilot. The center of the magnetic field is seen where the two dark lines cross.

When the brain was correctly positioned in the scanner, three scans were run to determine angles to be used in the later scans, as presented in table 2.4. All slices were angled to ensure the axial slice was as symmetric as possible, adjusting with respect to the main axis of the brain in the coronal and sagittal planes. The slices were made to be as similar as possible to the ones that would be used in histology of the brains.

Scan	Reference Scan	Adjustments made
1 Tripilot	-	Position of brain in the scanner
2 Coronal	Tripilot	Position of the slices
3 Sagittal	Coronal	Angle H-L as shown in figure 2.6
4 Axial	Sagittal	Angle A-H as shown in figure 2.6, and angle L-H

Table 2.4: Initial slice adjustments

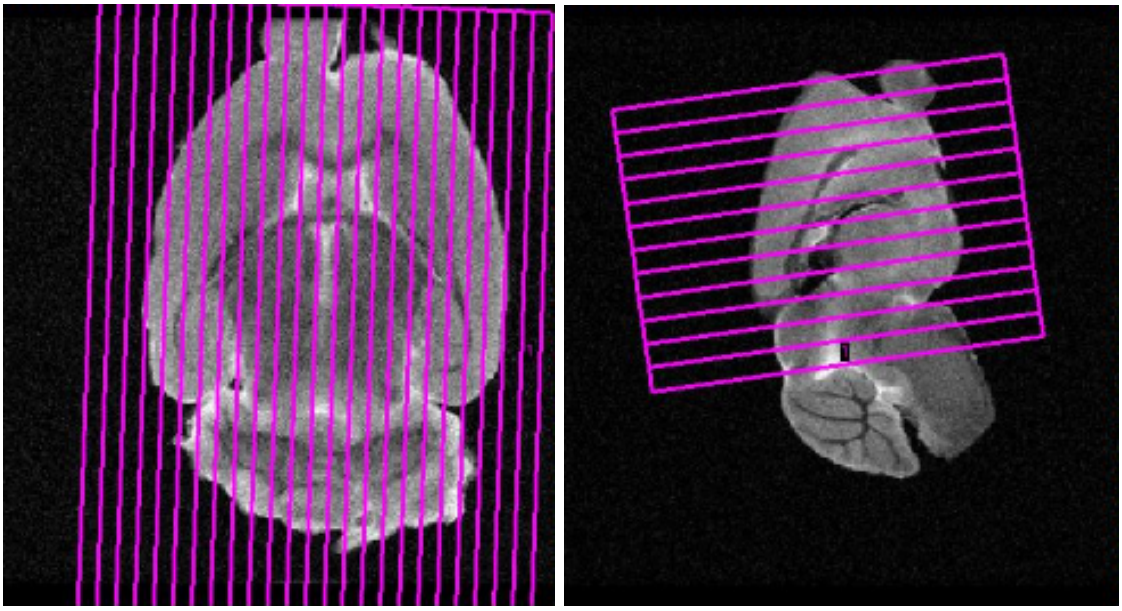

Figure 2.6: Angling of slices
Left: Angle H-L in the sagittal plane. Right: Angle A-H in the axial plane.

Shimming

Shimming is done to ensure a homogeneous field across the brain volume. Each brain is susceptible to magnetization, and thus able to alter the magnetic field. Additionally, inhomogeneities in the field appear naturally with time. The diffusion protocol used in this study is based on EPI, which is very sensitive to field inhomogeneities, as are the MTI sequences. Before performing these scans, a second-order shimming (xx,yy,zz,xy,xz,yz) of the field was necessary. For this purpose, the so-called Mapshim macro was used. The macro acquires a FieldMap, which is a map that shows the uniformity of the field across a chosen FOV, and then performs a global shim based on the map. To measure the quality of the shim, the FWHM was measured from the frequency spectra of a single-excitation pulse sequence called PressWaterline. The FWHM was measured before and after shimming, and for mouse brains it was maximum 15 Hz after shimming [30].

	Name	Averages	TE/TR [ms]	Total duration
5	PressWaterline	1	20.000/2500.000	2sec 500ms
6	FieldMap	1	2.000/20.000	1min 22sec
7	PressWaterline	1	20.000/2500.000	2sec 500ms

Table 2.5: Protocol parameters - Shimming - Mouse brains

The two PressWaterline scans were identical, and had the following geometry: Cube size 4×4×4 mm^3, resolution 0.98 Hz/pts. The cube was placed as to cover brain tissue only.

The FieldMap scan had a different geometry: FOV 2.00×1.80×1.80 cm^3, slice thickness 18.00 mm, 1 slice, matrix size 128×64×64, resolution 0.156×0.281×0.281 mm^3/voxel. The other protocol parameters are shown in table 2.5.

Magnetization Transfer Imaging

	Name	Averages	TE/TR [ms]	Total duration
8	TurboRARE3D	1	9.000/1500.000	6min 0sec
9	3DFLASHMT	8	2.235/28.500	10min 57sec
10	3DFLASHMT	8	2.235/28.500	10min 57sec

Table 2.6: Protocol parameters - MTI - Mouse brains

The MTI protocol consisted of three 3D scans with the following geometry: FOV 2.56×2.56×0.70 cm^3, slice thickness 7.00 mm, 1 slice, matrix size 128×128×30, resolution 0.200×0.200×0.233 mm^3/voxel. The other protocol parameters are shown in figure 2.6.

The first scan of the protocol was a 3D scan of the entire brain (T2-weighted TurboRARE sequence with RARE factor 16). The resulting images were used to co-register the the MTR maps to the brain anatomy. The remaining two scans were used to obtain MTR maps. For that purpose, a gradient-echo pulse sequence (FLASH, excitation pulse angle 10.0°), with and without the saturating pulse (+2500 Hz off resonance, Gaussian shaped, 7.5 μT strength, 15 ms duration) was used.

The MTI scan protocol used in this project was set up and tested in a previous project [34], that found a correlation between myelin loss evaluated by immunochemistry and MTR values in some parts of the brain. Collection of MTR data in this experiment will enable us to compare the MTR data with the results presented here from the DWI, as well as with the histological data from the corresponding imaging slices.

Diffusion Weighted Imaging

	Name	Averages	TE/TR [ms]	Total duration	δ/Δ [ms]
11	EPI_ DTI	1	23.000/3000.000	7min 0sec	5/10
12	EPI_ DTI_ greymatter	6	33.490/3000.000	3 hrs 18 min	6/20

Table 2.7: Protocol parameters - Diffusion Weighted Imaging - Mouse brains

The DWI protocol was based on Echo Planar Imaging, which is sensitive to field inhomogeneities, and also prone to motion artefact when used in combination with diffusion gradients. Using EPI for diffusion weighted imaging allows for relatively short scan times.

The main diffusion tensor imaging sequence had a scan time of over 3 hours. Before running this scan, a DTI scan was run that had a significantly shorter scan time, as shown in table 2.7. This shorter scan was helpful in checking the image quality and positioning of the sample. Both DTI sequences had the same geometry: FOV 1.25 cm×1.25 cm, slice thickness 0.75 mm, interslice distance 0.75 mm, 12 slices, matrix size 128×128, and resolution 0.098×0.098 mm^2/pixel. The geometry was the same as in the T_2-weighted axial images.

The EPI_ DTI scan had one b-value of 1000 s/mm^2, and 30 diffusion directions were chosen. In addition, 5 S_0 unweighted images were collected. EPI_ DTI_ greymatter collected data for 16 b-values ranging from 880 to 14080 s/mm^2, and for each b-value 10 diffusion directions were chosen. 5 S_0 images were acquired. The 16 b-values were 880, 1760, 2640, 3520, 4400, 5280, 6160, 7040, 7920, 8800, 9680, 10560, 11440, 12320, 13200 and 14080 s/mm^2.

2.3.3 Protocol for rat brains

Three control rat brains and three brains cuprizone exposed rat brains were scanned. Several of the brains were scanned twice to improve the slice positioning. All brains were scanned in a two week period. The protocol was very similar to the one used for scanning the mouse brains, however some smaller alterations were made. For instance, the image FOV had to be changed in order to cover the larger volume of the rat brains.

Positioning and slice selection

	Name	Averages	TE/TR [ms]	Total duration
1	Tripilot	1	3.000/100.000	0min 12sec
2	TurboRARET2Coronal	2	12.000/3500.000	3min 44sec
3	TurboRARET2Sagittal	2	12.000/3500.000	3min 44sec
4	TurboRARET2Axial	2	12.000/3500.000	3min 44sec

Table 2.8: Protocol parameters - Positioning and slice selection (1) - Rat brains

Name	FOV [cm^2]	# of slices	Slice thickness/ Interslice distance [mm]	Resolution [mm^2/pixel]
Tripilot	4.00×4.00	1	2.00	0.156×0.156
TurboRARET2Coronal	3.00×3.00	16	0.75/0.75	0.117×0.117
TurboRARET2Sagittal	3.00×3.00	24	0.75/0.75	0.117×0.117
TurboRARET2Axial	2.00×2.00	15	0.50/0.50	0.078×0.078

Table 2.9: Protocol parameters - Positioning and slice selection (2) - Rat brains

All four sequences had a 256 × 256 matrix. All other parameters are shown in tables 2.8 and 2.9. The brain position was adjusted and the slices oriented in the same way as for the mouse brains.

Shimming

	Name	Averages	TE/TR [ms]	Total duration
5	PressWaterline	1	20.000/2500.000	2sec 500ms
6	FieldMap	1	1.530/20.000	3min4sec
7	PressWaterline	1	20.000/2500.000	2sec 500ms

Table 2.10: Protocol parameters - Shimming - Rat brains

The two PressWaterline scans were identical, and had the following geometry: Cube size 4×4×4 mm^3, resolution 0.98 Hz/pts.

The FieldMap scan had a different geometry: FOV 4.00 cm × 3.00 cm × 3.00 cm, slice thickness 30.00 mm, 1 slice, matrix size 128×96×96, resolution 0.312×0.312×0.312 mm^3/voxel. The other parameters of the protocol are shown in table 2.10.

The shimming of the field was done in the same way as for mouse brains. The FWHM for rat brains after shimming was no higher then 20 Hz [30].

Magnetization Transfer Imaging

	Name	Averages	TE/TR [ms]	Total duration
8	TurboRARE3D	1	9.000/1500.000	6min 0sec
9	3DFLASHMT	8	2.235/28.500	10min 57sec
10	3DFLASHMT	8	2.235/28.500	10min 57sec

Table 2.11: Protocol parameters - MTI - Rat brains

All MTI scans had the same geometry: FOV 3.00 cm×3.00 cm×0.70 cm, slice thickness 7.00 mm, interslice distance 8.00 mm, 1 slice, matrix size 128×128×30, resolution 0.234×0.234×0.233 mm^3/voxel.

First was a TurboRARE sequence with a RARE factor 16, while the following two identical sequences were FLASH sequences with an excitation pulse angle 10.0°.

The saturating pulse used was +2500 Hz off resonance, Gaussian shaped, 7.5 μT strength, 15 ms duration. The other protocol parameters are shown in table 2.11.

The slices were chosen and the protocol executed in the same way as for the mouse brains.

Diffusion Weighted Imaging

	Name	Averages	TE/TR [ms]	Total duration	δ/Δ [ms]
11	EPI_ DTI	1	23.000/3750.000	8min 45sec	5/10
12	EPI_ DTI_ greymatter	6	33.490/3750.000	4 hrs 7 min	6/20

Table 2.12: Protocol parameters - Diffusion Weighted Imaging - Rat brains

Both diffusion sequences had the same geometry: FOV 2.00 cm×2.00 cm, slice thickness 0.50 mm, interslice distance 0.50 mm, 15 slices, matrix size 128×128, and resolution 0.156×0.156 mm^2/pixel. The rest of the protocol parameters are shown in table 2.12.

For the two DWI sequences the same geometry was used as in the axial T2-weighted scans. The EPI_ DTI scan was used to check that the positioning of the slices was good, and that there were no other problems with the scan. For this scan, one b-factor of 1000 s/mm^2, and 30 diffusion directions were chosen. 5 S_0 images with no diffusion weighting were acquired. EPI_ DTI_ greymatter_ rat collected data for the same 16 b-values as in the mouse brains. 5 S_0 images were acquired.

2.4 Image quality assessment

Several factors were considered to assess the quality of the diffusion weighted images, and to determine if any brains had to be excluded from the analysis. An initial step to ensure good image quality was the shimming protocol that proceeded the diffusion weighted imaging. All FWHM values were recorded before and after shimming, and scanning proceeded only for FWHM values below 15 Hz for mouse brains, and 20 Hz for rat brains. The noise level of each image was measured by calculating the mean noise of the five S_0 images in an ROI placed outside the brain volume, this was done using the Paravision 5.1 software. The signal intensity was compared to the noise level by plotting SI as a function of b-value, and the noise in the same plot. The signal intensity in all regions-of-interest should be above the noise region. Artefacts in the diffusion weighted images were observed in several of the brains. The amount of artefact was determined

visually through windowing (adjusting the displayed minimum and maximum signal intensity of the images) in the Paravision 5.1 software to amplify the artefacts. Both motion artefacts in the left-right direction, and Gibbs ringing in the anterior-posterior direction were seen. In the brains with significant motion artefact it manifested both inside and outside the brain volume, while the smaller artefacts manifested themselves only outside the brain. In addition, the maps of neurite density and the two diffusion coefficients were studied for signs of these artefacts.

2.5 Image data processing

2.5.1 Jespersen's complex gray matter model

The MatLab script used for preprocessing of data was provided by Sune Jespersen (CFIN/MindLab and Dept. of Physics and Astronomy, Aarhus University) and slightly modified to fit our acquired data. The script consists of three functions: fitscript.m, which loads data for each animal, specifies initial parameters of the model fit, and saves the output parameters. pixelwiseroifit.m, which prepares matrices for output parameters, calles on the fullmodel.m file to fit the data to model function pixel by pixel, and makes maps for all output parameters. fullmodel.m, which contains the full mathematical model that is applied.

In fitscript.m an image data matrix, a matrix of gradient values (gmatrix), and the standard deviation of the noise in the image as retrieved from the scanner were loaded for the specified animal. The data matrix was of the size [height (128), width (128), number of slices (12), number of diffusion directions (165)]. The entries gmatrix where the values were zero were used to find the 5 non-diffusion weighted S_0 images. The mean of these was found and used to normalize each image for all b-values in a chosen slice. The initial parameters and bounds of the least square fit were defined, before the pixelwiseroifit function was called on to perform the pixel-by-pixel fit to the model. The output matrices from this function were then normalized and saved.

pixelwiseroifit.m was called on to fit the diffusion model to the acquired data. The input parameters to this function were the normalized image data matrix, the model function (fullmodel.m), the inital fit parameters and bounds of the least square fit, the gmatrix, and specifying options for the least square fit. The function let the user define a polygonal region of interest (the whole brain) in the slice, and the model function was fitted for the pixels included in this ROI. Before fitting the function, empty 128×128 matrices par (model parameters), chi2 (resnorm of the least square fit), and algorithm (output info of the fit) were created. The matlab lsqcurvefit function was used to fit data to the model function in each pixel, with par, chi2, the residual, the exitflag, and output info of the fit in each pixel as the outputs. If exitflag$>$0 the exit condition was good, 18 parameter (par) maps and one chi2 map were made by assigning the output values to each pixel.

fullmodel.m was the input model function to the lsqcurvefit function. The input parameters to fullmodel.m were par, gmatrix, Delta and delta. In the function, b was cal-

culated from the gmatrix, Delta and delta. The model equation was then defined, as well as the 18 parameters that are included in the 4D par matrix. The important parameters for further analysis were par(1)=S_0, par(2)=f (1-neurite density), par(3)=extracellular diffusion coefficient, par(4)=longitudinal diffusion coefficient. Parameters 5 to 18 were spherical harmonics expansion parameters used in the model function. The map of par(2) was later inverted in matlab to be a map of the neurite density.

2.5.2 Conventional diffusion modelling

For all mouse brains, ADC maps were generated in a modified version of the matlab script used for the complex diffusion modelling. The input data and gradient matrix were changed to only include the data from the unweighted images and images generated at the two lowest non-zero b-values in all ten directions. In addition, the complex model was replaced by the simple diffusion equation $S = S_0 e^{-b(ADC)}$. The maps of ADC were generated by fitting pixel-by-pixel to the diffusion equation in the same way as for the complex model. The two model parameters defined in this model were the par(1)=S_0 and par(2)=ADC.

2.5.3 Selecting ROIs

The S_0 intensity image was used to define the regions-of-interest in each brain. The ROIs were manually selected using the MATLAB roipoly function. The positioning of the ROIs can be seen in figure 2.7. In the mouse brains the following three different regions were investigated: corpus callosum (CC), cortex and deep gray matter (DGM). For the cortex and the DGM, two ROIs were chosen from the same slice, one from each brain half. In DGM, the information from the two ROIs was averaged, and the resulting information was used in analysis. In the cortex the information from one of the ROIs was used in analysis.

The same ROIs were used in the rat brains, but with a different placement of the cortex ROI as seen in figure 2.7. The reason for this placement was that a surface coil was used in scanning the rat brains, and so the SNR was highest at the top of the brain.

2.5.4 Extracting image parameters

The means and corresponding standard deviations of the model parameters were extracted in the same way for advanced and conventional diffusion modelling. In the advanced model, the relevant parameters were neurite density, longitudinal diffusion coefficient, and the extracellular diffusion coefficient. In the conventional model, the relevant parameter was the apparent diffusion coefficient. In the data processing, maps of all these parameters were generated for each brain. Once ROIs were defined in the S_0 intensity image, they were applied to all other maps. The matlab functions mean2 and std2 were used to extract the mean values and their corresponding standard deviation from each ROI in all maps.

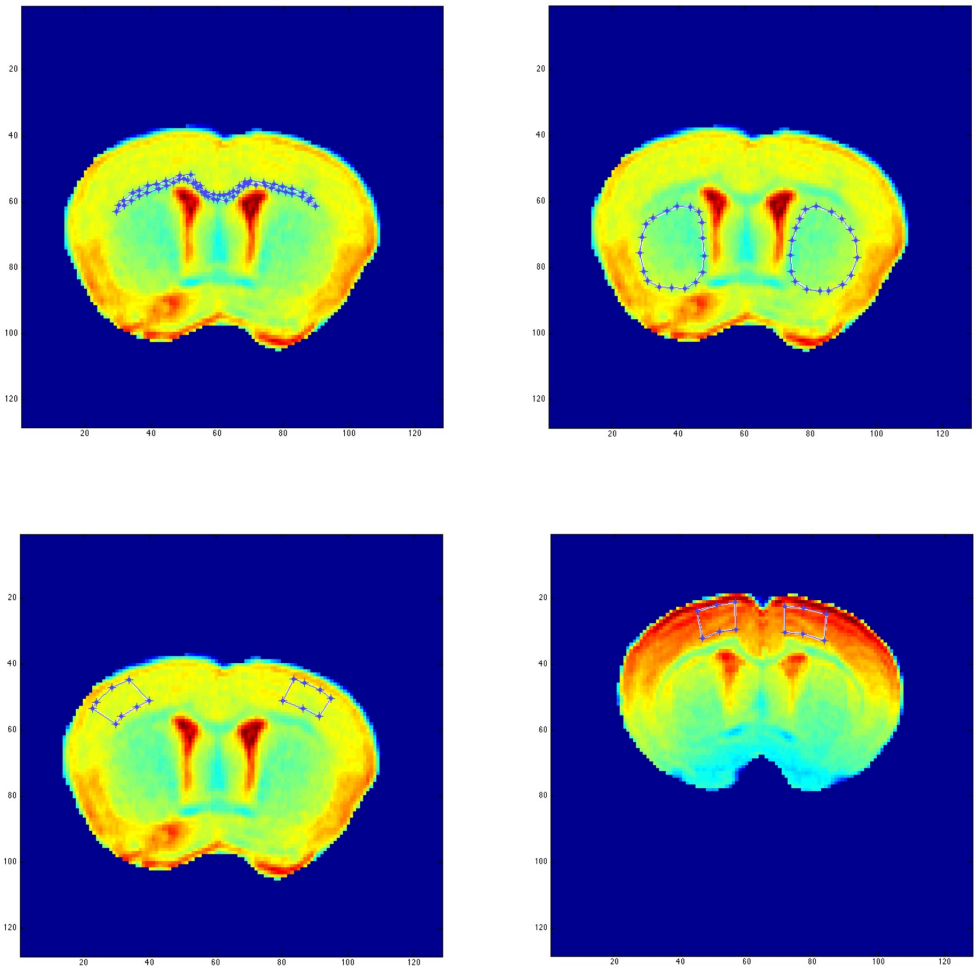

Figure 2.7: Placement of ROIs
Shown on mouse brain A5: Top left: corpus callosum, top right: deep gray matter, bottom left: cortex in mouse. Shown on rat brain 45: bottom right: cortex in rat

2.6 Statistical analysis

A two-sided Wilcoxon rank sum test was applied to the mean neurite densities and ADC in each mouse brain ROI. The mean values from each brain were used to determine if the changes between groups were significant. The test was performed using the ranksum matlab function, and all groups were compared with the others. Differences were considered significant at a level of $p \leq 0.05$.

The analysis was not repeated for the longitudinal and extracellular diffusion coefficients, as these parameters are not completely unrelated to the neurite density, and thus to avoid bias due to multiple comparisons. Instead, correlation coefficients between the three model parameters and ADC were computed. As well as correlations towards histology. When expanding the analysis to also include MTR contrast and individual histology, a full scale ANOVA model is suggested for the statistical analysis.

Chapter 3

Results

3.1 Mouse brains

3.1.1 Image quality

All images had a FWHM measured in the shimming protocol that was between 8.8 and 13.7 Hz after shimming, low enough to proceed with diffusion imaging. The average value was 10.9 Hz before shimming with second order shims, and 9.8 Hz after.

The SNR was found to be significantly worse when some brains were rescanned after two months of storage. This was due to the RF coil performing below its specifications, and possibly also the relatively long storage time of the brains. Data from the first scanning of brain A4 was corrupted, and due to the low SNR in the rescanning, the brain was discarded from analysis. In all the images from the initial scanning of the brains, the SNR was determined to be good enough to use the data in analysis. The noise level was not found to change with b-value.

In diffusion weighted imaging, the signal intensity, and thus the SNR, decreases exponentially with increasing b-values, as seen in figure 3.1. This can also be seen from the diffusion weighted images at various b-values, as illustrated in figure 3.2.

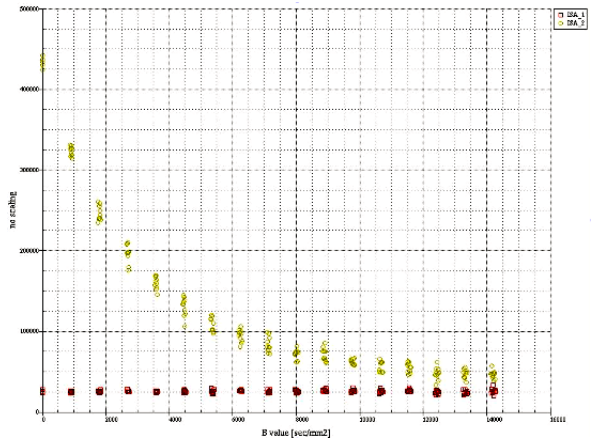

Figure 3.1: The signal intensity as a function of b-value
Plot of the signal intensity in a deep gray matter ROI in brain D2. The noise level is also shown. The image was generated in ParaVision.

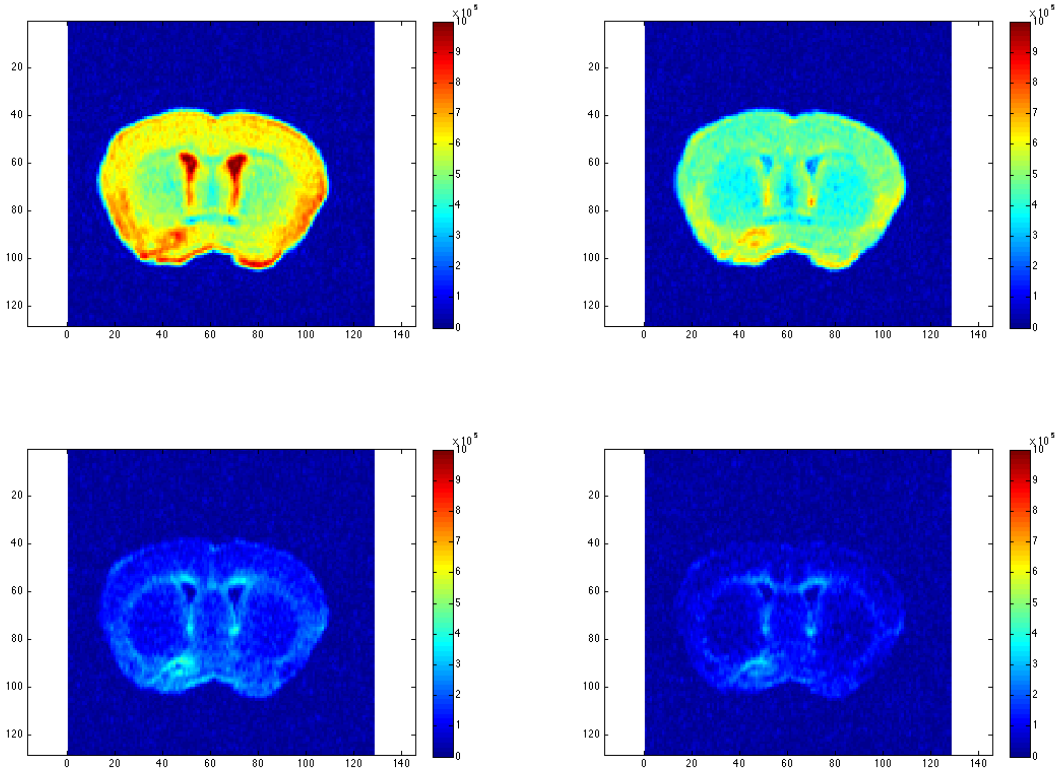

Figure 3.2: Attenuation of signal intensity with increasing b-value
Here shown in brain A5. From top left to bottom right: b=0, 880, 6160 and 14080 s/mm^2. The signal intensity is shown on a scale from 0 to 10^6 in all images.

Some degree of motion artefact was present in the readout direction in most of the diffusion weighted images. The degree varied between brains, and also between slices in each brain. In most images it had little effect on the regions of interest, but brains E2, C4 and C5 were excluded from the analysis due to this artefact. Motion artefact in two brains is shown in figure 3.3. Gibbs ringing was also present in some diffusion images, affecting the part of the cortex in the upper part of the brain, as seen in figure 3.4. Cortex ROIs were placed to avoid artefacts as far as possible.

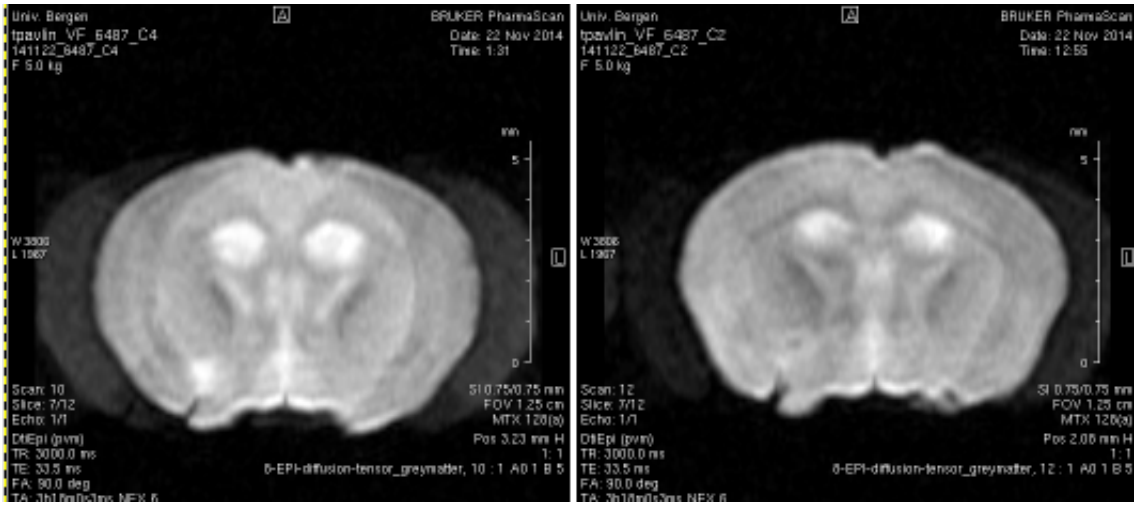

Figure 3.3: Varying degrees of motion artefact.
On the left: Brain C4 where the artefact is very bad, and is seen in and outside the brain. On the right: Brain C2 where the artefact is present but to a much lesser extent.

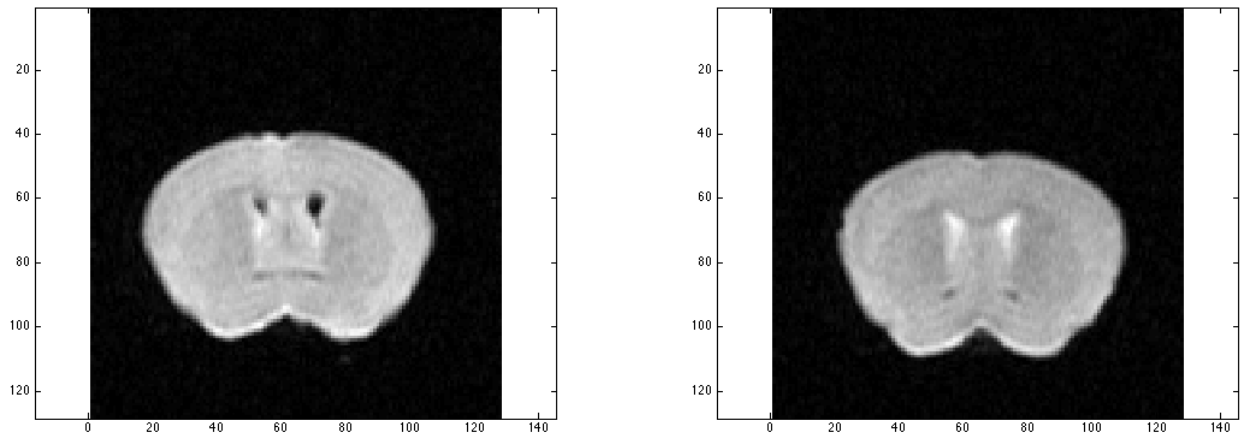

Figure 3.4: Gibbs ringing seen the A-P direction in mouse brains D3 and D4

For each image slice that was fitted, a corresponding χ^2 map showing the quality of the fit was also generated. Representative maps are shown in figure 3.5. An ideal χ^2 has no visible structure (it is flat) in any parts of the bran. The scaling of the maps is affected by the noise level, and since it is in arbitrary units, the scaling will vary between the maps.

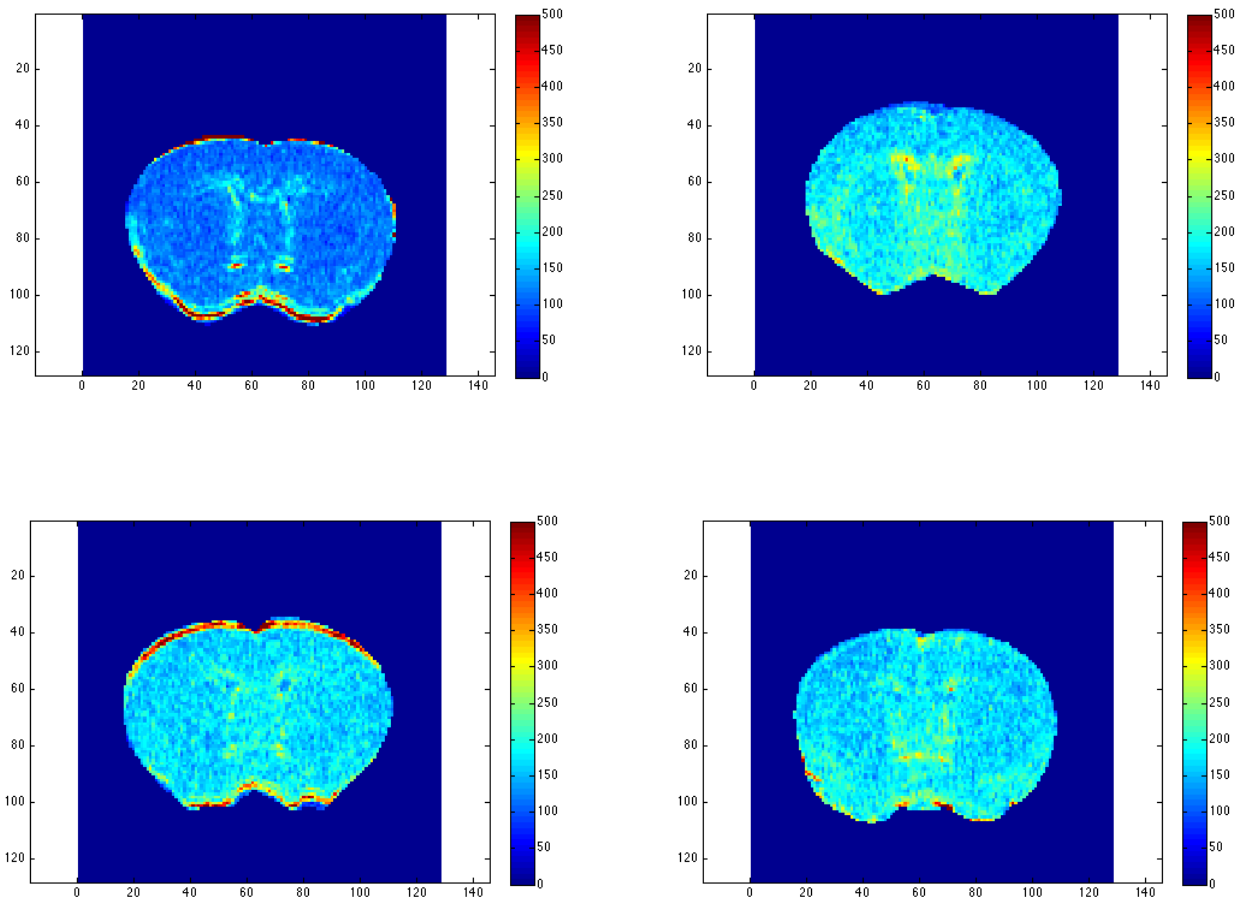

Figure 3.5: Examples of χ^2 maps
Top left: brain A2 (control), top right: brain D1 (3 weeks), bottom left: brain C3 (5 weeks), bottom right: brain E6 (remyelinated). Varying degrees of structure is seen in the ventricles and corpus callosum of each brain.

3.1.2 Neurite density and diffusion coefficients

In the analysis, only parameters from the cortex ROI in the right brain hemisphere are used, and these are also the values presented here. This will be further addressed in the discussion.

Neurite density

One representative neurite density map from each group is shown in figure 3.6. Plots of the mean neurite density values are shown in figures 3.7, 3.8, and 3.9. Cuprizone exposure leads to demyelination and neuronal loss, and so the neurite volume fraction is expected to decrease with exposure. In all three regions, the plots show a change in the neurite density with exposure time. As expected, the neurite density decreased with cuprizone exposure, due to demyelination. It then returned to values near the baseline level after the exposure was ended and the brains had remyelinated. The statistical analysis showed that the difference in neurite density between the controls and the 5-week group was significant in all ROIs, so was the difference between the 5-week and the remyelinated brains. In corpus callosum, the decrease in neurite density after 3 weeks of exposure was not significant compared to the control brains, but in both gray matter ROIs it was. All results of the statistical analysis can be seen in table 3.2.

In the CC and DGM ROIs, at least half of the neurite density values from the brains in the group were within one standard deviation of the group mean. All values in these ROIs were within the .95 confidence interval. Data from the cortex ROI placed in the right brain hemisphere is displayed,two values fall outside the .95 confidence interval of the mean cortex neurite densities.

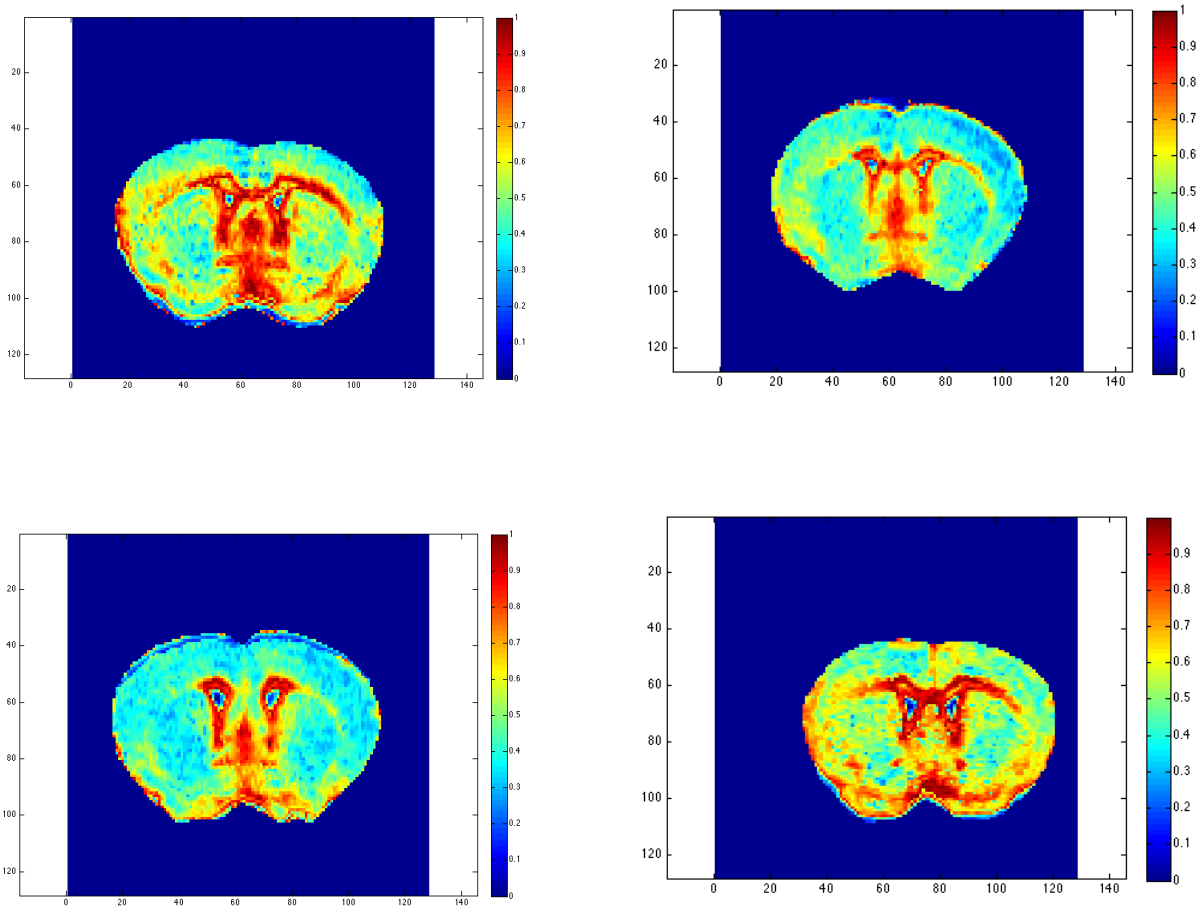

Figure 3.6: Neurite density maps
Top left: brain A2 (control), top right: brain D1 (3 weeks), bottom left: brain C3 (5 weeks), bottom right: brain D6 (remyelinated). The scale goes from 0 to 1.

Group	Corpus Callosum	Deep gray matter	Cortex
Controls	0.75 ± 0.07	0.50 ± 0.04	0.53 ± 0.03
3 week	0.70 ± 0.07	0.42 ± 0.03	0.45 ± 0.02
5 week	0.64 ± 0.08	0.42 ± 0.03	0.42 ± 0.02
Remyelinated	0.75 ± 0.08	0.48 ± 0.04	0.51 ± 0.03

Table 3.1: Mean neurite density values in each group
The group mean neurite density values in all regions of interest, with their respective standard deviations. Note that the plots show mean values with the .95 confidence intervals as error bars, not the standard deviations.

Groups	Corpus callosum	Deep gray matter	Cortex
H_0:(Controls=3w)	p=0.25	p=**0.01**	p=**0.01**
H_0:(Controls=5w)	**p=0.02**	p=**0.02**	p=**0.02**
H_0:(Controls=Remyelinated)	p=1	p=0.39	p=0.60
H_0:(3w=5w)	p=0.15	p=0.88	p=0.19
H_0:(3w=Remyelinated)	p=0.25	p=**0.02**	p=**0.02**
H_0:(5w=Remyelinated)	**p=0.02**	p=**0.04**	p=**0.05**

Table 3.2: p-values of the Wilcoxon rank sum test on mean neurite densities
Significant changes are marked in bold font.

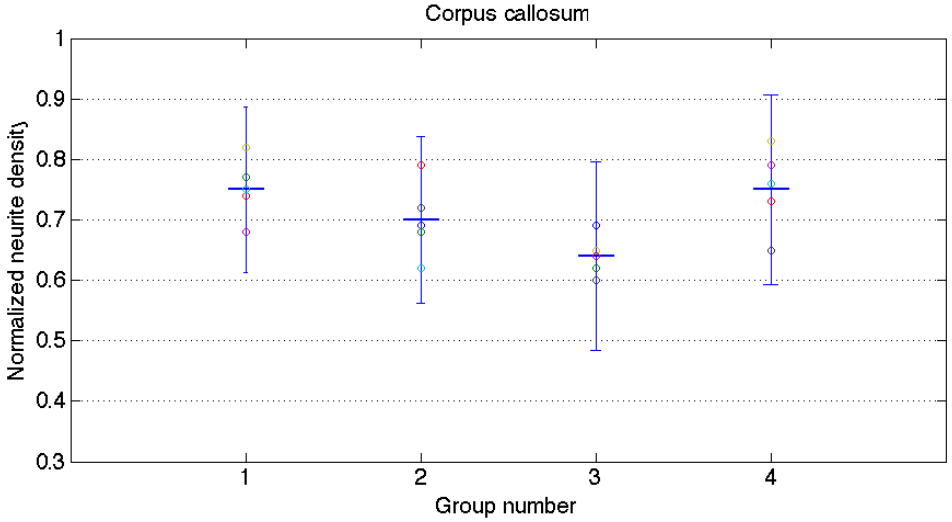

Figure 3.7: Plot of neurite density values of the corpus callosum in each group
The plot shows the group mean neurite densities as horizontal lines, the value from each individual brain in the groups as a circle, and the .95 confidence levels of the means as vertical error bars. The groups are numbered as follows: 1 - controls, 2 - 3 weeks, 3 - 5 weeks, 4 - remyelinated.

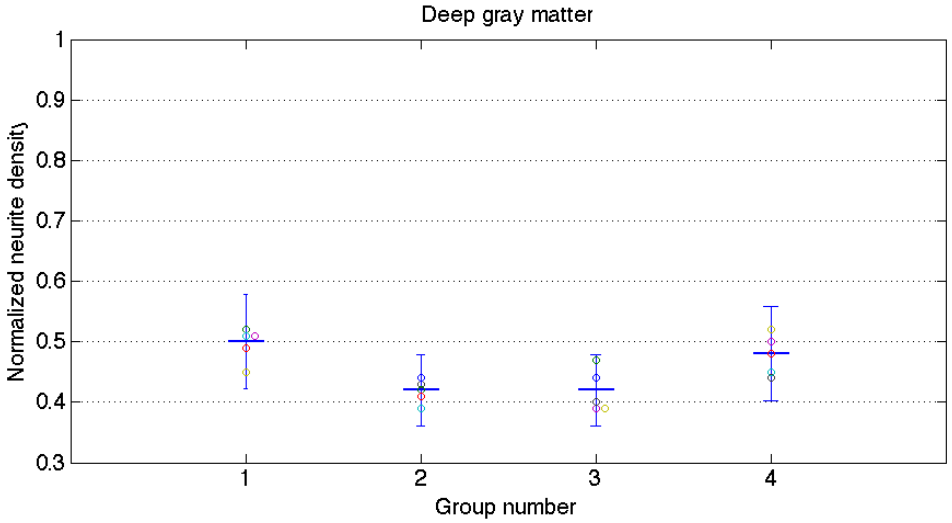

Figure 3.8: Plot of neurite density values of the deep gray matter in each group
The plot shows the group mean neurite densities as horizontal lines, the value from each individual brain in the groups as a circle, and the .95 confidence levels of the means as vertical error bars. The groups are numbered as follows: 1 - controls, 2 - 3 weeks, 3 - 5 weeks, 4 - remyelinated.

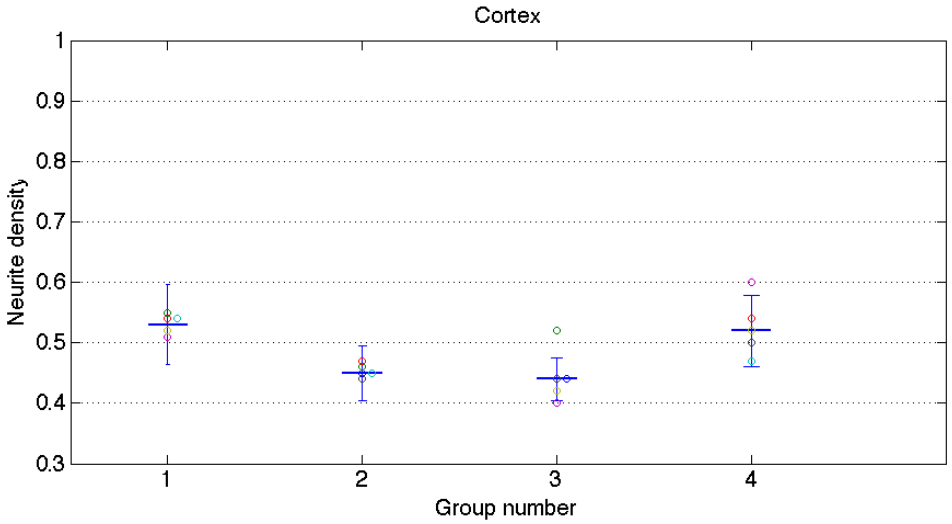

Figure 3.9: Plot of neurite density values of the cortex in each group
The plot shows the group mean neurite densities as horizontal lines, the value from each individual brain in the groups as a circle, and the .95 confidence levels of the means as vertical error bars. The groups are numbered as follows: 1 - controls, 2 - 3 weeks, 3 - 5 weeks, 4 - remyelinated.

Longitudinal diffusion coefficient

A representative map of the longitudinal diffusion coefficient in each group is shown in figure 3.10. The mean longitudinal diffusion coefficients are plotted in figures 3.11, 3.13, and 3.12. An increased D_L was seen in all ROIs in the exposed brains, ans a decrease after remyelination.

In the CC and DGM ROIs, with two exceptions, at least half of the longitudinal diffusion coefficients from the brains in the group were within one standard deviation of the group mean. With the exception of the DGM control group where 3 of 5 brains were in the .95 confidence interval, all groups had at least 4 of 5 brains within the interval and their outliers were very close to the interval limits.

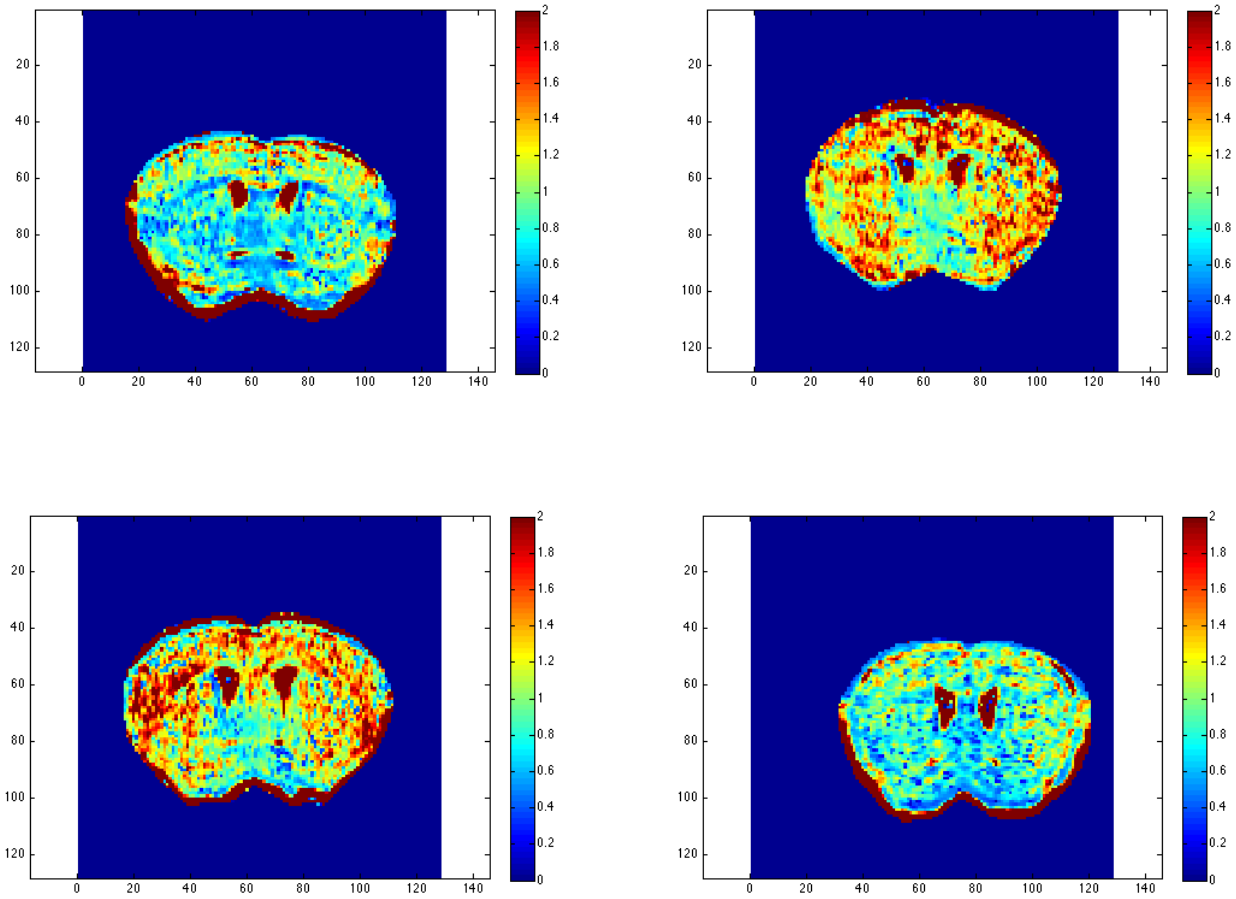

Figure 3.10: Longitudinal diffusion maps.
Top left: brain A2 (control), top right: brain D1 (3 weeks), bottom left: brain C3 (5 weeks), bottom right: brain D6 (remyelinated). Scale: 0.0-2.0 $\mu m^2/ms$

Group	Corpus callosum	Deep gray matter	Cortex
Controls	0.7 ± 0.2	0.9 ± 0.1	1.0 ± 0.2
3 week	0.8 ± 0.2	1.0 ± 0.1	1.1 ± 0.1
5 week	1.0 ± 0.1	1.0 ± 0.1	1.1 ± 0.1
Remyelinated	0.8 ± 0.1	0.9 ± 0.2	1.0 ± 0.1

Table 3.3: Mean longitudinal diffusion coefficients in each group.
The group mean longitudinal diffusion coefficients [μm^2/ms] in all regions of interest, with their respective standard deviations. Note that the plots show mean values with the .95 confidence intervals as error bars, not the standard deviations.

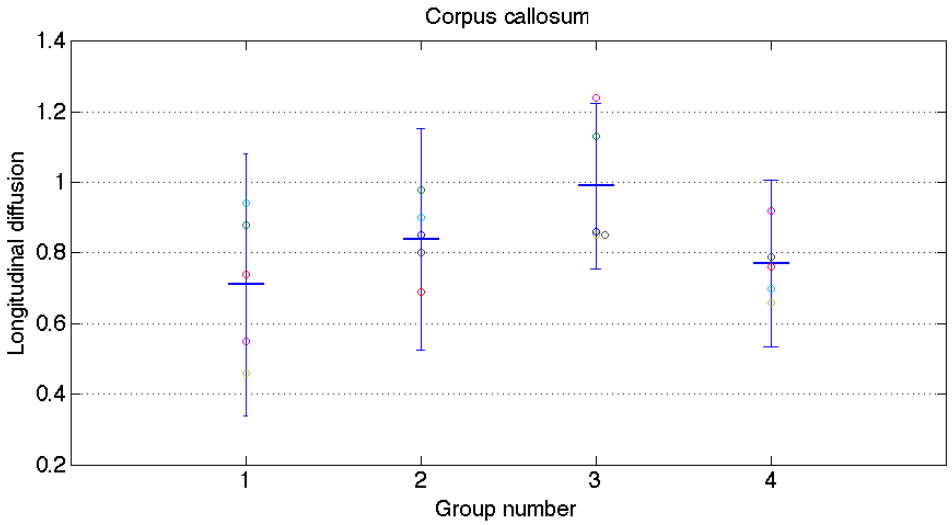

Figure 3.11: Plot of longitudinal DC in the corpus callosum of each group
The plot shows the group mean diffusion coefficients [μm^2/ms] as horizontal lines, the value from each individual brain in the groups as a circle, and the .95 confidence levels of the means as vertical error bars. The groups are numbered as follows: 1 - controls, 2 - 3 weeks, 3 - 5 weeks, 4 - remyelinated.

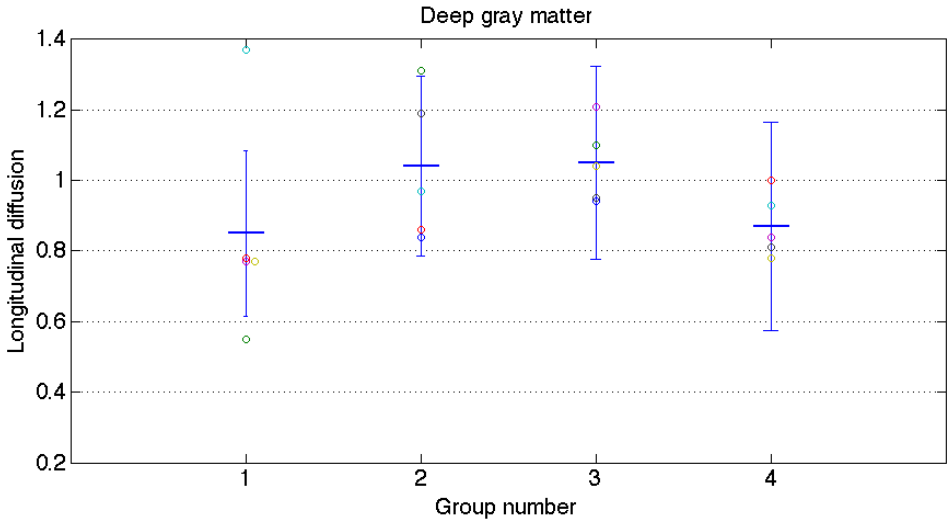

Figure 3.12: Plot of longitudinal DC in the deep gray matter of each group
The plot shows the group mean diffusion coefficients [$\mu m^2/ms$] as horizontal lines, the value from each individual brain in the groups as a circle, and the .95 confidence levels of the means as vertical error bars. The groups are numbered as follows: 1 - controls, 2 - 3 weeks, 3 - 5 weeks, 4 - remyelinated.

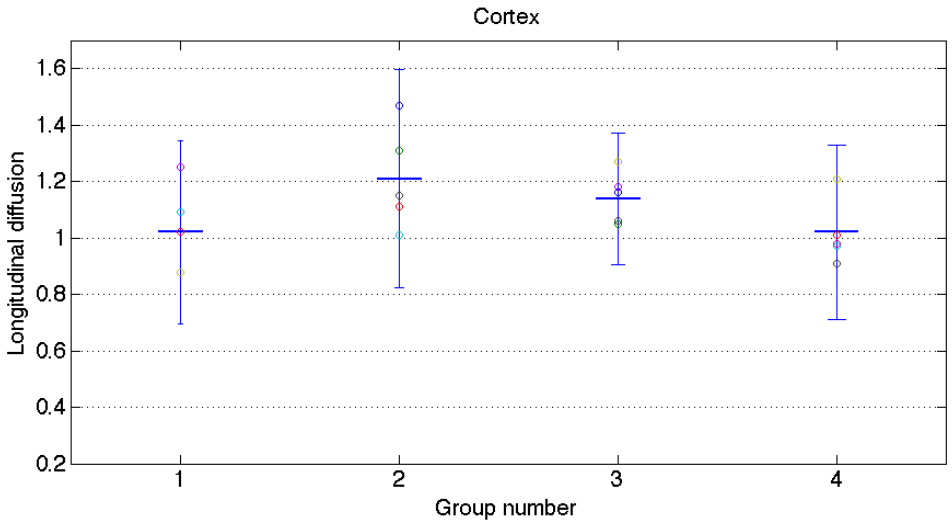

Figure 3.13: Plot of longitudinal DC in the cortex of each group
The plot shows the group mean diffusion coefficients [$\mu m^2/ms$] as horizontal lines, the value from each individual brain in the groups as a circle, and the .95 confidence levels of the means as vertical error bars. The groups are numbered as follows: 1 - controls, 2 - 3 weeks, 3 - 5 weeks, 4 - remyelinated.

Extracellular diffusion

Representative maps of the extracellular diffusion coefficient in each group are shown in figure 3.14. The mean extracellular diffusion coefficients are plotted in figures 3.15, 3.16, and 3.17. In the corpus callosum of unexposed and remyelinated brains there is little extracellular space, and an increased diffusion coefficient was seen in the CC of cuprizone exposed brains. In deep gray matter and cortex little change was seen in the extracellular diffusion from group to group.

In all the ROIs at least half of the extracellular diffusion coefficients from the brains in each group were within one standard deviation of the group mean. In the corpus callosum and the deep gray matter all coefficients were within the .95 confidence interval.

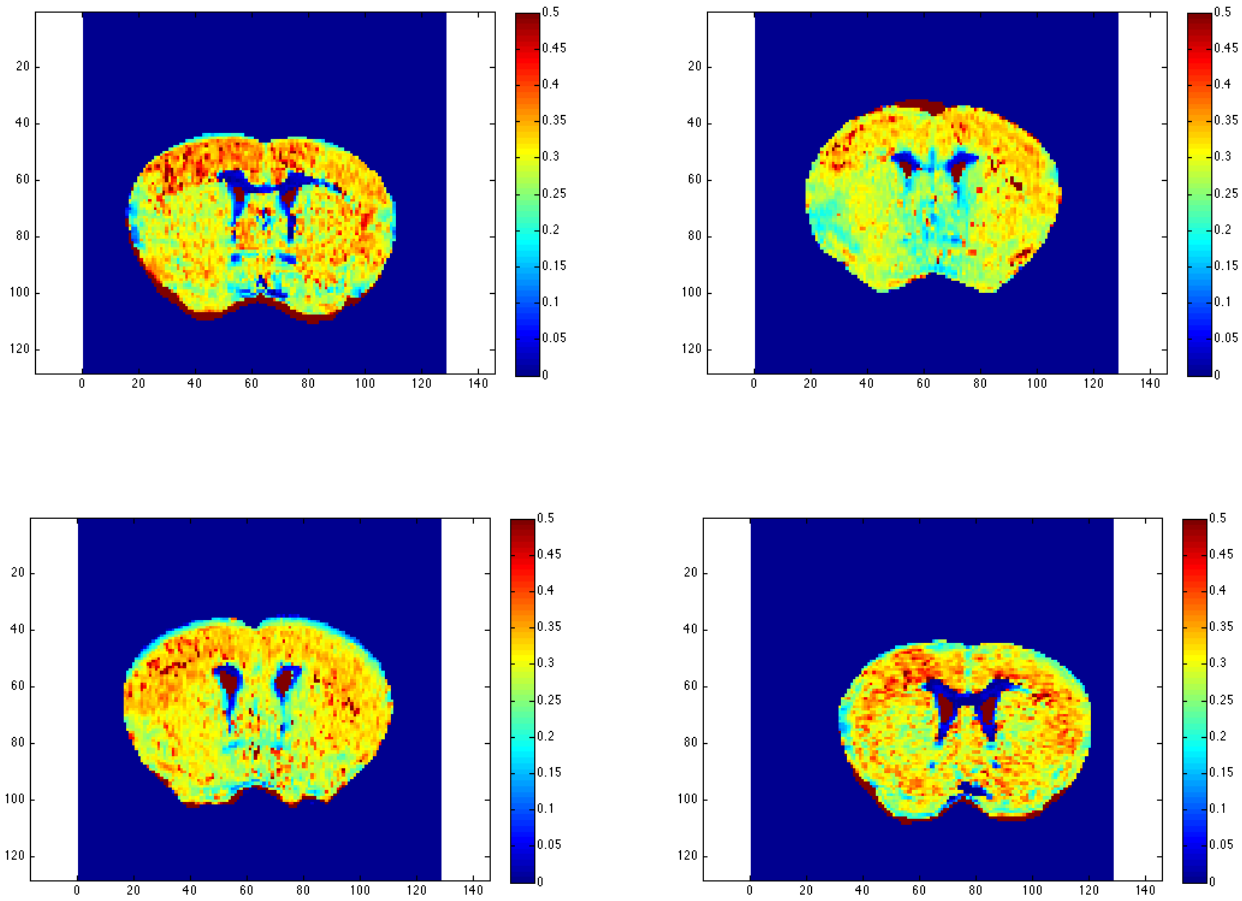

Figure 3.14: Extracellular diffusion maps.
Top left: brain A2 (control), top right: brain D1 (3 weeks), bottom left: brain C3 (5 weeks), bottom right: brain D6 (remyelinated). Scale: 0.0-0.5 $\mu m^2/ms$

Group	Corpus callosum	Deep gray matter	Cortex
Controls	0.15 ± 0.06	0.28 ± 0.02	0.33 ± 0.03
3 week	0.23 ± 0.06	0.30 ± 0.01	0.34 ± 0.02
5 week	0.31 ± 0.05	0.31 ± 0.02	0.35 ± 0.02
Remyelinated	0.20 ± 0.08	0.31 ± 0.02	0.37 ± 0.03

Table 3.4: Mean extracellular diffusion coefficients in each group.
The group mean extracellular diffusion coefficients [$\mu m^2/ms$] in all regions of interest, with their respective standard deviations. Note that the plots show mean values with the .95 confidence intervals as error bars, not the standard deviations.

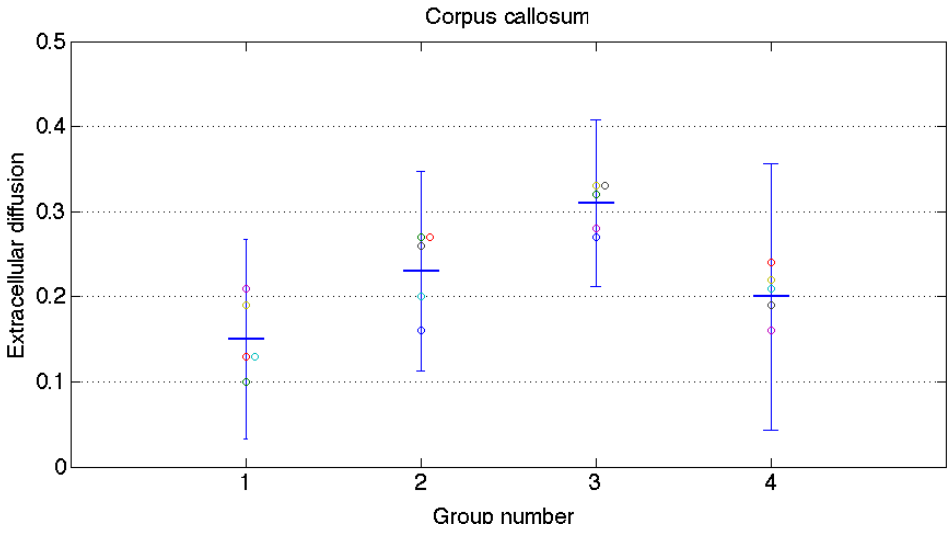

Figure 3.15: Plot of extracellular DC in the corpus callosum of each group
The plot shows the group mean diffusion coefficients [$\mu m^2/ms$] as horizontal lines, the value from each individual brain in the groups as a circle, and the .95 confidence levels of the means as vertical error bars. The groups are numbered as follows: 1 - controls, 2 - 3 weeks, 3 - 5 weeks, 4 - remyelinated.

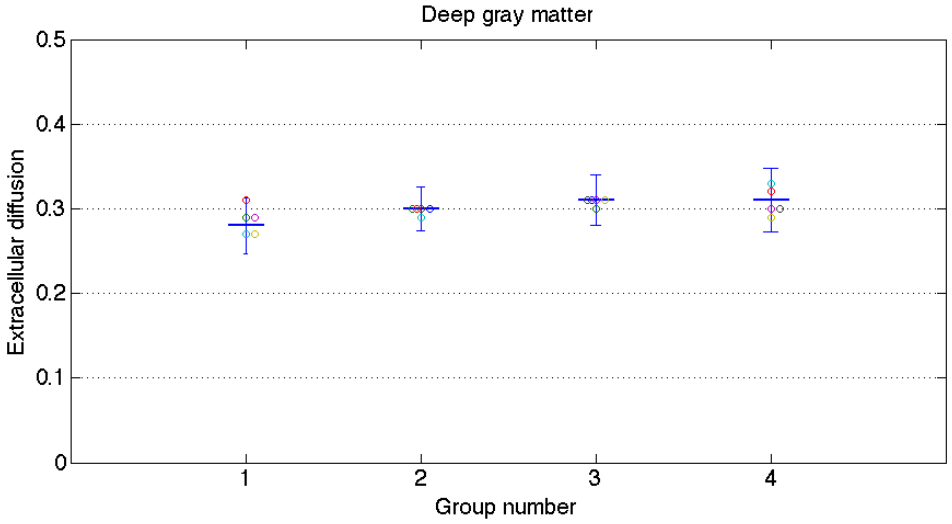

Figure 3.16: Plot of extracellular DC in the deep gray matter of each group
The plot shows the group mean diffusion coefficients [μm^2/ms] as horizontal lines, the value from each individual brain in the groups as a circle, and the .95 confidence levels of the means as vertical error bars. The groups are numbered as follows: 1 - controls, 2 - 3 weeks, 3 - 5 weeks, 4 - remyelinated.

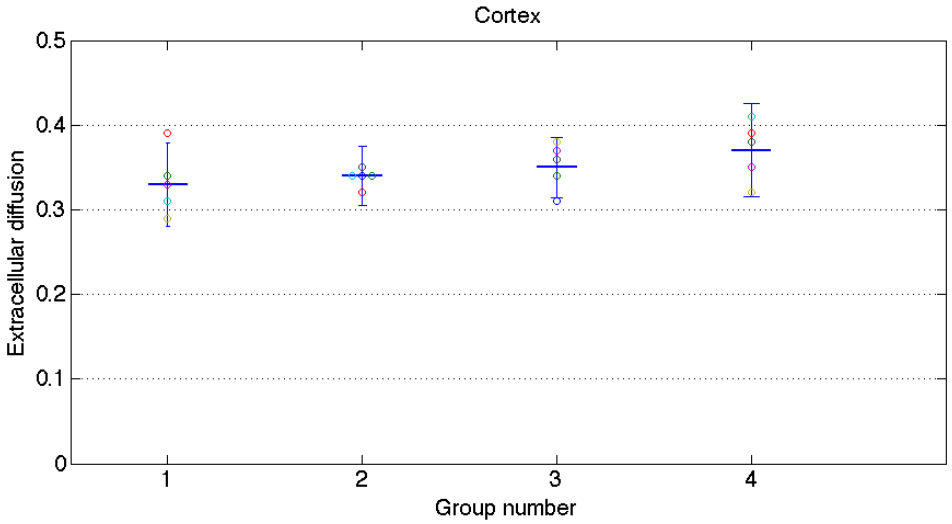

Figure 3.17: Plot of extracellular DC in the cortex of each group
The plot shows the group mean diffusion coefficients [μm^2/ms] as horizontal lines, the value from each individual brain in the groups as a circle, and the .95 confidence levels of the means as vertical error bars. The groups are numbered as follows: 1 - controls, 2 - 3 weeks, 3 - 5 weeks, 4 - remyelinated.

3.1.3 ADC values

The mean ADC value was estimated in the same ROIs as in the previous analysis, namely the corpus callosum, deep gray matter and cortex in all the brains. Representative ADC maps are shown in figure 3.18. Plots of the mean ADC values are shown in figures 3.19, 3.20, and 3.21. In the analysis only values from the cortex ROI in the right brain hemisphere were used, and these are also the values presented here. The group means and corresponding standard deviations were calculated, and the group means were plotted with the .95 confidence interval as the error bars, and the ADC value in each brain scatter plotted. All plots are on a scale from 0.1 to 0.4 $\mu m^2/ms$.

Group	Corpus callosum	Deep gray matter	Cortex
Controls	0.17 ± 0.02	0.26 ± 0.01	0.33 ± 0.01
3 week	0.23 ± 0.02	0.29 ± 0.01	0.34 ± 0.01
5 week	0.26 ± 0.02	0.30 ± 0.01	0.35 ± 0.01
Remyelinated	0.21 ± 0.02	0.27 ± 0.01	0.33 ± 0.01

Table 3.5: Mean ADC in all groups and ROIs
The mean apparent diffusion coefficient [$\mu m^2/ms$] with corresponding standard deviations

Groups	Corpus callosum	Deep gray matter	Cortex
H_0:(Controls=3w)	p=**0.02**	p=0.10	p=0.19
H_0:(Controls=5w)	p=**0.01**	p=0.07	p=0.27
H_0:(Controls=Remyelinated)	p=**0.05**	p=0.61	p=0.52
H_0:(3w=5w)	p=0.06	p=0.59	p=1
H_0:(3w=Remyelinated)	p=0.17	p=0.18	p=0.71
H_0:(5w=Remyelinated)	p=**0.02**	p=**0.03**	p=0.60

Table 3.6: Results of the Wilcoxon rank sum test on mean ADC
Significant changes are marked in bold font

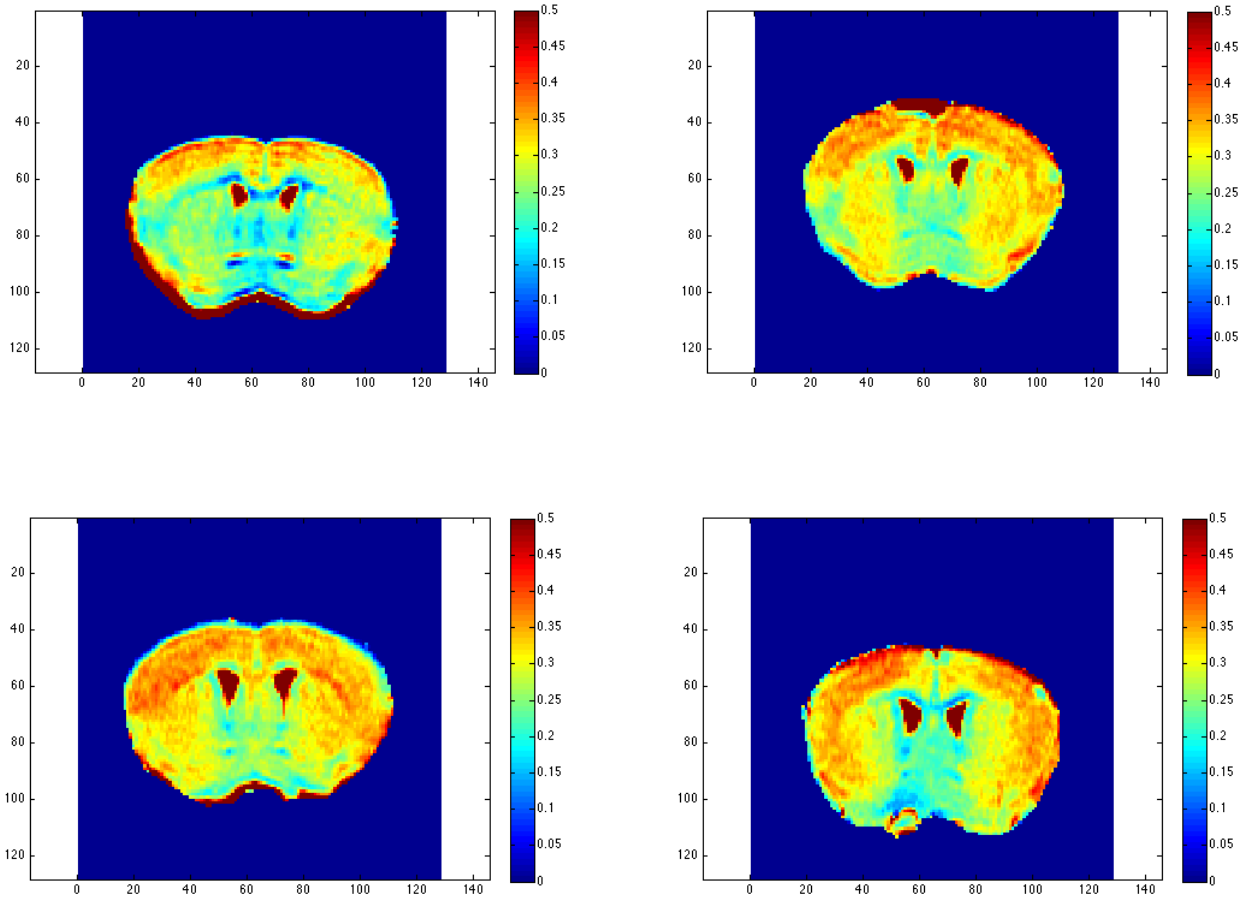

Figure 3.18: Representative ADC maps.
From the top left to the bottom right: Brain A2 (Control), D1 (3 weeks), C3 (5 weeks), and D5 (Remyelinated. All on a scale from 0.0 to 0.5 $\mu m^2/ms$

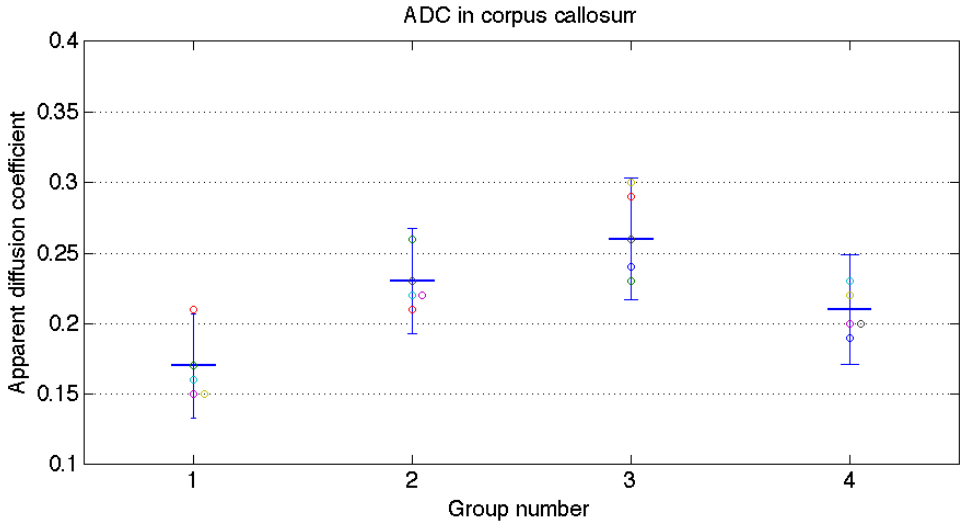

Figure 3.19: Plot of apparent diffusion coefficients in the corpus callosum of each group The plot shows the group mean ADC [μm^2/ms] as horizontal lines, the value from each individual brain in the groups as a circle, and the .95 confidence levels of the means as vertical error bars. The groups are numbered as follows: 1 - controls, 2 - 3 weeks, 3 - 5 weeks, 4 - remyelinated.

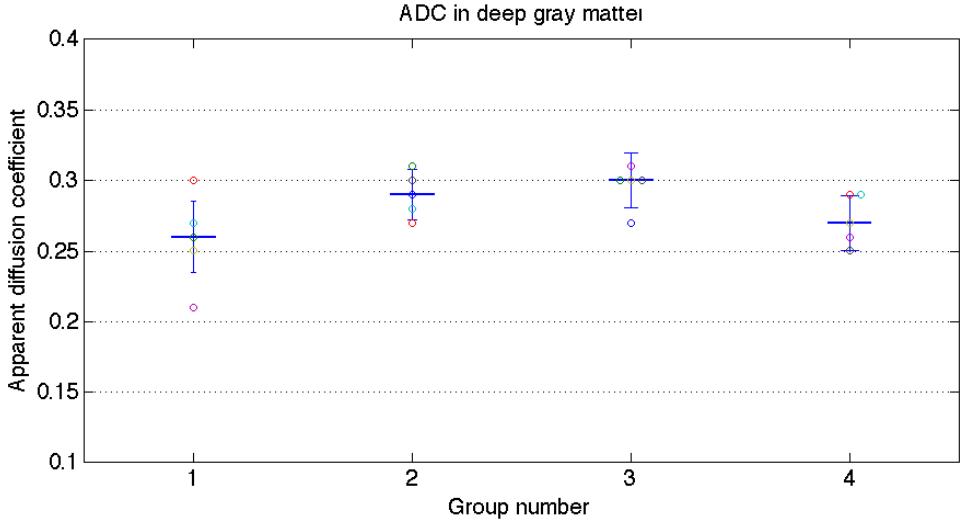

Figure 3.20: Plot of apparent diffusion coefficients in the deep gray matter of each group The plot shows the group mean ADC [μm^2/ms] as horizontal lines, the value from each individual brain in the groups as a circle, and the .95 confidence levels of the means as vertical error bars. The groups are numbered as follows: 1 - controls, 2 - 3 weeks, 3 - 5 weeks, 4 - remyelinated.

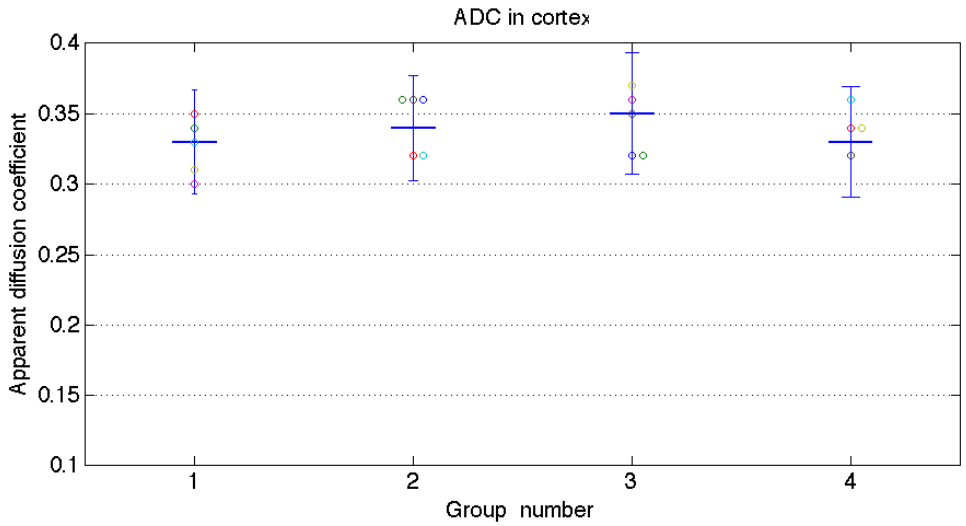

Figure 3.21: Plot of apparent diffusion coefficients in the cortex of each group
The plot shows the group mean ADC [μm^2/ms] as horizontal lines, the value from each individual brain in the groups as a circle, and the .95 confidence levels of the means as vertical error bars. The groups are numbered as follows: 1 - controls, 2 - 3 weeks, 3 - 5 weeks, 4 - remyelinated.

3.2 Rat brains

3.2.1 Image quality

In the rat brains the average FWHM before shimming with second order shims was 20.8 Hz, and after shimming it was 17.4 Hz, sufficient to proceed with the scanning in all cases. When using a surface coil, the signal intensity will decrease with distance from the coil. The highest SI was thus found in the cortex ROIs, and the lowest in deep gray matter. There were less problems with artefacts in the rat brain images, and no data was discarded from analysis.

3.2.2 Neurite density and diffusion coefficients

The parameters of the complex model are shown in tables 3.7, 3.8, and 3.9 for the three regions of interest. As is apparent from the mean values, no significant change was found in any of the parameters from the controls to the exposed brains (2 weeks).

Corpus callosum		Deep gray matter		Cortex	
Controls	CPZ exposed	Controls	CPZ exposed	Controls	CPZ exposed
0.8±0.2	0.8±0.1	0.49±0.08	0.49±0.08	0.52±0.06	0.52±0.07
0.8±0.1	0.7±0.2	0.5±0.1	0.47±0.09	0.53±0.06	0.53±0.06
0.8±0.2	0.8±0.1	0.5±0.1	0.50±0.09	0.48±0.05	0.49±0.07
0.80±0.09	**0.79±0.08**	**0.51±0.06**	**0.49±0.05**	**0.51±0.03**	**0.51±0.04**

Table 3.7: Neurite density in rat brains.
Mean values from the ROIs in each brain with standard deviations, and the group means (in bold) with their standard deviations

Corpus callosum		Deep gray matter		Cortex	
Controls	CPZ exposed	Controls	CPZ exposed	Controls	CPZ exposed
1.0±0.3	1.1±0.3	1.0±0.3	1.0±0.3	1.3±0.2	1.2±0.3
1.0±0.3	1.0±0.2	0.8±0.2	1.0±0.3	1.3±0.3	1.3±0.2
1.1±0.3	1.0±0.2	1.0±0.3	1.0±0.2	1.3±0.2	1.3±0.2
1.0±0.2	**1.0±0.2**	**1.0±0.2**	**1.0±0.2**	**1.3±0.1**	**1.2±0.1**

Table 3.8: Longitudinal diffusion coeffcients in rat brains.
Mean longitudinal diffusion coefficients [μm^2/ms] from the ROIs in each brain with standard deviations, and the group means (in bold) with their standard deviations

Corpus callosum		Deep gray matter		Cortex	
Controls	CPZ exposed	Controls	CPZ exposed	Controls	CPZ exposed
0.4±0.2	0.4±0.2	0.49±0.04	0.46±0.04	0.46±0.05	0.46±0.05
0.3±0.3	0.4±0.1	0.52±0.05	0.47±0.04	0.48±0.08	0.50±0.05
0.4±0.3	0.4±0.3	0.43±0.06	0.51±0.05	0.49±0.05	0.53±0.06
0.4±0.2	**0.4±0.1**	**0.48±0.03**	**0.48±0.03**	**0.47±0.04**	**0.50±0.03**

Table 3.9: Extracellular diffusion coefficients in rat brains.
Mean extracellular diffusion coefficients [μm^2/ms] from the ROIs in each brain with standard deviations, and the group means (in bold) with their standard deviations

Chapter 4

Discussion

4.1 Results in mice

4.1.1 Modelled neurite density and diffusion coefficients

Corpus callosum

The cuprizone model has been shown to cause extensive demyelination in the corpus callosum (CC) of mice, and these changes can be detected by DTI and other imaging methods [44] . Similar results in our fitted data indicate that the model is well suited for detecting demyelination from cuprizone exposure. Our findings were in line with the expected trend, the average neurite density in brains that were exposed to cuprizone for 5 weeks was 17.2 % lower than in the control brains. In addition, in the remyelinated brains, the neurite density was at the same level as in the control brains. This recovery indicates that there were enough oligodendrocytes remaining that near complete remyelination of the axons was possible, and that there was little to no axonal death. It is also worth noting that the average neurite density was 8.6 % lower after 5 weeks of exposure than after 3 weeks, which is line with the expectation that the demyelination in mice increases with the duration of cuprizone exposure.

The longitudinal and extracellular diffusion coefficients both showed the same pattern. In demyelinated brains the diffusion is less restricted. The model assumes that axons and dendrites are the primary source of water restriction. In the cuprizone exposed brains the neurite density was shown to be lower, and a correlating result was an increase in the diffusion coefficients. In the CC a 39.4 % increase in average D_L from the control group to the maximum in the 5 week group was seen. However, there were large variations within each group. The extracellular diffusion was also significantly higher in the cuprizone exposed brains. But, it is difficult to estimate by how much, due to the large standard error of the mean values in the control and remyelinated groups. In the

control and remyelinated brains, the extracellular diffusion was so restricted that the model did not fit well, and the resulting values were in the noise region and less precise. This was also seen in the presented maps of extracellular diffusivity, particularly in the areas above the ventricles. In the 5 week group the standard deviation of each coefficient was on average lower than in the other groups, and the mean value was well above the noise region. From this, it can be concluded that the diffusion was less restricted in the corpus callosum of cuprizone exposed brains.

All the parameters discussed had a significant variance, and the underlying values of the group means were spread. The error in the corpus callosum was larger than in the cortex and deep gray matter. Corpus callosum is a narrow structure, and particularly prone to partial volume effect. The slice thickness in the diffusion protocol was 0.75 mm, and the position of the CC in the image varied from one slice to the next. Therefore, the pixels where CC is displayed in the resulting 2D image will also contain information from areas outside corpus callosum. In addition it was harder to ensure that only the CC was included in the ROIs in the cuprizone exposed brains, due to the volume reduction caused by demyelination. Using smaller ROIs in the corpus callosum was attempted, but no significant difference was seen. In addition, some of the smaller ROIs included too few pixels to give representative information for the CC. As seen in the presented neurite density maps, the volume of the CC was strongly reduced in the cuprizone exposed brains.

Deep gray matter

In deep gray matter (DGM) myelin occupies a lower fraction of the total volume than in corpus callosum, therefore the changes due to demyelination are smaller and harder to detect. Visually, this can be seen in the presented neurite density maps. The changes in CC is clearly seen across the images, while in the DGM the changes are less noticeable. The cuprizone exposed brains, both 3 and 5 weeks, had a significantly lower neurite density than the control group. There was also a significant remyelination after ended exposure, as compared to both the 3 week and 5 week groups. Unlike in the CC, there was no significant difference between the 3 week and 5 week groups. A probable reason why the neurite density of the two groups was at the same level is that there was near complete demyelination already after 3 weeks of exposure, or a balance between re- and demyelination. The significant remyelination indicates that a balance between re- and demyelination is probable, and that the recruitment and differentiation of oligodendrocyte precursor cells was sufficiently fast to remyelinate axons.

The longitudinal diffusion coefficients support the findings from the neurite density maps. Even though there was a lot of variation and large error bars, the trend was that the diffusion is less restricted in the demyelinated brains, and there was little difference between the 3 week and 5 week groups. Since the myelin is a small part of the total gray matter volume, demyelination might be more visible when looking at the neurite associated diffusion, compared to the change neurite density (volume). Unlike the neurite density, the longitudinal DC did not show a complete recovery in the remyelinated brains. This could be due to incomplete remyelination, or a more extensive loss of structure in

the neurons. However, the standard error of each group mean was significant, and there was a large intergroup spread of coefficient values. It is clear that cuprizone exposure leads to demyelination and increased diffusion in the neurites of DGM. Upon comparison of D_L in CC and DGM it was seen that the values in the 5 week group in CC are on the same level as the 3 and 5 week brains in DGM. This indicates that the axons in CC and the neurites in DGM have the same low level of myelin at these stages of cuprizone exposure.

The extracellular DC did not change much with cuprizone exposure. The assumption that diffusion can be modelled as isotropic in extracellular space has been found to be accurate in gray matter. The model fits well, and we do not expect to see significant changes in this parameter. It is worth noting that the spread of values within each group was small, and so was the standard error. This is in sharp contrast to the CC where the model did not fit as well and the errors were large.

Cortex

There was a systematic left-right asymmetry in the axial plane of the images, this mainly affected the cortex ROIs and will be discussed further in section 4.1.4. In the one cortex ROI presented in the results, a significant reduction of neurite density was seen in both the 3 and 5 week groups, as compared to the control brains. Compared to these groups, there was a significant increase in neurite density in the remyelinated brains. There was no significant difference in neurite density between the control group and the remyelinated group. This is in line with what was seen in deep gray matter.

The longitudinal diffusion coefficient plot showed many of the same tendencies as the neurite density plot, but with a larger spread in values. The highest values of D_L were found in the 3 and 5 week brains, which indicates a demyelination of the cortex. However, the spread of values was so large, and the standard errors so significant, that it becomes difficult to conclude on the extent of the demyelination from these parameters. The large spread within each group could be due to the structure of the cortex, where there are layers with decreasing neuron density towards the surface. With an ROI that includes all layers it is natural to have a spread in values across the ROI volume.

Like in the deep gray matter no large change in the extracellular diffusion is expected, and none was seen from the plots. The extracellular diffusion did not vary much within the groups or between them, which is line with the expectation.

χ^2 and quality of fit

The model was developed for investigating the gray matter, and so it is expected that it will not fit as well in white matter. The model data is fitted using a least squares curve fit, and χ^2 is the sum of the residuals squared. The residual is given by the function fun(x,xdata)-ydata, where fun is the fitting function, xdata is the input matrix of gradient values, x are the chosen parameters of the fit, and ydata are the signal intensities normalized by Sigma, the standard deviation of the noise. Sigma only affects the scaling of χ^2, and in the fitting it was set to a constant value based on values read

from the MR images. Since the signal intensity is in arbitrary units the intensity will vary between the maps. Ideally the χ^2 map is completely structureless and flat. The more structure is visible, the worse the fit in that region. No brains were discarded on account of a bad fit. However, some structure was seen in a large number of the brains: mostly in the ventricles which are not part of any ROI, but also in the corpus callosum. Little to no structure was seen in the cortex and deep gray matter, as can be expected in a gray matter model.

4.1.2 Histological correlation to diffusion weighted MRI data

Myelin content and axons were estimated by staining for PLP and and NFL immunopositivity, respectively. This was done by Dr. Stig Wergeland. PLP is myelin proteolipid protein, a major constituent of compact myelin. NFL is neurofilament light chain, the major structural axonal protein involved in axonal transport. The mean values were found in ROIs in the cortex, deep gray matter and corpus callosum, as shown in figure 4.1. A oneway ANOVA test applied to the mean values of the ROIs was used for the statistical analysis, differences were considered significant at a level of $p<0.05$.

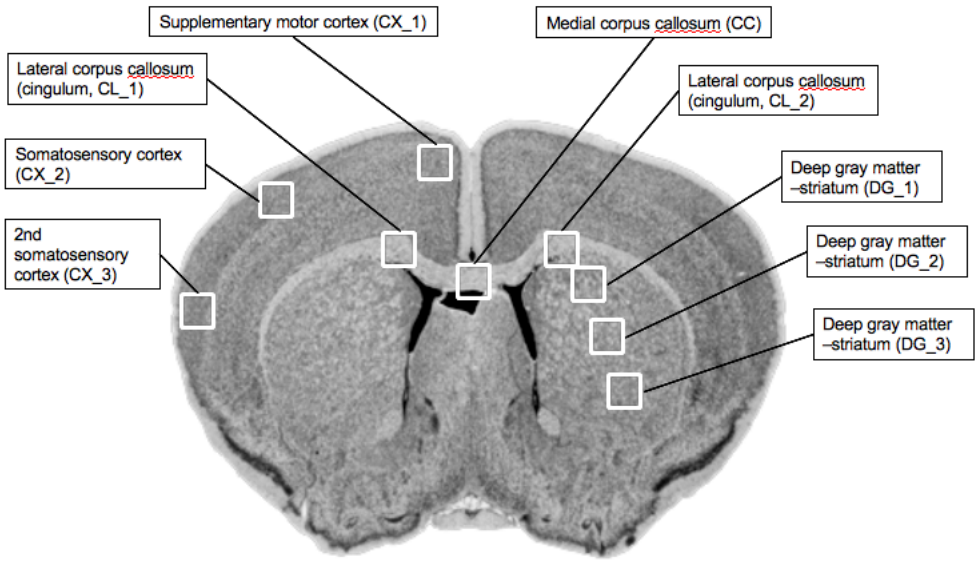

Figure 4.1: Regions of interest in histology

In the corpus callosum (CC and CL) a significant decrease in myelin content was seen after 5 weeks of cuprizone exposure, as compared to the control group. A decrease was also seen after 3 weeks, but not at a significant level. In the remyelinated brains there was a significant increase in myelin content, compared to the 5 week group. In both the medial and lateral corpus callosum a significant decrease in NFL immunopositivity was

seen in the 5 week group, compared to the control brains. The remyelinated group did not show a signifcant increase compared to the 5 week group.

The results in the cortex and the deep gray matter showed a similar trend. There was a significant reduction of the myelin level after both 3 and 5 weeks of exposure, compared to the control group. An increase in myelin was seen in the remyelinated brains, however, it was not significant compared to the cuprizone exposed groups. In addition, the PLP values in remyelinated deep gray matter were significantly different from the control group, which indicates a low level of remyelination. While there wwere changes in NFL immunopositivity from group to group, they were not significant. All mean values with standard deviations are shown in the table in figure 4.2, significant changes from the control group are marked in bold font.

	Weeks CPZ exposure							
	Controls		3		5		4 weeks RM	
	M	SD	M	SD	M	SD	M	SD
Myelin								
PLP_CC	89.5	(5.8)	72.1	(11.1)	**29.8**	**(26.4)**	77.0	(10.8)
PLP_CL	93.9	(1.2)	87.9	(4.8)	**55.3**	**(22.7)**	87.2	(4.6)
PLP_CX	11.3	(4.6)	**5.8**	**(5.0)**	**2.5**	**(2.1)**	6.6	(4.5)
PLP_DG	27.6	(8.4)	**14.8**	**(2.6)**	**12.8**	**(5.2)**	**18.8**	**(6.7)**
Axons								
NFL_CC	93.4	(2.6)	88.5	(4.4)	**77.8**	**(14.6)**	85.4	(8.0)
NFL_CL	83.5	(4.9)	77.9	(3.7)	**63.5**	**(14.0)**	78.8	(7.3)
NFL_CX	25.5	(10.4)	15.9	(7.7)	18.4	(5.1)	17.2	(7.0)
NFL_DG	32.5	(15.0)	25.2	(6.5)	24.0	(7.2)	23.0	(7.2)

Figure 4.2: Table of mean values from histopathology
Significant changes are marked in bold font, in this table changes are significant if the group is significantly different from the healthy controls.

While the neurite density is not the same as the myelin content or axons, a comparison of the values will give a good indication of how well the model represents the changes that occur with cuprizone exposure. The correlation coefficient, as calculated using the matlab corrcoef function, between PLP and neurite density was measured to be 0.90 or higher in all regions of interest, on a scale where 1 is complete correlation. The correlation with NFL values was as high in the lateral corpus callosum, but not in the other regions. All calculated correlation coefficients can are found in table 4.1.

	Corpus callosum			
Parameter	PLP CC	PLP CL	NFL CC	NFL CL
Neurite density	0.95	0.91	0.80	0.94
Longitudinal DC	-0.99	-0.98	-0.98	-0.99
Extracellular DC	-0.97	-0.93	-0.93	-0.97

	Deep gray matter		Cortex	
Parameter	PLP DG	NFL DG	PLP CX	NFL CX
Neurite density	0.92	0.59	0.90	0.61
Longitudinal DC	-0.83	-0.42	-0.76	-0.56
Extracellular DC	-0.85	-0.98	-0.47	-0.60

Table 4.1: The correlation coefficients between histological parameters and the parameters of the complex model

The scale is from 1 to -1, where 1 is complete correlation, -1 is complete negative correlation, and 0 is no correlation.

Corpus callosum

The corpus callosum ROI used in analysis of the diffusion weighted images included the same areas as those used in histology. In the diffusion weighted images partial volume effect is present to a larger extent than in histology, and the neurite density values are therefore likely underestimated. While there are differences between the two histology ROIs, the development of myelin content and axons follows the same trend. In both the histology parameters and the neurite density, a non-significant decrease was seen in the 3 week group, and a significant decrease in the 5 week group, as compared with the healthy controls. In histology a significant increase in PLP immunopositivity was seen from the 5 week group to the remyelinated, this was also seen in neurite density. A full comparison of values is seen in table 4.2.

Parameter	Controls	3 week	5 week	Remyelinated
PLP (myelin) CC	89.5±5.8	72.1±11.1	**29.8±26.4**	**77.0±10.8**
PLP CL	93.9±1.2	87.9±4.8	**55.3±22.7**	**87.2±4.6**
NFL (axons) CC	93.4±2.6	88.5±4.4	**77.8±14.6**	85.4±8.0
NFL CL	83.5±4.9	77.9±3.7	**63.5±14.0**	78.8±7.3
Neurite density	0.75±0.07	0.70±0.07	**0.64±0.08**	**0.75 ± 0.08**

Table 4.2: Parameter comparison in corpus callosum

Significant changes are marked in bold font, the statistical analysis compares the cuprizone exposed (3w and 5w) brains to the control group, and the remyelinated to the 5 week group. CC is the medial corpus callosum, CL is the lateral.

Gray matter - Deep gray matter and cortex

In both the myelin content and the neurite density of deep gray matter a significant decrease was seen after both 3 and 5 weeks of cuprizone exposure, compared to the healthy controls. None of the parameters changed significantly between the 3 week and the 5 week groups. The mean neurite density level decreased by 16 % after cuprizone exposure, while the largest decrease in PLP and NFL immunopositivity was 54 and 26 %, respectively. However, the decrease in NFL immunopositivity was not judged to be significant, this may be an issue of statistical power. It also indicates that the neuronal loss not related to myelin is smaller. In the remyelinated brains there was a non-signifcant increase of PLP immunopositivity, and little change in the axon level. There was also a significant difference between the control group and the remyelinated group. Meanwhile, the diffusion model showed a significant increase of neurite density from the 5 week group to the remyelinated. All values can be seen in table 4.3.

Parameter	Controls	3 week	5 week	Remyelinated
PLP	27.6±0.4	**14.8±2.6**	**12.8±5.2**	18.8±6.7
NFL	32.5±15.0	25.2±6.5	24.0±7.2	23.0±7.2
Neurite density	0.50±0.04	**0.42±0.03**	**0.42±0.03**	**0.48±0.04**

Table 4.3: Parameter comparison in deep gray matter
Significant changes are marked in bold font, the statistical analysis compares the cuprizone exposed (3w and 5w) brains to the control group, and the remyelinated to the 5 week group.

The neurite density values presented in table 4.4 are from the cortex ROI placed in the right hemisphere of the brain. The values from histology are averaged from three ROIs placed in the same hemisphere. The histology ROIs are also placed in the part of the cortex closest to the surface, as seen in figure 4.1. The neuron density in the cortex decreases with distance from the corpus callosum, so it is expected that the histology will show lower values than if all layers of the cortex were included. However, cuprizone exposure affects all layers of the cortex and is detected in all ROIs. After 3 and 5 weeks of cuprizone exposure a significant decrease in PLP immunopositivity and neurite density was seen. Like in DGM, the histology showed a non-significant increase in PLP and NFL immunopositivty in the remyelinated brains, while the model showed a significant increase of neurite density, as compared to the 5 week group.

Parameter	Controls	3 week	5 week	Remyelinated
PLP	11.3±4.6	**5.8±5.0**	**2.5±2.1**	6.6±4.5
NFL	25.5±10.4	15.9±7.7	18.4±5.1	17.2±7.0
Neurite density	0.53±0.03	**0.45±0.02**	**0.42±0.02**	**0.51±0.03**

Table 4.4: Parameter comparison in cortex
Neurite density values from the right brain hemisphere is used, while the histological parameters are averaged from both hemispheres. Significant changes are marked in bold font, the statistical analysis compares the cuprizone exposed (3w and 5w) brains to the control group, and the remyelinated to the 5 week group.

In both gray matter regions (DGM and the cortex) the remyelinated brains had a significantly increased neurite density compared to the 3 and 5 week groups, with values close to the baseline level. This was not the case with the histology parameters, where no significant increase was seen, and the values were further from the baseline values. In DGM, the myelin content was found to have significantly decreased from the control group to the remyelinated brains. Neither of the gray matter neurite density values correlate well with NFL immunopositivity, the correlation coefficients are 0.59 in DGM and 0.61 in the cortex. Combined with the high correlation coefficients between neurite density and PLP immunopositivity, this can be an indication that the diffusion model is less successful at detecting neuronal loss exceeding demyelination. If this is the case, the neurite density values of the remyelinated group are probably over-estimated, and there may not be a significant increase. This would also be in line with the estimated myelin content in DGM, which was significantly lower in the remyelinated brains than in healthy controls. However, it is important to note that histology does not present the correct answer, it is a technique that also has disadvantages and flaws.

4.1.3 Comparison to conventional model results

Correlation to neurite density and diffusion coefficients

The matlab function corrcoef was used to find the correlation coefficient between the group means of ADC and neurite density, the longitudinal DC, and the extracellular DC. This was done for all three regions of interest. The correlation coefficient is given on a scale from -1 to 1, where 1 is total correlation, -1 is total negative correlation, and 0 is no correlation. The results of the application of this test are presented in table 4.5. Interestingly, the extracellular DC correlates most with the ADC in corpus callosum, and by far the least in gray matter. This shows how the extracellular DC is a fair indicator of change in white matter. While, as discussed previously, in gray matter the extracellular space is not as affected by the demyelination.

Parameters	Corpus callosum	Deep gray matter	Cortex
ADC and neurite density	-0.90	**-0.97**	**-0.97**
ADC and longitudinal DC	0.93	0.95	0.91
ADC and extracellular DC	**0.98**	0.65	-0.05

Table 4.5: Correlation coefficients between ADC and the other parameters. The largest correlation coefficient in each ROI is marked in bold font.

Corpus callosum

In the corpus callosum, all parameters of the complex model correlate well with the apparent diffusion coefficient. The models do not contradict each other, and the parameters follow the same trend across the stages of cuprizone exposure. As seen in table 3.1, a significant decrease in neurite density was seen from the control group to the 5 week group, and a significant increase was seen from the 5 week group to the remyelinated group. The significant changes in the cuprizone exposed brains, as compared to the baseline level, was also seen in the ADC in CC. Here, a significant increase in diffusivity was seen after both 3 and 5 weeks. Both parameters also showed a significant change from the 5 week to the remyelinated group. However, ADC also changed significantly between the control brains and the remyelinated brains, while in the neurite density there was little difference between the two values. Both the longitudinal and extracellular diffusion coefficients were increased in the remyelinated group, as compared to the control group. This is in line with the partial remyelination detected in the ADC. However, these coefficients had a large spread in values and large standard deviations. The values of the histology parameters were also lower in the remyelinated group than in the control group, but not significantly. This could indicate that the conventional model is better suited for imaging white matter, the complex model is of the gray matter, and has its limitations in white matter applications.

Deep gray matter

In deep gray matter, the ADC was found decrease significantly from the 5 week group to the remyelinated group. This was the only significant change detected by the conventional model in this region. There was also an increase in ADC in the cuprizone exposed (3w and 5w) brains, compared to the controls, but not on a significant level. In the neurite density a significant decrease was seen in both the 3 week and 5 week group, compared to the control group. As well as a significant increase from the demyelinated groups to the remyelinated group. The longitudinal diffusion coefficient and the ADC follow the same trend, and the results from the two models do not contradict each other. The histology results support the neurite density changes from the controls to the 3 and 5 week brains. This shows the strength of the complex model when it is applied to gray matter: both the neurite density and the longitudinal DC are dependent on the neurons. Changes that are small on a total volume scale, like the neurite density decrease from 50

to 42 % of the total volume, impact the parameters in the complex model on a significant level.

Cortex

In the cortex none of the detected changes in ADC were significant. Meanwhile, the neurite density found from the complex model showed a significant decrease after both 3 and 5 weeks of cuprizone exposure, compared to the baseline level. There was also a significant increase in neurite density in the remyelinated brains, compared to both the 3 week and the 5 week group. As in the deep gray matter, histology also showed a significant decrease after 3 and 5 weeks. The similarity of the results in DGM and the cortex signify that in gray matter imaging the complex model is advantageous to conventional modelling. It is both more specific and able to detect significant changes at a microstructural level.

4.2 Results in rats

Rats do not respond to cuprizone exposure in the same way as mice. Demyelination is expected to occur primarily in the cortex, and later in deep gray matter and corpus callosum. The seen effect is also expected to be smaller, as rats are more resistant to cuprizone than mice.

4.2.1 Corpus callosum and deep gray matter

In the corpus callosum no significant change was seen in neurite denisty, the longitudinal diffusion coefficient or the extracellular diffusion coefficient between the control group and the cuprizone exposed group. The spread of values within each group, and the variance of the group means were all larger than the small difference between the respective group means. The calculated standard errors of the group means were slightly larger in rat brains than in the mouse brains, because each rat group only contains three brains. In histological examinations no significant changes were seen in the corpus callosum with cuprizone exposure.

In the deep gray matter the same observations are made as in the CC. No significant change was seen in any of the parameters between the two groups in deep gray matter. There was also no significant change detected in the histology parameters.

4.2.2 Cortex

The neurite density in the cortex did not change significantly with cuprizone exposure, neither did the diffusion coefficients. However, a significant change between the groups was found in both histology and gene expression analysis. A clear demyelination and reduction of myelin-related proteins was seen in the cortex of the cuprizone exposed brains. These changes were seen in the upper layers of the cortex. Some measurements of the DWI model parameters were made with a smaller ROI, placed in the upper layers

of the cortex, but still no significant changes were seen. Smaller changes are expected in rats than in mice, and the results show that the DWI model is not sensitive enough to detect them. It may be that partial volume effects within the cortex even out the small changes. In this application of the model, it would be very useful to have an in-vivo model where the development in one animal was investigated. As there are some variations within both groups, it could be that the small changes can be detected if the same animal is followed. The exposure period could also have been extended to a point where significant changes were detected using MRI.

4.3 Practical difficulties and possible improvements

Practical difficulties are a part of any experiment, and the experiences can be used to improve the protocol for future projects. Here the difficulties in the scanning of the brains, and disadvantages of the DWI model are discussed.

4.3.1 Positioning of the brains

When imaging brains removed from the sculls, there was a need to make a holder to hold each brain in place for the duration of the scan. The positioning of the brain had to be reproducible, and it was also necessary to fully immerse the brains in Fomblin, without any air bubbles forming near the brain surface. This problem was solved by molding acrylic holders in 15 ml (for mice) and 50 ml (for rats) tubes. A precise drill was used to form a space for the brain. The holder and brain could then be inserted into a half-full tube of Fomblin, and all the air bubbles were pressed out. Three such holders in different sizes were made for the mouse brains. However, the brains vary in both length and width. The animals were sacrificed at different ages, and there were also some biological differences between the animals. It is impossible to make three perfect holders for 24 different brains. The focus was on avoiding compression of the brains, and so, some brains were placed in holders where they had some room to move. In addition, the brains were floating in the oil, instead of lying flat on the bottom of the holder compartment. These two factors complicated the angling and positioning of the slices. Additionally, the angle of the tube in the scanner had to be adjusted manually to get symmetrical axial slices. This led to some asymmetry in the axial images.

If brains were not removed from the scull before imaging, the positioning of the brain in the scanner could be easier. The largest problem with the positioning was the floating of the brains, which complicated the slice selection significantly. There was little problem with compression of the brains or air bubbles. However, in several brains there was some leftover PBS around the brain surface, which produces background signal in MRI. This problem was reduced somewhat, but not completely by rinsing the tubes with Fomblin between each scan, as well as rinsing each brain in Fomblin before it was placed in the holder.

4.3.2 Image quality

A large difficulty in this project was the reduction of the image quality when brains were rescanned. If the brains could have been rescanned with the same protocol and SNR levels, there would not have been a need to exclude data from the analysis. The coil used for scanning the mouse brains was found to have deteriorated to below the expected performance level. The reason for this is unknown. The worsened SNR could also be due to the storage of the brains. The brains had been stored in formalin for approximately 2 months at the time of rescanning. However, histology was performed after 5 months of storage, and the brains were not found to be damaged in any way.

Artefacts were present in several of the images. Gibbs artefact in the A-P direction that only affected the placement of the cortex ROIs, and motion artefact in the L-R direction that lead to discarding of data from three brains from the data analysis. The degree of artefacts did not show any pattern, nor was it significantly larger in any of the groups. It is also not clear what the source of the motion artefact was.

During the data analysis it became clear that there was a systematic left-right asymmetry in the diffusion weighted images. This was seen in most parameter maps, including the ADC maps. The asymmetry mainly affected the cortex which has ROIs placed far from the center of the brain, where asymmetry in the slice becomes an important factor. The asymmetry was also seen in corpus callosum, but only one ROI was defined in corpus callosum, and so the data all went into the same mean value. The difference in values seen between the two cortex ROIs is here exemplified by the neurite densities shown in table 4.6, and it can also be seen in maps of the diffusion parameters. The data from the two ROIs showed the same overall trend, and the asymmetry problem was sidestepped to some degree by including data from only on ROI in the analysis.

Group	Cortex Left	Cortex Right
Controls	0.48±0.04	0.53±0.03
3 week	0.40±0.03	0.45±0.02
5 week	0.35±0.02	0.44±0.02
Remyelinated	0.43±0.03	0.52±0.03

Table 4.6: The group mean neurite density in the two cortex ROIs

The symmetry of an image is determined by the angling of the slices. However, no corresponding asymmetry was seen in the T2-weighted images. The T2-weighted images could be less sensitive to the asymmetry, or the asymmetry in the parameter maps could be due to other factors. Other possible reasons for the asymmetry include non-uniformity of the applied diffusion gradients, and biological differences.

4.3.3 Disadvantages of the model

In the complex model, one diffusion coefficient describes the neurite associated diffusion. It is calculated as the longitudinal diffusion coefficient D_L minus the transversal diffu-

sion coefficient D_T, and D_T is assumed to be negligible on the timescale of the diffusion experiment. In doing so one assumes that the neurites are impermeable to water on our diffusion timescale. With demyelination the permeability of neurites is expected to increase, and the assumption may be less accurate. It could be that a significant part of the detected increase in D_L was due to increased transversal diffusivity. A low permeability is a necessary assumption to be able to calculate the signal intensity as a sum of the contribution from inside and outside the neurites. However, it would be interesting and possible to adapt the full model script to generate maps of both the longitudinal and transversal diffusion coefficients. Jespersen et al. have done this while developing the model, and estimated the transversal diffusion coefficient to be approximately 0.06 in the white matter, and 0.1 in the gray matter cortex of a healthy baboon [37]. They also found a significant correlation between D_T and the ADC in the same project. The inclusion of D_T as a separate parameter would strengthen the data analysis, and possibly give further insights to how neurites are affected by cuprizone exposure. However, in very narrow structures, such as dendrites, the transversal diffusivity becomes inseparable from zero because one reaches a resolution limit, dependent on the gradient strength [45]. In our experiment this limit was found to be approximately 1.3 μm, while dendrites have diameters of 0.1-0.2 μm. D_T is thus likely to only be significant in axons.

The assumption that all extracellular diffusion is isotropic is a rough approximation that works better for gray matter than white matter. This is likely the main reason the model is not as accurate for white matter. This problem has also been addressed by Jespersen et al. in a later publication [46]. However it is not a significant problem in the modelling of gray matter, which is the main focus of the thesis.

4.4 Adapting the model for in-vivo imaging

Ex-vivo imaging has both advantages and disadvantages. The main advantages are that histology is available for each brain, and thus at all stages of cuprizone exposure, and that the scan protocol is not very limited by scan times. There is also far less motion related difficulties in ex-vivo scanning. The main disadvantage is that we do not follow the development in the same animal over time. With in-vivo imaging each animal can be scanned several times, at different stages of cuprizone exposure. When following the development in one animal, there is no need to make assumptions on the parameters at different stages of exposure in comparisons. In-vivo experiments also limits the number of mice needed. In addition, an in-vivo scanning protocol could be adapted for clinical use.

The main challenges in adapting the protocol for in-vivo animal imaging are the scan times and the artefacts. The scan time can be greatly reduced by using a better performing coil in the image acquisition, the same SNR could then be achieved with fewer averages. The diffusion sequence used in the protocol is very sensitive to motion. Even if the small vibrations that led to artefact in this project were eliminated, there will always be motion in in-vivo imaging. However, despite the artefacts present in this project, we were able to estimate properties of the tissue mirostructure in a fairly

accurate manner. Even with larger motion artefacts, similar results may be found in-vivo. Clinical scanners also generally have more advanced motion correction techniques than the scanner used in this project, which will reduce the motion related artefacts.

Chapter 5

Conclusion and Outlook

In this project, a complex biophysical diffusion weighted imaging based model of gray matter microstructure has been applied to a degenerative experimental model of multiple sclerosis. The aim was to use the model parameters to quantify the neuronal integrity of ex-vivo mouse brains. The resulting parameters of the model were also compared to parameters of conventional DWI modelling and histology. Finally, the gray matter model was applied to a group of rats.

In both the white and gray matter of mice, a significant decrease in the neurite density was detected after five weeks of cuprizone exposure, as compared to healthy controls. Four weeks after ended exposure, a significant increase in neurite density from the five week level was seen in all regions of interest. The same trend was seen in the longitudinal diffusion coefficient associated with diffusion in dendrites and axons. The diffusivity increased in the 3 week and 5 week groups, and decreased in the remyelinated brains in all regions of interest.

The estimated neurite density was found to correlate well with the estimated myelin level from histology in all regions of interest. The measurements of myelin level followed the same trend as the development of the neurite density, but did not show a significant remyelination in any region. In gray matter there was little correlation between the axon development estimated from histology and the estimated neurite density and diffusion coefficients.

When compared to conventional DWI modelling, both the neurite density and the longitudinal diffusion coefficient correlated well with the ADC in both white and gray matter, and the models showed the same general trend. In white matter, the complex model was not found to be advantageous to the conventional model, as can be expected from a gray matter model applied to white matter. In the gray matter, the results from the complex model were found to be closer to histology results. In the cortex, the conventional model detected no significant changes in ADC with exposure, and in DGM

the only significant difference was from the five week group to the remyelinated. On the other hand, the complex model provided both added specificity and sensitivity to microstructural changes in gray matter.

In the rat brains no significant changes between the controls and the cuprizone exposed group were detected in any regions. Histology showed a significant demyelination and reduction of myelin-related proteins in the outer layers of the cortex. The model is not as sensitive as histology, and was not able to detect the small changes.

In future work, the results of this thesis will be compared to MTR measurements in the same brains. The MTR has previously been shown to correlate well with histological findings in the cuprizone mouse model. By providing an extra parameter, the general trend can be estimated with increased certainty, and the performance of the model further evaluated. It would also be of great interest to compare the DWI model parameters, histology parameters and MTR values in each brain. Further, an in-vivo application of the gray matter model can provide valuable insight to MS gray matter disease progression in one animal. It would also be an important step on the way to clinical application of the model.

Bibliography

[1] Jan Jansen and Joel Glover. Gliaceller. Store Medisinske Leksikon, `https://sml.snl.no/gliaceller`, 2009-02-13. (Accessed: 2014-11-25).

[2] Sigbjørn Fossum. Celleskjelett. Store Medisinske Leksikon, `https://sml.snl.no/celleskjelett`, 2009-02-13. (Accessed: 2014-11-25).

[3] Markus Nilsson, Danielle van Westen, Freddy Ståhlberg, Pia C. Sundgren, and Jimmy Lätt. The role of tissue microstructure and water exchange in biophysical modelling of diffusion in white matter. *Magn Reson Mater Phy.*, 26:345–370, 2013.

[4] Per Brodal. *Sentralnervesystemet*. Universitetsforlaget, Norway, fifth edition, 2013.

[5] Valentino Braitenberg and Almut Schüz. Cortex statistics and geometry of neuronal connectivity. *Springer*, 8:249–, 1998.

[6] AG Williams and T Capra. Neurogenetics at UT Health Science Center,1999 RW Williams, `http://www.mbl.org/atlas170/atlas170_frame.html`. (Accessed: 2015-05-13).

[7] Kjell-Morten Myhr, Unn Ljøstad, and Åse Mygland. Ms - multippel sklerose. Nevrologiske sykdommer - legehåndboka, `http://nevro.legehandboka.no/demyeliniserende-sykdommer/ms-multippel-sklerose-31960.html`, 2015.

[8] Aliza Ben-Zacharia. Medscape: Diagnosis, Treatments, and Prognosis in MS: A Nursing Perspective, `http://www.medscape.org/viewarticle/739432`. (Accessed: 2015-01-19).

[9] I.V. Allen, S. Mcquaid, G. Nevin, and M. Mirakhur. Pathological abnormalities in the normal-appearing white matter in multiple sclerosis. *J. Neurol. Sci.*, 22:141–144, 2001.

[10] Jonathan D. Thiessen, Yanbo Zhang, Handi Zhang, Lingyan Wang, Richard Buist, Marc R. Del Bigio, Jiming Kong, Xin-MIn Li, and Melanie Martin. Quantitative mri and ultrastructural examination of the cuprizone mouse model of demyelination. *NMR Biomed.*, 26:1562–1581, 2013.

[11] Massimo Filippi and Marco Rovaris. Magnetisation transfer imaging in multiple sclerosis. *Journal of NeuroVirology*, 6:115–120, 2000.

[12] Stig Wergeland. *Vitamin D and ω-3 polyunsaturated fatty acids as disease modifying factors in multiple sclerosis.* PhD thesis, University of Bergen, 2013.

[13] N. Manrique-Hoyos, T. Jurgens, and M. Gronborg et al. Late motor decline after accomplished remyelination: impact for progressive multiple sclerosis. *Ann. Neurol.*, 71(2):227–244, 2012.

[14] Lucas Silvestroff, Sandra Bartucci, Juana Pasquini, and Paula Franco. Cuprizone-induced demyelination in the rat cerebral cortex and thyroid hormone effects on cortical remyelination. *Experimanetal Neurology*, 235:357–367, 2012.

[15] Ernest M. Henley and Alejandro Garcia. *Subatomic physics.* World Scientific Publishing, 5 Toh Tuck Link, Singapore 596224, third edition, 2007.

[16] Atle Bjørnerud. The physics of magnetic resonance imaging. Univeristy of Oslo, Department of Physics, `http://www.uio.no/studier/emner/matnat/fys/FYS-KJM4740/v14/kompendium/compendium-mri-feb-2009.pdf`, 2008.

[17] Egil Lillestøl, Ola Hunderi, and Jan R. lien. *Generell fysikk for universiteter og høyskoler - Bind 2 Varmelære og elektromagnetisme.* Universitetsforlaget, Oslo, Norway, first edition, 2006.

[18] GyroMagician. Wikimedia, `http://en.wikipedia.org/wiki/Free_induction_decay`. (Accessed: 2015-05-13).

[19] Tina Pavlin. Phys212 lecture notes. Personal communication, 2014.

[20] Eli Renate Grüner. Compendium phys212, medical physics and technology. Personal communication, `https://miside.uib.no/dotlrn/classes/det-matematisk-naturvitenskapelige-fakultet/phys212/phys212-2013v/file-storage/download/105084175/20130122_PHYS212_Compendium_MRI.pdf`, 2012.

[21] Dr Jeremy Jones and Dr Usman Bashir. Gradient echo sequences. Radiopaedia, `http://radiopaedia.org/articles/gradient-echo-sequences-1`. (Accessed: 2015-01-19).

[22] Paul Tofts. *Quantitative MRI of the Brain: Measuring changes caused by disease.* Wiley, West Sussex, England, first edition, 2004.

[23] James H. McCellan, Ronald W. Schafer, and Mark A. Yoder. *Signal Processing First*. Pearson Education International, NJ, USA, first edition, 2003.

[24] Lothar R. Schad. Problems in texture analysis with magnetic resonance imaging. *Dialogues in Clinical Neuroscience*, 6:235–242, 2004.

[25] Scientific Volume Imaging. Aliasing. `http://www.svi.nl/AliasingArtifacts`. (Accessed: 2015-01-19).

[26] Eric W. Weisstein. Gibbs phenomenon. MathWorld - A Wolfram Web Resource, `http://mathworld.wolfram.com/GibbsPhenomenon.html`, 2015. (Accessed: 2015-02-23).

[27] Dr Ayush Goel and Dr Usman Bashir. Gibbs and truncation artifacts. Radiopaedia, `http://radiopaedia.org/articles/gibbs-and-truncation-artifacts`, 2015. (Accessed: 2015-02-23).

[28] C.D. Gregory. Univeristy of Illinois, 1998, `http://chickscope.beckman.uiuc.edu/roosts/carl/artifacts.html#ReferenceImage`. (Accessed: 2015-05-29).

[29] Washington State University. Shimming. Office of Research, Center for NMR Spectroscopy, `http://nmr.chem.wsu.edu/tutorials/basics/shimming/`, 2015. (Accessed: 2015-01-13).

[30] Tina Pavlin. Mri protocols. Internal use, Haukeland Univeristy Hospital, 2013-07-31.

[31] Michael Wendt. Second order shimming of high field magnets. MRI Hot Topics, Siemens medical, `http://www.healthcare.siemens.com/siemens_hwem-hwem_ssxa_websites-context-root/wcm/idc/siemens_hwem-hwem_ssxa_websites-context-root/wcm/idc/groups/public/@global/@imaging/@mri/documents/download/mdaw/mtqy/~edisp/second_hot_topic_brochure-00017029.pdf`. (Accessed: 2015-01-13).

[32] Biomedical Imaging Technology Center. Sequence diagrams. `http://bitc.bme.emory.edu/seq_dia.html`. (Accessed: 2015-01-19).

[33] Beth Israel Deaconess Medical Center. Magnetization transfer (mt) in cartilage. `http://www.bidmc.org/Research/Departments/Radiology/Laboratories/Cartilage/Research/CartilageCollagen/Magnetization.aspx`. (Accessed: 2015-05-30).

[34] Sveinung Fjær, Lars Bø, Arvid Lundervold, Kjell-Morten Myhr, Tina Pavlin, Øivind Torkildsen, and Stig Wergeland. Deep gray matter demyelination detected by magnetization transfer ratio in the cuprizone model. *PLOS ONE*, 8, 2013.

[35] Jeffrey J. Neil. Measurement of water motion (apparent diffusion) in biological systems. *Concepts in Magn. Reson.*, 9:385–401, 1997.

[36] Noam Shemesh, Evren Özarslan, Michal E. Komlosh, Peter J. Basser, and Yoram Cohen. From single-pulsed field gradient to double-pulsed field gradient mr: gleaning new microstructural information and developing new forms of contrast in mri. *NMR Biomed.*, 23:757–780, 2010.

[37] Sune N. Jespersen, Christopher D. Kroenke, Leif Østergaard, Josepg J.H. Ackerman, and Dmitriy A. Yablonskiy. Modeling dendrite density from magnetic resonance diffusion measurements. *NeuroImage*, 34:1473–1486, 2007.

[38] Eric W. Weisstein. Laplace series - from mathworld–a wolfram web resource. `http://mathworld.wolfram.com/LaplaceSeries.html`. (Accessed: 2015-01-08).

[39] Finn Levy. Formalin. Store Medisinske Leksikon, `https://sml.snl.no/formalin`, 2009-02-13. (Accessed: 2015-01-08).

[40] Robert J. Dawe, David A. Bennett, Julie A. Schneider, Sunil K. Vasireddi, and Konstantinos Arfanakis. Postmortem mri of human brain hemispheres: T2 relaxation times during formaldehyde fixation. *Magn. Reson. Med.*, 61(4):810–818, 2009.

[41] C.R. Zachariah, D. Pitt, P. Wassenar, B.D. Clymer, A. Abduljalil, M.V. Knopp, and P. Schmalbrock. Quantification of formalin-fixed ms brain tissue parameters t1, t2*, pd and phase at 7t and comparison with histopathology. *Magn. Reson. Med.*, 18:2073, 2010.

[42] Klaus Schmierer, Janet R. Thavarajah, Shu F. An, Sebastian Brandner, David H. Miller, and Daniel J. Tozer. Effects of formalin fixation on magnetic resonance indices in multiple sclerosis cortical gray matter. *Magn. Reson. Imaging.*, 32(5):1054–1060, 2010.

[43] Geoffrey Rolls. Fixation and fixatives - factors influencing chemical fixation, formaldehyde and glutaralhyde. Lecia Biosystems, Wetzlar, Germany, 2012-03-06. (Accessed: 2015-01-08).

[44] Emilia Sbardella, Francesca Tona, Nikolaos Petsas, and Patrizia Pantano. Dti measurements in multiple sclerosis: Evaluation of brain damage and clinical implications. *Multiple Sclerosis International*, Article ID 671730, 2013.

[45] Markus Nilsson. Imaging microstructure: Diffusion modelling. *Proc. Intl. Soc. Mag. Reson. Med*, 23, 2015.

[46] Sune N. Jespersen, Carsten R. Bjarkam, Jens R. Nyengaard, M. Mallar Chakravarty, Brian Hansen, Thomas Vosegaard, Leif Østergaard, Dmitriy Yablonskiy, Niels Chr. Nielsen, and Peter Vestergaard-Poulsen. Neurite density from magnetic resonance diffusion measurements at ultrahighfield: Comparison with light microscopy and electron microscopy. *NeuroImage*, 49:205–216, 2013.